A FINITE ELEMENT APPROACH TO THE 3D CSEM MODELING PROBLEM AND APPLICATIONS TO THE STUDY OF THE EFFECT OF TARGET INTERACTION AND TOPOGRAPHY

A Dissertation

by

JACK STALNAKER

Submitted to the Office of Graduate Studies of
Texas A&M University
in partial fulfillment of the requirements for the degree of

DOCTOR OF PHILOSOPHY

August 2004

Major Subject: Geophysics

A FINITE ELEMENT APPROACH TO THE 3D CSEM MODELING PROBLEM AND APPLICATIONS TO THE STUDY OF THE EFFECT OF TARGET INTERACTION AND TOPOGRAPHY

A Dissertation

by

JACK STALNAKER

Submitted to Texas A&M University
in partial fulfillment of the requirements
for the degree of

DOCTOR OF PHILOSOPHY

Approved as to style and content by:

Mark Everett (Chair of Committee)	Richard Gibson (Member)
David Sparks (Member)	Thomas Hilde (Member)
Krzystof Michalski (Member)	Richard Carlson (Head of Department)

August 2004

Major Subject: Geophysics

ABSTRACT

A Finite Element Approach to the 3D CSEM Modeling Problem
and Applications to the Study of the Effect of Target Interaction
and Topography. (August 2004)
Jack Stalnaker, B.S., College of Charleston
Chair of Advisory Committee: Dr. Mark Everett

The solution of the secondary coupled-vector potential formulation of Maxwell's equations governing the controlled-source electromagnetic (CSEM) response of an arbitrary, three-dimensional conductivity model must be calculated numerically. The finite element method is attractive, because it allows the model to be discretized into an unstructured mesh, permitting the specification of realistic irregular conductor geometries, and permitting the mesh to be refined locally, where finer resolution is needed. The calculated results for a series of simple test problems, ranging from one-dimensional scalar differential equations to three-dimensional coupled vector equations match the known analytic solutions well, with error values several orders of magnitude smaller than the calculated values. The electromagnetic fields of a fully three-dimensional CSEM model, recovered from the potentials using the moving least squares interpolation numerical differentiation algorithm, compares well with published numerical modeling results, particularly when local refinement is applied. Multiple buried conductors in a conductive host interact via mutual induction and current flow through the host due to the dissipation of charge accumulated on the conductor boundary. The effect of this interaction varies with host conductivity, transmitter frequency, and conductor geometry, orientation, and conductivity. For three test models containing two highly conductive plate-like targets, oriented in various geometries (parallel, perpendicular, and horizontal), mutual coupling ranges as high as twenty times the total magnetic field. The effect of varying host conductivity is significant, especially at high frequencies. Numerical modeling also shows that the vorticity of the currents density induced in a vertically oriented plate-like conductor rotates from vertical at high frequencies, to horizontal at low frequencies, a phenomenon confirmed by comparison with time domain field data collected in Brazos County, Texas. Furthermore, the effect of the presence of a simple horst on the CSEM response of a homogeneous conductive earth is significant, even when the height of the horst is only a fraction of the skin depth of the model. When the transmitter is placed on top of the horst, the currents induced therein account for nearly all of the total magnetic field of the model, indicating that topography, like mutual coupling must be accounted for when interpreting CSEM data.

To the Colonel, and early morning street sweepers...

ACKNOWLEDGMENTS

I would first and foremost like to thank my advisor, Dr. Mark Everett, for his assistance and his uncanny ability to lucidly explain the most obtuse of concepts. I also thank Dr. Greg Newman for his patience with a neophyte in the world of electromagnetic physics during the summer of 2001. Of course, I must also express my gratitude to the entire Geology Department of College of Charleston, South Carolina, whose unique attention to undergraduate student research left me well prepared for graduate school. In particular, I am grateful for the help of Dr. Robert Nusbaum, who guided me through the trials and tribulations of life as an undergraduate student, and Dr. A. Kem Fronabarger, who was my fencing partner, and the person who introduced to the world of geophysics.

To my wife, Nicole Stalnaker, I am forever indebted for her attention to my health and happiness, and her tolerance of my pursuit of education. I thank my parents, David and Amelia Stalnaker, my brother and sisters, and my family-in-law for their support and encouragement. I should acknowledge also my infant son, Koren, the care of whom has afforded me many hours to devote to the review of literature.

The work presented in this dissertation was supported financially by the National Science Foundation (NSF), and by the Strategic Environmental Research abd Development Program (SERDP).

TABLE OF CONTENTS

LIST OF FIGURES

FIGURE Page

LIST OF TABLES

TABLE Page

CHAPTER I

INTRODUCTION

The electrical and magnetic properties of the subsurface, including electrical permittivity ϵ, magnetic permeability μ, and conductivity σ vary from material to material. These quantities are indicative of various properties of the material including the availability and mobility of free electrons and the ease with which the material may become magnetized or electrically polarized. In turn, these properties can be related to less abstract geological conditions, such as lithology, porosity, permeability, and structure. It is the duty of the electromagnetic geophysicist to measure the electromagnetic properties remotely, and to interpret the measured data in order to characterize the subsurface.

Conductivity is the most variable of the electromagnetic properties of typical earth materials, which range from highly conductive metallic ore minerals, to slightly conductive crystalline minerals such as quartz. In fact, conductivity within the Earth spans 20 orders of magnitude. Despite this great range, it is often difficult to relate measured conductivity to lithology. That is, if the conductivity of a region of the subsurface is known, the lithology of that region is not necessarily known. Porosity and permeability (and thus water content), for example, often dwarf the contribution of the actual mineral chemistry to the average conductivity, causing what may normally be a poorly conductive (when dry) mineral appear to be several orders of magnitude more conductive than it actually is (Grant and West, 1965).

A variety of methods have been developed to remotely measure the conductivity (or its reciprocal, resistivity) of the subsurface. Direct current (DC) resistivity, induced polarity (IP), spontaneous potential (SP), controlled-source induction (CSEM), and magnetotelluric induction (MT) are the most commonly used. CSEM offers several advantages over direct-current resistivity surveys: less manpower is required, and larger areas may be surveyed

---

This dissertation follows the style and format of Geophysics.

within the same amount of time (McNeill, 1980a). Several examples of CSEM devices are the Geonics EM-31, EM-34, and ProTEM 47.

CSEM methods for investigating subsurface geology began in earnest in the 1950's and 1960's with the advent of airborne systems mainly for mining applications. Later, with the development of portable and inexpensive ground-based instruments, CSEM systems were applied to groundwater prospecting in arid or hard-rock environments. Due to the upsurge in interest in environmental applications in the past one or two decades, the CSEM method is currently experiencing a rapid growth in use by hydrogeologists, civil and geotechnical engineers, and engineering geologists.

CSEM methods have been successfully applied to a range of tasks, including mapping permafrost, gravel, salt intrusions, cavities in carbonate rocks, contaminant plumes in groundwater, bedrock topography, general geological mapping, archaeological exploration, and the location of buried metallic targets (i.e. pipes and drums) (McNeill, 1980a). Case histories can be found in Hoekstra and Blohm (1990), Buselli et al. (1990), and Senos Matias et al. (1994).

The CSEM method was originally developed for mining applications in which conductive ore bodies form excellent, compact targets within resistive host crystalline rocks. The CSEM method is also able to identify conductive fracture zones in crystalline bedrock aquifers for groundwater prospecting applications. However, generic geological site characterization problem is very difficult. The subsurface geology contains quasi-localized features such as the weathered mantle, bedrock, bedding planes, faults, joints, fracture zones in addition to continuously distributed textural and compositional variations. It is the difficult task of the EM geophysicist to interpret such CSEM responses in terms of the subsurface geology with its attendant spatial complexity. The presence of man-made conductors in the subsurface adds to the difficulty.

Although the physics is well understood, the governing Maxwell's equations become difficult to solve analytically for all but the simplest conductor geometries, such as a homogeneous halfspace, a sphere, or a layered earth. The response of models of only moderate complexity, such as those in figure 1.1, commonly encountered in environmental and engineering scale geophysical surveys, cannot be calculated analytically; numerical methods must be applied to investigate the response of these, and more complex, conductivity models. Numerical solutions designed to calculate the CSEM response of a fully three-dimensional (3-D) earth include integral equation solutions (Weidelt, 1975; Avdeev et al., 1997), finite difference approximations (Wang and Hohmann, 1993; Newman and Alumbaugh, 1995), and finite element solutions (Badea et al., 2001; Pridmore et al., 1981), each of which has its advantages and disadvantages. New solutions are motivated by the complexity of the true distribution of conductivity the earth, computation efficiency, and potential economic and environmental benefits.

Three-dimensional modeling of the response of an arbitrary conductivity distribution is currently computationally expensive, rendering it impractical for routine interpretation of field data. However, in addition to accurately modeling the response of an arbitrary 3-D conductivity, a functioning 3-D modeling algorithm may be used to investigate poorly understood issues associated with CSEM geophysics. Model parametric studies may be conducted to explore the effect of target conductivity, host conductivity, transmitter size, frequency, and moment on the measured response. The effect of mutual coupling between conductive targets and the impact of topography on the CSEM response may also be assessed, for example.

Objectives of This Study

The primary objective of this study is to design, implement, and validate a computer algorithm, based on borehole induction work by Badea and others (2001), that will provide the CSEM response of an arbitrary 3-D conductivity model in the frequency and time domains, using the finite element method. This algorithm will then be used to explore some of the issues outlined above, focusing in particular on the effects of topography and the mutual interaction of multiple buried targets on the CSEM response.

The Galerkin finite element method is used to numerically model the response of a fully

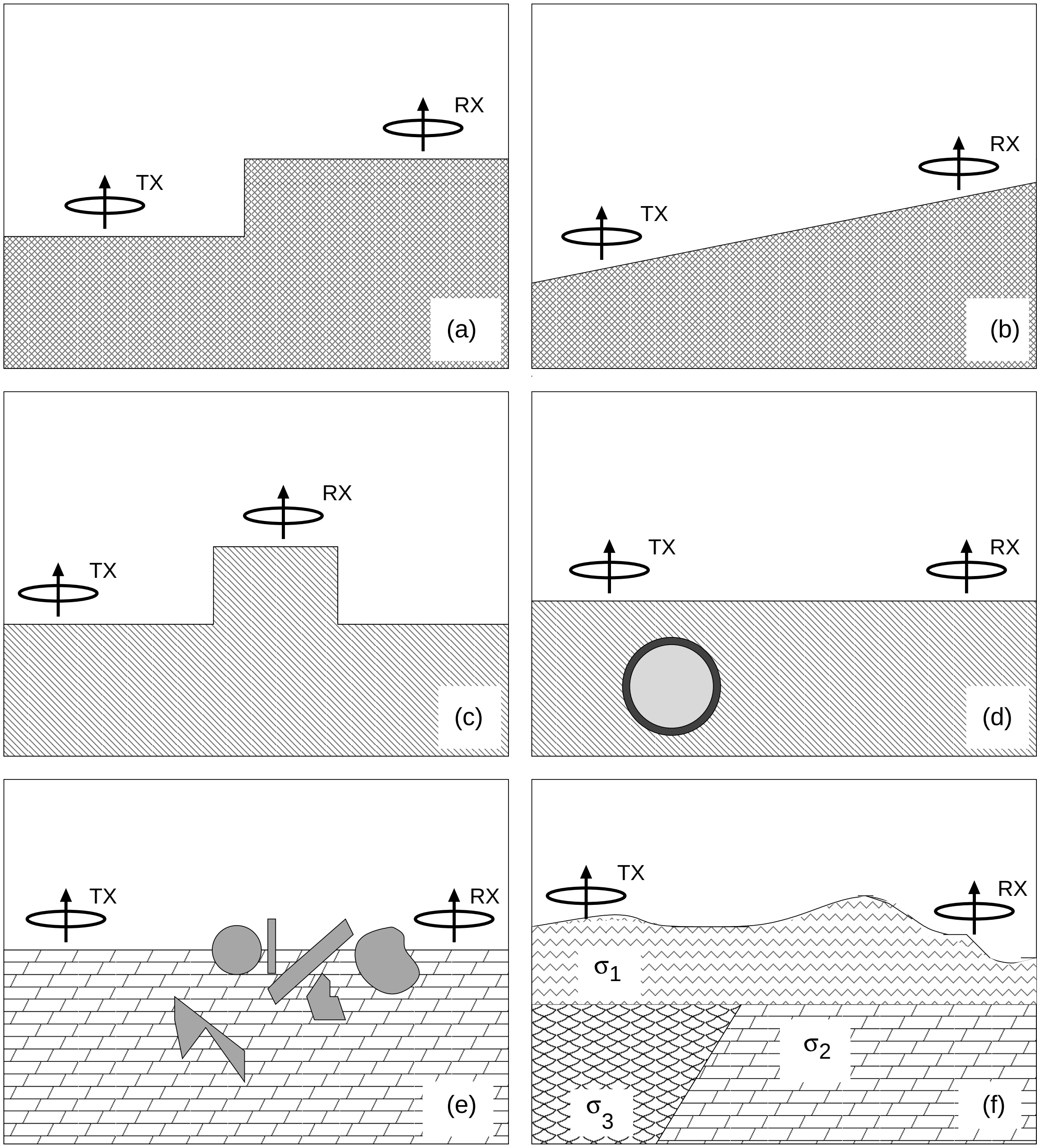

Fig. 1.1. Three-dimensional conductivity models. One of the goals of the research presented herein is to create a finite element algorithm capable of calculating the response of models such as these.

three-dimensional conductivity distribution. Finite element and finite difference solutions produce comparable results. However, the finite element method allows the solution domain to be broken down into a completely unstructured mesh, wherein the element boundaries can be made to conform to the irregular shapes characteristic of realistic conductors three dimensional conductor geometries, including the effect of topography, subsurface geology, and so-called "cultural" conductors such as metallic debris. Furthermore, the mesh may be locally refined, providing finer mesh resolution where it is needed.

As a form of quality control, the fully three-dimensional finite element algorithm is gradually increased in complexity from simple one-dimensional test problems to three-dimensional scalar and vector test problems. Subsequently, the algorithm is applied to the one-dimension CSEM problem, and finally, to the fully three-dimensional CSEM problem. Each phase is verified against known solutions before proceeding. The algorithm is verified against a semi-analytic solution for a double halfspace (Ward and Hohmann, 1987), and against published numerical model results for a fully three-dimensional conductivity (Pridmore et al., 1981).

In order to simplify calculations, Maxwell's equations are reformulated in terms of a frequency-domain magnetic vector potential and a scalar electric potential. The potentials and the the conductivities are divided into a known primary portion and an unknown secondary portion. The fields, defined as spatial derivatives of the potential, are recovered using both simple node differencing and moving least squares interpolation (Tabarra et al., 1994). Although the finite element algorithm is formulated in the frequency-domain, conversion to the time domain is achieved by inverse Fourier transforming the frequency domain data (Newman et al., 1986). The time domain responses of several 3-D models are evaluated.

The finite element algorithm is then used to investigate the effects of mutual induction between multiple buried targets and the host medium. The currents induced in one conductive target will affect the currents flowing in another target via the process of mutual induction. If the host is conductive, currents also flow therein, adding to the complexity of the interaction between targets. The combined effect of these two processes has been dubbed the “mutual coupling”. The effect of mutual induction between multiple targets is poorly understood, and often the host effect is wholly neglected, largely due to lack of availability of a fully three-dimensional forward modeling code.

The targets chosen are plates buried at a shallow depth, and assigned a conductivity similar to aluminum. A realistic transmitter and range of host medium conductivities were modeled as well. Three different model configurations were investigated, each containing two identical plates, including a model with two parallel vertical plates (VVP), a model with with a vertical and a horizontal plate perpendicular to one another (VHP), and a model with two horizontal plates (HHP).

An understanding of the effect of mutual induction on the response measured by a controlled-source electromagnetic device is vital to the correct interpretation of field data in field sites containing multiple targets buried in close proximity to one another. The results presented herein show that mutual coupling is significant and may not be ignored. Furthermore, it is shown that the presence of a conductive host medium also has a significant effect on the controlled-source response. The effect of mutual coupling is of particular interest in circumstances where the correct interpretation of field data is not only desired, but required in order to prevent injury of the loss of life. The detection and discrimination of unexploded ordnance (UXO) is one example, where field sites often contain a great deal of exploded ordnance fragments (frag) that, through the processes of mutual coupling, may distort the expected response of the UXO.

Lastly, the finite element foward model is used to explore the effects of topography on the CSEM response. A simple horst model of variable height is presented. The effect of the presence of the horst is calculated for several transmitter locations. The horst is shown to have a significant impact on the total magnetic field of the model, particularly when the transmitter is located on top of the horst, even when the horst is small relative to the dimensions of the model. Thus an interpretation of field data that does not account for topography may be erroneous.

CHAPTER II

THE ELECTROMAGNETIC INDUCTION PROBLEM

The phenomenon of electromagnetic induction is described concisely by Maxwell's equations:

$$\nabla \cdot \mathbf{E} = \frac{1}{\epsilon}\rho \tag{2.1}$$

$$\nabla \cdot \mathbf{H} = 0 \tag{2.2}$$

$$\nabla \times \mathbf{E} = -\mu\frac{\partial \mathbf{H}}{\partial t} \tag{2.3}$$

$$\nabla \times \mathbf{H} = \mathbf{J} + \epsilon\frac{\partial \mathbf{E}}{\partial t} \tag{2.4}$$

where $\mathbf{E}$ is the electric field, $\mathbf{H}$ is the magnetic field, ρ is the charge density, ϵ is the electric permittivity, and $\mathbf{J}$ is the current density. Several other constitutive relationships constrain these equations:

$$\mathbf{B} = \mu\mathbf{H} \tag{2.5}$$

$$\mathbf{J} = \sigma\mathbf{E} \tag{2.6}$$

where $\mathbf{B}$ is the magnetic induction, μ is the magnetic permeability, and σ is the conductivity.

The entirety of electrodynamics is described by Maxwell's equations. A more thorough treatment of electrodynamic theory may be found in Griffiths (1999). Gauss's law, equation 2.1, states that an electric field diverges away from a collection of positive charges, and toward a collection of negative charges. Despite diligent investigation, magnetic charges have never been observed in nature. Therefore, all magnetic fields must be divergence-free (equation 2.2). A time-varying magnetic field induces an electric field that curls around the magnetic field. This is Faraday's law (equation 2.3). Magnetic fields curl around current densities, and are induced by time varying electric fields, according to equation 2.4, originally stated by Ampere and revised by Maxwell.

Magnetic permeability μ can be approximated by μ_0, the magnetic permeability of free space, for most rocks and minerals. Thus equation 2.5 can be rewritten as

$$\mathbf{B} = \mu_0 \mathbf{H}. \tag{2.7}$$

It should be noted that equation 2.6 is the generalization of Ohm's law to volumetric currents, and that this is not a true law, but an empirical relationship that holds true for most linear isotropic conductors. Ohm's law states that an electric field $\mathbf{E}$ fluxing through a conductor will cause a current density $\mathbf{J}$ to flow therein, the magnitude of which is determined by the conductivity σ. Conductivity, then, is a constant of proportionality specific to the material. It reflects the availability and mobility of free charge carriers within the material.

If an external source of current $\mathbf{J}_P$ exists, as is the case for CSEM, it must be included in equation 2.4. Substituting 2.6 into 2.4 yields:

$$\nabla \times \mathbf{H} = \mathbf{J} + \epsilon \frac{\partial \mathbf{E}}{\partial t} = \mathbf{J}_S + \mathbf{J}_P + \epsilon \frac{\partial \mathbf{E}}{\partial t} = \sigma \mathbf{E} + \mathbf{J}_P + \epsilon \frac{\partial \mathbf{E}}{\partial t} \tag{2.8}$$

where $\mathbf{J}_S$ is the induced current, and $\mathbf{J}_P$ is the external (or source) current.

If a region is of non-vanishing conductivity, any charge buildup caused by current flow will reach a state of equilibrium very rapidly ($t \approx \epsilon/\sigma$) (Grant and West, 1965). Thus, taking the divergence of 2.8 yields:

$$\nabla \cdot \mathbf{J} = -\frac{\partial \rho}{\partial t} = 0, \tag{2.9}$$

which implies that

$$\nabla \cdot (\sigma \mathbf{E}) = 0 \tag{2.10}$$

if the source current density is divergence-free. This condition is satisfied by inductively coupled magnetic dipole controlled sources, but not by electric dipole sources.

Taking the curl of equations 2.3 and 2.8 and substituting each into the other produces the damped wave equations:

$$\nabla \times \nabla \times \mathbf{E} + \mu_0 \sigma \frac{\partial \mathbf{E}}{\partial t} + \mu_0 \epsilon \frac{\partial^2 \mathbf{E}}{\partial t^2} = -\mu_0 \frac{\partial \mathbf{J}_P}{\partial t} \tag{2.11}$$

$$\nabla \times \nabla \times \mathbf{H} + \mu_0 \sigma \frac{\partial \mathbf{H}}{\partial t} + \mu_0 \epsilon \frac{\partial^2 \mathbf{H}}{\partial t^2} = \nabla \times \mathbf{J}_P. \tag{2.12}$$

The second term on the left hand side of equations 2.11 and 2.12 describes diffusion of energy from **E** and **H** respectively, and the third term describes wave propagation at velocity $c = 1/\sqrt{\epsilon_0 \mu_0}$.

Calculation of the electric and magnetic fields may be simplified by Fourier transforming Maxwell's equations to the frequency domain.

$$\int_{-\infty}^{+\infty} (\nabla \times \mathbf{H}(\omega)) e^{i\omega t} d\omega = \int_{-\infty}^{+\infty} [(\sigma \mathbf{E}(\omega) + \mathbf{J}_P(\omega)) e^{i\omega t} + \epsilon \mathbf{E}(\omega) \frac{\partial e^{i\omega t}}{\partial t}] d\omega \tag{2.13}$$

$$\int_{-\infty}^{+\infty} (\nabla \times \mathbf{E}(\omega)) e^{i\omega t} d\omega = \int_{-\infty}^{+\infty} (-\mu_0 \mathbf{H}(\omega) \frac{\partial e^{i\omega t}}{\partial t}) d\omega \tag{2.14}$$

Equating the integrands yields Maxwell's equations in the frequency domain:

$$\nabla \times \mathbf{H}(\omega) = \sigma \mathbf{E}(\omega) + \mathbf{J}_P(\omega) + i\omega\epsilon \mathbf{E}(\omega) \tag{2.15}$$

$$\nabla \times \mathbf{E}(\omega) = -i\omega\mu_0 \mathbf{H}(\omega) \tag{2.16}$$

$$\nabla \cdot \mathbf{H}(\omega) = 0 \tag{2.17}$$

$$\nabla \cdot \mathbf{E}(\omega) = \frac{1}{\epsilon} \rho \tag{2.18}$$

The time domain equations may be recovered by an inverse Fourier transform. This is not a purely mathematical exercise. CSEM investigations may be conducted in either the frequency domain or the time domain. (This can readily be demonstrated by assuming that source current is sinusoidal with an $e^{i\omega t}$ time dependence, indicating that $\mathbf{H} = \mathbf{H}_0 e^{i\omega t}$, $\mathbf{E} = \mathbf{E}_0 e^{i\omega t}$, and $\mathbf{J} = \mathbf{J}_0 e^{i\omega t}$. Substitution into Maxwell's equations in the time domain returns equations 2.15–2.18.)

The frequency domain form of Maxwell's equations may also be rewritten as a pair of damped-wave equations by again taking the curls of Ampere's Law, equation 2.15, and Faraday's Law, equation 2.16, and substituting each into the other:

$$\nabla \times \nabla \times \mathbf{E}(\omega) + i\omega\mu_0\sigma\mathbf{E}(\omega) - \omega^2\mu_0\epsilon = -i\omega\mu_0\mathbf{J}_P(\omega) \tag{2.19}$$

$$\nabla \times \nabla \times \mathbf{H}(\omega) + i\omega\mu_0\sigma\mathbf{H}(\omega) - \omega^2\mu_0\epsilon\mathbf{H}(\omega) = \nabla \times \mathbf{J}_P(\omega) \tag{2.20}$$

The electric permittivity ϵ is generally quite small for most rocks, on the order of 10^{-11} F/m. Conductivity is, in general, much higher ($\geq 10^{-2}$ S/m for most targets of interest). Therefore, at low frequencies, where $f < 10^5$ Hz, the displacement current term in equations 2.11, 2.12, 2.19, and 2.20 is dominated by the diffusion term, and can be neglected. This is the quasistatic approximation. It is assumed that all CSEM investigations discussed in this study are conducted using a frequency within the quasistatic range, allowing the diffusive Maxwell's equations to be written as

$$\nabla \times \mathbf{H}(\omega) = \sigma\mathbf{E}(\omega) + \mathbf{J}_P(\omega) \tag{2.21}$$

$$\nabla \times \mathbf{E}(\omega) = -i\omega\mu_0\mathbf{H}(\omega) \tag{2.22}$$

$$\nabla \cdot \mathbf{H}(\omega) = 0 \tag{2.23}$$

$$\nabla \cdot \mathbf{E}(\omega) = \frac{1}{\epsilon}\rho \tag{2.24}$$

The (A-Ψ) Potential Formulation of Maxwell's Equations

It is possible to formulate finite element solutions of Maxwell's equations directly in terms of the electric and magnetic field vectors **E** and **H** , or in terms of the coupled vector-scalar potentials. Either formulation must ensure that the normal component of **E** be allowed to "jump" at material interfaces, and that the solution contains no purely divergent "spurious modes" (Sun et al., 1995).

If the solution is formulated in terms of **E** and **H** , these conditions may be satisfied by the application of penalty functions to the EM field divergence (Zanoubi et al., 1999), or by using vector-based "edge" elements (Barton and Cendes, 1987; Sugeng et al., 1999) that are divergence-free, and cannot support spurious modes (Badea et al., 2001). In addition, edge elements allow the electric field to be discontinuous across material boundaries. Alternatively, the electromagnetic induction problem may be rephrased in a coupled-potential formulation. Several different coupled-potential formulations are available, and the appropriate choice depends on the nature of the problem to be solved. A review of coupled-potential formulations is available in Biro and Richter (1991). In this study, the ($\mathbf{A}$,Ψ) coupled-potential formulation is used, where $\mathbf{A}$ is the magnetic vector potential, and Ψ is the scalar electric potential.

The Helmholtz theorem states that if the divergence and the curl of a differentiable vector function are specified, that vector function may be written as the gradient of a scalar plus the curl of a vector

$$\mathbf{F} = \nabla U + \nabla \times \mathbf{W}$$

where U is the scalar potential of $\mathbf{F}$ and is a function of the divergence of $\mathbf{F}$, and $\mathbf{W}$ is the vector potential of $\mathbf{F}$, and is a function of the curl of $\mathbf{F}$. Thus, the magnetic induction $\mathbf{B}$ may be represented by a vector potential

$$\mathbf{B}(t) = \nabla \times \mathbf{A}(t) \quad \Longleftrightarrow \quad \mathbf{B}(\omega) = \nabla \times \mathbf{A}(\omega). \tag{2.25}$$

Substituting 2.25 into 2.3 reveals a quantity the curl of which is zero:

$$\nabla \times \mathbf{E} = -\frac{\partial}{\partial t}(\nabla \times \mathbf{A}) \tag{2.26}$$

$$\nabla \times \left(\mathbf{E} + \frac{\partial \mathbf{A}}{\partial t}\right) = 0. \tag{2.27}$$

As it is irrotational, this quantity may be represented by the gradient of a scalar Φ:

$$\mathbf{E}(t) = -\frac{\partial \mathbf{A}(t)}{\partial t} - \nabla\Phi(t) \quad \Longleftrightarrow \quad \mathbf{E}(\omega) = -i\omega\mathbf{A}(\omega) - \nabla\Phi(\omega). \tag{2.28}$$

The scalar electric potential Φ can be rewritten as $\Phi = i\omega\Psi$ allowing the electric field to be written more concisely:

$$\mathbf{E} = -i\omega(\mathbf{A} + \nabla\Psi). \tag{2.29}$$

Equation 2.7 is substituted into 2.21:

$$\nabla \times \mathbf{B} = \mu_0(\mathbf{J}_P + \sigma\mathbf{E}) \tag{2.30}$$

and equations 2.25 and 2.29 are substituted into 2.30:

$$\nabla \times \nabla \times \mathbf{A} + i\omega\mu_0\sigma(\mathbf{A} + \nabla\Psi) = \mu_0\mathbf{J}_P \tag{2.31}$$

yielding three equations in four unknowns. The final equation is obtained by substituting 2.29 into 2.10:

$$\nabla \cdot [i\omega\mu_0\sigma(\mathbf{A} + \nabla\Psi)] = 0. \tag{2.32}$$

The gradient of any scalar function λ may be added to $\mathbf{A}$ provided the time derivative of that scalar function is subtracted from Φ. This behavior may be exploited, causing the divergence of $\mathbf{A}$ to vanish:

$$\nabla \cdot \mathbf{A} = 0 \tag{2.33}$$

This is the Coloumb gauge. The Coulomb gauge 2.33 and a vector identity $\nabla \times \nabla \times \mathbf{A} = \nabla(\nabla \cdot \mathbf{A}) - \nabla^2\mathbf{A}$ are applied to equation 2.31:

$$\nabla^2\mathbf{A} - i\omega\mu_0\sigma(\mathbf{A} + \nabla\Psi) = \mu_0\mathbf{J}_P \tag{2.34}$$

The potentials $\mathbf{A}$ and Ψ may be divided into a known primary portion due to a primary conductivity distribution $\sigma_P(\mathbf{r})$ and the source current density $\mathbf{J}_P$, and an unknown secondary component arising from a secondary conductivity distribution σ_S:

$$\mathbf{A} \equiv \mathbf{A}_P + \mathbf{A}_S \tag{2.35}$$

$$\Psi \equiv \Psi_P + \Psi_S \tag{2.36}$$

$$\sigma \equiv \sigma_P + \sigma_S \tag{2.37}$$

Because the primary potentials are defined as

$$\nabla^2 \mathbf{A}_P - i\omega\mu_0\sigma_P(\mathbf{A}_P + \nabla\Psi_P) = \mu_0 \mathbf{J}_P \tag{2.38}$$

$$\nabla \cdot [-i\omega\mu_0\sigma_P(\mathbf{A}_P + \nabla\Psi_P)] = 0 \tag{2.39}$$

the source current density no longer must be explicitly defined, and may be of arbitrary shape, size, or orientation. The secondary formulation also makes readily apparent the contribution of the secondary conductivity to the total potentials or fields. The primary potentials are generally analytic solutions for a source in free space or a layered conductivity distribution $\sigma_P(z)$ (Badea et al., 2001).

The governing equations for the primary potentials, 2.38 and 2.39, and the definitions 2.36 are substituted into the equations 2.32 and 2.34:

$$\nabla^2 \mathbf{A}_S - i\omega\mu_0\sigma(\mathbf{A}_S + \nabla\Psi_S) = +i\omega\mu_0\sigma_S(\mathbf{A}_P + \nabla\Psi_P) \tag{2.40}$$

$$\nabla \cdot [-i\omega\mu_0\sigma(\mathbf{A}_S + \nabla\Psi_S)] = \nabla \cdot [+i\omega\mu_0\sigma_S(\mathbf{A}_P + \nabla\Psi_P)] \tag{2.41}$$

These are the governing equations for the secondary magnetic vector potential $\mathbf{A}_S$ and the secondary electric potential Ψ_S in the Coulomb gauge. The 4×4 system of equations will be solved numerically for the secondary magnetic and electric potentials resulting from an arbitrary conductivity distribution σ_S energized by an inductively-coupled current density $\mathbf{J}_P$.

The Controlled-Source Electromagnetic Method

The description of a controlled-source electromagnetic field experiment is contained mathematically in Maxwell's equations. Data may be collected in either the time domain or the frequency domain. Although both time and frequency domain data collection ultimately return the conductivity of the subsurface, the methods differ in ease and speed of data collection, depth of penetration, and susceptibility to ambient electromagnetic noise. In-depth explanations of CSEM methods may be found in Grant and West (1965) and Nabighian (1988; 1991).

In the frequency domain, a sinusoidally alternating current $\mathbf{J}_P$ of frequency ω is passed through a transmitter coil. A primary magnetic field $\mathbf{H}_P$, also varying with frequency ω, arises from the source current according to Ampere's law (equation 2.15), and fluxes through the earth. An electric field is induced by the time-varying magnetic field, according to Faraday's law (equation 2.16), that curls around the magnetic field. Ohm's Law (2.6) states that a secondary current density $\mathbf{J}$ (also called the eddy current) will result from the electromotive force (EMF) caused by the electric field, the strength and phase of which depends on the conductivity of the subsurface $\sigma(\mathbf{r})$. The current density within a highly conductive zone is 90° out of phase with the source current density. As conductivity approaches zero, the phase lag of the secondary current also approaches zero.

The secondary current density will give rise to a secondary (or scattered) magnetic field $\mathbf{H}_S$, again in accordance with Ampere's law. Both the primary and secondary fields flux through the receiver coil, causing an EMF, or voltage, that is measured by the receiver. The secondary currents that are induced in the earth are proportional to conductivity. Therefore, the voltage measured at the receiver is also proportional to conductivity (see figure 2.1).

In the time domain, a steady current is slowly turned on in the transmitter coil. The slow turn on time limits the secondary current density induced in the subsurface by the $\partial\mathbf{H}/\partial t$ associated with the rising current in the transmitter. After the current has remained on sufficiently long for the turn-on currents to dissipate, it is rapidly shut off, causing a large

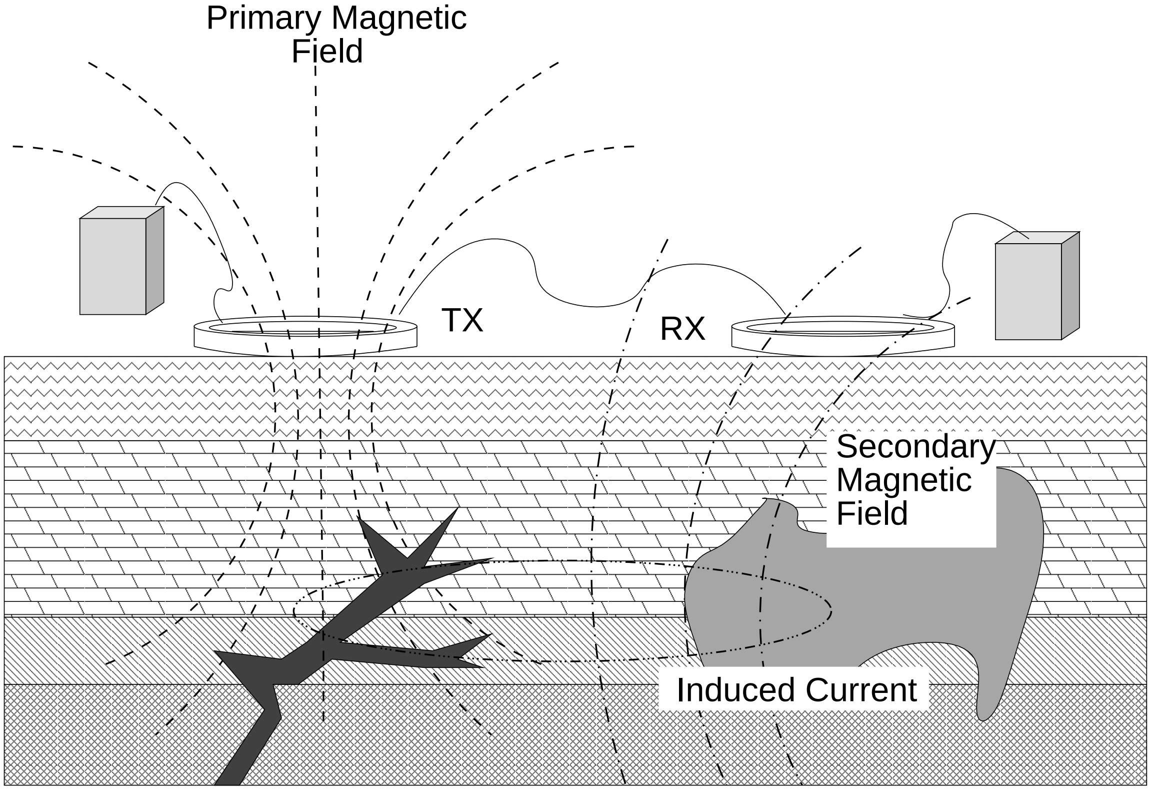

Fig. 2.1. A frequency domain CSEM experiment.

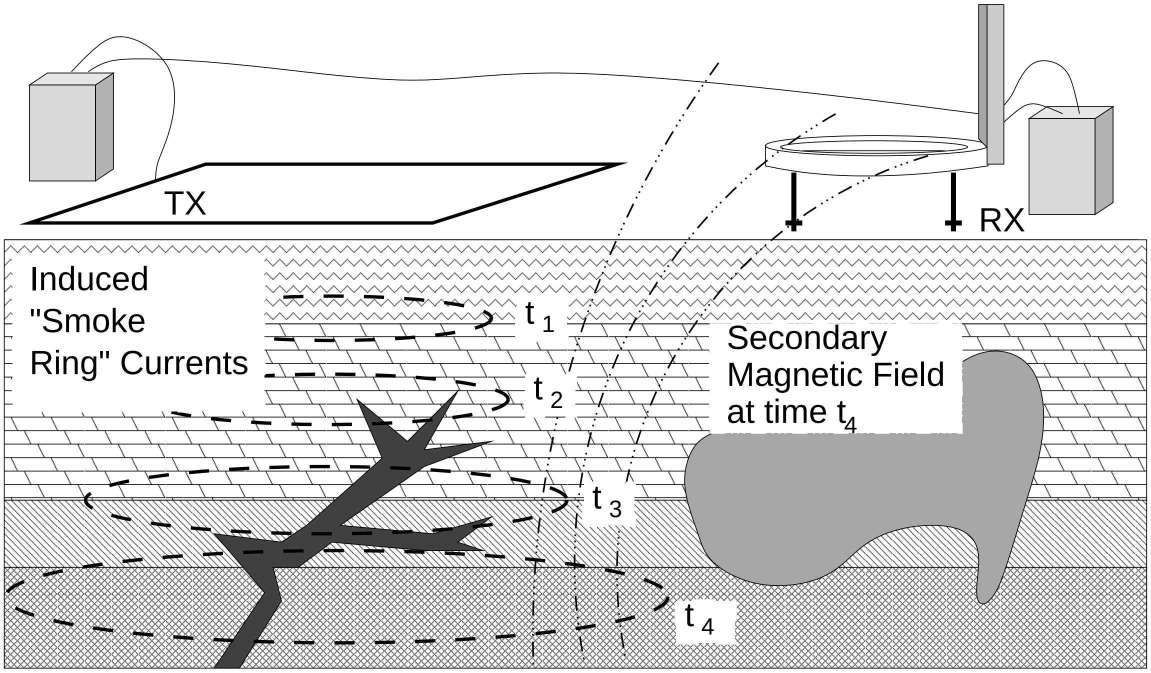

Fig. 2.2. A time domain CSEM experiment.

change in the primary magnetic field, and consequently, a large EMF in the subsurface. The EMF, in turn, causes secondary currents to flow in the subsurface that initially seek to maintain the magnetic field that existed prior to shut-off, according to Lenz's law. These currents immediately begin to decay due to resistive heat loss at a rate determined by the conductivity distribution of the subsurface. Additionally, the eddy currents diffuse downward and outward away from the transmitter, in a manner similar to the behavior of a smoke ring, effectively providing a depth sounding of the subsurface. The secondary current density generates a secondary magnetic field that is measured at the receiver (McNeill, 1980b; Nabighian and Macnae, 1991) (see figure 2.2).

The anomalous current flow in the subsurface falls into two categories. If a conductor floating in free space is subjected to a time-varying primary magnetic field, the currents that are generated flow in closed loops and result from the flux of the primary magnetic field through the conductor. These currents are called vortex currents, because the currents flow in toroidal vortices within the conductor. The large conductivity contrast with the

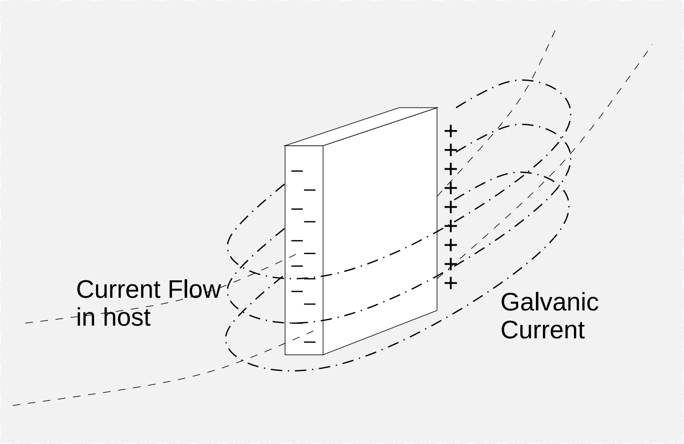

Fig. 2.3. Galvanic current flow.

surrounding, insulating free space prohibits the existence of any current component normal to the conductor surfaces.

If a conductor is present within a conductive medium, a second type of current flow exists. The conductivity contrast between the host medium and the conductor causes a charge buildup on the boundary of the conductor as the vortex currents flowing in the host encounter and flow through the boundary. A current density begins to flow (figure 2.3) in an attempt to neutralize the charge buildup, producing a secondary electric field that attempts to cancel the electric field of the transmitter. A secondary magnetic field arises from the current according to Ampere's law in addition to the secondary magnetic field that exists due to the vortex current flow within the host and the conductive body. Because the galvanic currents flow both through the host and the conductor, it is affected by the conductivity of both, the orientation of the conductor with respect to the primary electric field, and the size and shape of the conductor.

CHAPTER III

FINITE ELEMENT ANALYSIS

The Coulomb-gauged secondary potential formulation of Maxwell's equations, 2.40 and 2.41, are difficult to solve analytically for all but the simplest conductivity distributions. For example, analytic and semi-analytic solutions exist for the potentials in a homogeneous wholespace, a homogeneous halfspace, a sphere, and a layered earth. For more complex conductivity geometries, numerical methods must be employed to approximate the solution of Maxwell's equations.

Published numerical algorithms designed to calculate the electromagnetic response of a fully three dimensional conductivity include integral equation, finite difference, and finite element methods. Integral equation, semi-analytic, and series solutions are fast and efficient (Avdeev et al., 1997; Zhdanov et al., 1999; Weidelt, 1975), but are limited to certain conductor geometries, such as one or more buried prismatic bodies in a layered host. The finite difference method is capable of calculating the response of an inhomogeneous earth (Wang and Hohmann, 1993; Newman and Alumbaugh, 1995; Smith, 1996; Newman, 1999), and is similar in solution accuracy, execution speed, and storage requirements to the finite element method (Badea et al., 2001). However, the finite difference method requires a regular, structured mesh that does not allow accurate simulation of the irregularities of real subsurface conductors. On the other hand, the finite element method permits the discretization of the solution domain into a completely unstructured mesh, allowing element boundaries to conform to the boundaries of real irregular inhomogeneities, such as topography, conductive cultural debris, and small-scale lithological changes.

The computational resources required by the finite element method have until recently made it largely impractical for geophysical applications. The method has, however, been exploited in electrical engineering applications (Biro and Preis, 1989; Boyse et al., 1993; Mur, 1993). Finite element analysis is also extant in the geophysical literature (Badea et al., 2001; Pridmore et al., 1981; Everett and Schultz, 1996; Everett and Weiss, 2002;

Everett et al., 2001).

The Weak Formulation

The finite element method is first described for a generic partial differential equation,

$$\mathscr{L}u = f, \tag{3.1}$$

where $\mathscr{L}$ is an unspecified differential operator. If a function ν is in the range of the operator $\mathscr{L}$, then the equality

$$(\nu, \mathscr{L}u) = (\nu, f) \tag{3.2}$$

is valid for any ν if it is true for all ν that form a spanning set of the range of the operator $\mathscr{L}$ (Silvester and Ferrari, 1996). The notation (a, b) indicates a general inner product, and equation 3.2 is a strong projective formulation of equation 3.1. However, it is often much simpler to define a larger Hilbert space $\mathscr{W}$ containing the range of the operator $\mathscr{L}$, so that the equality

$$(\nu, \mathscr{L}\bar{u}) = (\nu, f), \qquad \nu \in \mathscr{W} \tag{3.3}$$

is satisfied. This is the weak formulation of equation 3.1, and $\bar{u}$ is the weak solution of the differential equation.

An approximate weak solution may be found by solving equation 3.1 for a M-dimensional subspace $\mathscr{W}_{RM}$ of the Hilbert space $\mathscr{W}$, where the subscript R indicates that the subspace pertains to the range of $\mathscr{L}$. If a set of functions β_i span the entire subspace $\mathscr{W}_{RM}$, then any function g that is an element of $\mathscr{W}_{RM}$ may be exactly expressed as a linear combination of those spanning functions, such that

$$g = \sum_{i=1}^{M} g_i \beta_i \tag{3.4}$$

(Silvester and Ferrari, 1996). Equation 3.4 is only exact if g is an element of $\mathscr{W}_{RM}$. As the subspace $\mathscr{W}_{RM}$ is only an approximate representation of the range of $\mathscr{L}$, the approximate weak formulation of equation 3.1 is

$$(\beta_i, \mathscr{L}\bar{u}) = (\beta_i, f), \qquad \beta_i \in \mathscr{W}_{RM}. \tag{3.5}$$

The solution (or domain) of the differential equation (3.1) may be forced to lie within another subspace of dimension N of the Hilbert space $\mathscr{W}$, denoted $\mathscr{W}_{DN}$. Similarly, a spanning set for the domain is given by the set of functions α_j. Thus, the approximate solution is

$$\bar{u} = \sum_{j=1}^{N} u_j \alpha_j, \tag{3.6}$$

which is a linear combination of the spanning functions weighted by the numerical coefficients u_j, where $j = 1, \ldots, N$. The finite element expansion is an application of equation 3.6, where the spanning functions are constrained by the criteria presented in the next section. Substituting this equation into the approximate weak solution (3.5) yields a very general finite element formulation of equation 3.1:

$$(\beta_i, \mathscr{L} \sum_{j=1}^{N} u_j \alpha_j) = (\beta_i, f), \qquad i = 1, \ldots, M. \tag{3.7}$$

As Silvester and Ferrari indicate, the subspaces $\mathscr{W}_{RM}$ and $\mathscr{W}_{DN}$ have not been defined explicitly. Nor has anything been said about the size of the degrees of freedom M and N. Suffice it to say that as N and M increase, the solution of equation 3.7 approaches the true solution of equation 3.1. This claim is stated here without proof, but rigorous mathematical proof exists in the finite element literature. The reader is referred to (Johnson, 1987; Kardestuncer, 1987; Mitchell and Wait, 1978) for a more thorough treatment.

Before the subspaces $\mathscr{W}_{RM}$ and $\mathscr{W}_{DN}$ are defined, the following vector analogy is offered as a visualization tool. An arbitrary vector $\mathbf{v}$ is analogous to the range of of the generic differential equation, 3.1. If $\mathbf{v}$ is a three-dimensional vector, then a spanning set of vectors in three-dimensions is provided by the unit vectors $\hat{x}$, $\hat{y}$, and $\hat{z}$. The vector may be exactly represented by its projection onto the unit vectors (figure 3.1), in the same way that the

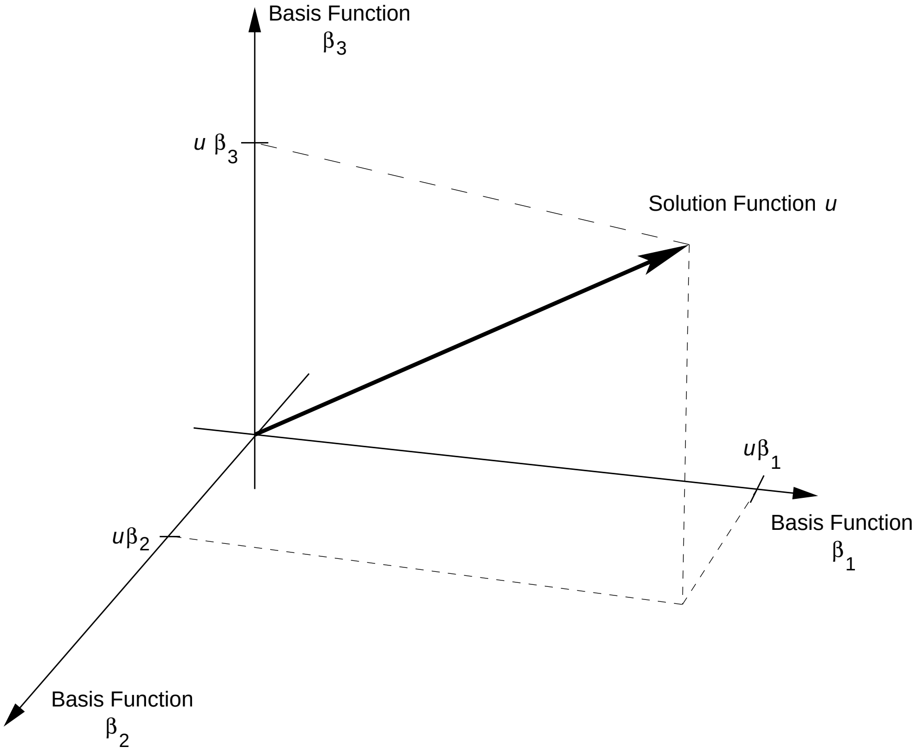

Fig. 3.1. Vector analogy of the projective solution.

range of $\mathscr{L}u$ may be exactly represented by its projection onto a spanning set of functions ν in the strong form of the projective formulation. If the vector is n-dimensional, and its projection onto some subset m of the n unit vectors is known, then the vector may be approximately represented by the m-dimensional projection. As m approaches n, the true vector is better represented. This is analogous to the weak projective formulation of equation 3.1.

The Galerkin Method

A three-dimensional differential equation (3.8) is given by

$$\nabla^2 u(x,y,z) + \tau^2 u(x,y,z) = f. \tag{3.8}$$

The solution to this equation may be approximated by the expansion

$$u(x, y, z) = \sum_{j=1}^{N} u_j \alpha_j(x, y, z). \tag{3.9}$$

It can be noted, after some consideration, that all solutions $u(x, y, z)$ and all source distributions f within a spatial region Ω are members of a subspace of square-integrable functions, and a Hilbert space $\mathscr{W}$ may therefore be formed from the inner product

$$(a, b)_\Omega = \int_\Omega ab \; d\Omega \tag{3.10}$$

(Silvester and Ferrari, 1996). Following the reasoning above, equation 3.8 may be reformulated in the weak sense as

$$\sum_{j=1}^{N} (\beta_i, \nabla^2 \alpha_j)_\Omega \; u_j + \tau^2 (\beta_i, \alpha_j)_\Omega \; u_j = (\beta_i, f)_\Omega. \tag{3.11}$$

The weak form requires that the set of functions α_j be twice-differentiable. In order to simplify the construction of α_j, this constraint is relaxed by applying integration by parts (Green's second identity) to equation 3.11, yielding

$$\sum_{j=1}^{N} [(\beta_i, \nabla \alpha_j)_S - (\nabla \beta_i, \nabla \alpha_j)_\Omega] \; u_j + \tau^2 (\beta_i, \alpha_j)_\Omega \; u_j = (\beta_i, f)_\Omega. \tag{3.12}$$

If the solution or the functions α_j or β_i vanish at the surface S of the spatial region Ω over which the solution is desired, then the surface integral will vanish as well. It will eventually be shown that this condition can always be satisfied. Thus equation 3.12 becomes

$$\sum_{j=1}^{N} -(\nabla \beta_i, \nabla \alpha_j)_\Omega \; u_j + \tau^2 (\beta_i, \alpha_j)_\Omega \; u_j = (\beta_i, f)_\Omega. \tag{3.13}$$

It is no longer requisite that α_j be twice-differentiable; α_j need only be once-differentiable. As a consequence of applying Green's second identity, β_i must also be once-differentiable, whereas it was previously only required to be square-integrable. Thus the range subspace $\mathscr{W}_{RM}$ and the domain subspace $\mathscr{W}_{DN}$ are both subspaces of the once-differentiable subspace, that is itself a subspace of the the square-integrable Hilbert space $\mathscr{W}$. As the application of integration by parts has made the subspaces $\mathscr{W}_{RM}$ and $\mathscr{W}_{DN}$ similar, the Galerkin method goes one step further, and prescribes using the same space for both $\mathscr{W}_{RM}$ and $\mathscr{W}_{DN}$. The simplest—although not the only—way to do this is to set $\alpha_i{=}\beta_i$.

Simplex Elements and Basis Function Construction

A general three-dimensional differential equation is again considered:

$$\nabla^2 u(x,y,z) + \tau^2 u(x,y,z) = f. \tag{3.8}$$

The approximate solution $u(x,y,z)$ is also recalled:

$$u(x,y,z) = \sum_{j=1}^{N} u_j \alpha_j(x,y,z). \tag{3.9}$$

where u_j is the value of u at location j in the solution domain and α_j is an interpolation, or basis, function that provides the approximate value of u in the regions between the locations j.

The solution domain Ω is broken down into a number of discrete elements over which a portion n of the N total nodes are distributed. The elements may be any shape, and any number of nodes may be defined for each element. If there are n nodes assigned to each element, then there are also n orthogonal basis functions equal to one at node j and zero at all other nodes, such that at any given node located at (x_j, y_j, z_j), the solution $u(x_j, y_j, z_j) = u_j$. The value of u in regions between the nodes is given by the linear combination of the n nonzero basis functions, and the values of u at the nodes.

It is reasonable to discretize the solution domain into the simplest possible non-trivial elements, or simplex elements, because for an N-dimensional problem, any polygon or polyhedron may be represented by a subset of simplex elements. That is to say that in a two-dimensional problem, any polygon may be constructed from a number of triangles, and in a three-dimensional problem, any polyhedron may be constructed from a number of tetrahedra. Mathematically, the use of simplex elements allows the choice of basis functions that guarantee the continuity of the solution across all element boundaries. Also, the approximate solution is independent of the placement of the elements within the global coordinate system. In other words, the use of completely unstructured meshes is permitted (Silvester and Ferrari, 1996).

Simplex elements are not without shortcomings, however. A curved surface, for example, may only be approximated by simplex elements. The polynomial basis functions α_j do not approximate rapidly varying functions or singularities well. Finally, unless a vector function $\mathbf{U}(x, y, z)$ is continuous across all material boundaries, as is the case for the vector potential $\mathbf{A}$, then the expansion

$$\mathbf{U}(x, y, z) = \sum_{j=1}^{N} \mathbf{U}_j \alpha_j(x, y, z)$$

is *not* valid. Other element types exist that compensate for these difficulties, including isoparametric elements that have curved sides, non-polynomial basis functions that approximate singularities well, and vector-based edge elements (Silvester and Ferrari, 1996)

A simplex pertaining to an N-dimensional problem is a region of the solution domain defined by $N + 1$ unique vertices. It has a size, defined as

$$\sigma(S) = \frac{1}{N!} \begin{vmatrix} 1 & x_1^{(1)} & x_1^{(2)} & \cdots & x_1^{(N)} \\ 1 & x_2^{(1)} & x_2^{(2)} & \cdots & x_2^{(N)} \\ \vdots & & & & \\ 1 & x_{N+1}^{(1)} & x_{N+1}^{(2)} & \cdots & x_{N+1}^{(N)} \end{vmatrix} \tag{3.14}$$

where the subscript of x denotes the vertex of the simplex, and the superscript refers to the spatial direction. For example, in two dimensions, σ is the area of a triangle, and in three dimensions, σ is the volume of a tetrahedron (Silvester and Ferrari, 1996).

From the size of the simplex, the barycentric coordinates may be derived. A point P within a simplex S of dimension N will define $N + 1$ unique subsimplexes that each have P as a vertex. The sum of the sizes of these subsimplexes is equal to the size of the original simplex. Therefore, the location of P is uniquely defined by the $N + 1$ barycentric coordinates

$$\zeta_i = \frac{\sigma(S_i)}{\sigma(S)} \tag{3.15}$$

where S_i is subsimplex i. If a perpendicular line is drawn from vertex i to the opposing side of the simplex, the coordinate ζ_i measures the relative distance along that line from vertex i to the location of P. Substituting equation 3.14 into equation 3.15 yields the definition of the barycentric coordinates in terms of the Cartesian coordinates of the simplex vertices. In three dimensions, the barycentric coordinates of point (x, y, z) are

$$\zeta_1 = \frac{\begin{vmatrix} 1 & x & y & z \\ 1 & x_2 & y_2 & z_2 \\ 1 & x_3 & y_3 & z_3 \\ 1 & x_4 & y_4 & z_4 \end{vmatrix}}{\begin{vmatrix} 1 & x_1 & y_1 & z_1 \\ 1 & x_2 & y_2 & z_2 \\ 1 & x_3 & y_3 & z_3 \\ 1 & x_4 & y_4 & z_4 \end{vmatrix}} \zeta_2 = \frac{\begin{vmatrix} 1 & x & y & z \\ 1 & x_3 & y_3 & z_3 \\ 1 & x_4 & y_4 & z_4 \\ 1 & x_1 & y_1 & z_1 \end{vmatrix}}{\begin{vmatrix} 1 & x_1 & y_1 & z_1 \\ 1 & x_2 & y_2 & z_2 \\ 1 & x_3 & y_3 & z_3 \\ 1 & x_4 & y_4 & z_4 \end{vmatrix}}$$

$$\zeta_3 = \frac{\begin{vmatrix} 1 & x & y & z \\ 1 & x_4 & y_4 & z_4 \\ 1 & x_1 & y_1 & z_1 \\ 1 & x_2 & y_2 & z_2 \end{vmatrix}}{\begin{vmatrix} 1 & x_1 & y_1 & z_1 \\ 1 & x_2 & y_2 & z_2 \\ 1 & x_3 & y_3 & z_3 \\ 1 & x_4 & y_4 & z_4 \end{vmatrix}} \zeta_4 = \frac{\begin{vmatrix} 1 & x & y & z \\ 1 & x_1 & y_1 & z_1 \\ 1 & x_2 & y_2 & z_2 \\ 1 & x_3 & y_3 & z_3 \end{vmatrix}}{\begin{vmatrix} 1 & x_1 & y_1 & z_1 \\ 1 & x_2 & y_2 & z_2 \\ 1 & x_3 & y_3 & z_3 \\ 1 & x_4 & y_4 & z_4 \end{vmatrix}}. \tag{3.16}$$

It is apparent from equation 3.15 that the barycentric coordinates are invariant under a rotation or translation of the global coordinate system. Although the vertex coordinates may change, the size of the simplex and the subsimplexes defined by point P will not change. The primary advantage of formulating the basis functions in terms of the barycentric coordinates is that the functions need only be constructed once for a general simplex, and extrapolated to any other simplex by means of coordinate transformation rules.

In general, the basis functions α_j are polynomials of degree n with n zeros each, obtaining the value zero at all nodes except j and unity at j, where n is again the number of nodes assigned to each simplex. A function that meets these specifications may be constructed from the auxiliary polynomials of degree n given by

$$R_m(n, \zeta) = \frac{1}{m!} \prod_{k=0}^{m-1} (n\zeta - k), \qquad m > 0 \tag{3.17}$$

$$R_0(n, \zeta) = 1, \tag{3.18}$$

and is itself defined as

$$\alpha_{ijk\ell}(\zeta_1, \zeta_2, \zeta_3, \zeta_4) = R_i(n, \zeta_1) R_j(n, \zeta_2) R_k(n, \zeta_3) R_\ell(n, \zeta_4). \tag{3.19}$$

where the subscripts i, j, k, and ℓ form an “address” for each simplex node, and $i+j+k+\ell =$

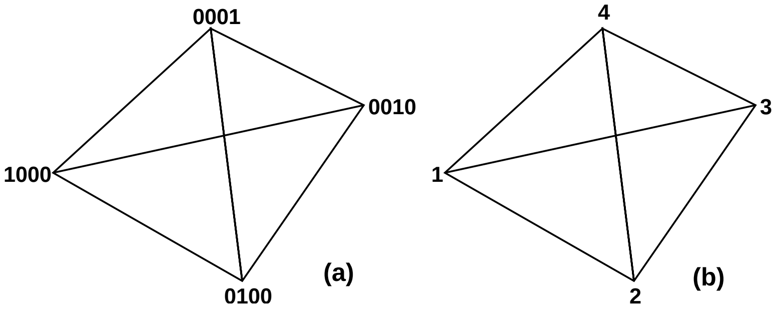

Fig. 3.2. A finite element tetrahedron. The (a) four index numbering scheme used by Silvester and Ferarri (1996), is compared to (b) the equivalent single index scheme.

n. With the sacrifice of some clarity, the subscripts may be collapsed into a single index α_j.

For the sake of simplicity and execution speed, the nodes may be chosen to correspond with the simplex vertices, as in figure 3.2. Also, the mathematics are greatly simplified if the simplest polynomials are chosen as basis functions. If the numbering scheme displayed in figure 3.2 is used to generate basis functions from equation 3.19, this condition is automatically enforced because $i + j + k + \ell = n = 1$. Thus, the basis functions α_j are linear. Furthermore, the auxiliary polynomials $R_m(n, \zeta)$ take on a value of either 1 or ζ, and therefore the basis functions become quite simple. In three dimensions,

$$\begin{aligned} \alpha_{1000} &= \alpha_1 = \zeta_1 \\ \alpha_{0100} &= \alpha_2 = \zeta_2 \\ \alpha_{0010} &= \alpha_3 = \zeta_3 \\ \alpha_{0001} &= \alpha_4 = \zeta_4. \end{aligned} \tag{3.20}$$

The utility of the barycentric coordinate formulation is also obvious when the equations in 3.20 are compared to the their Cartesian coordinate equivalents in equation 3.16.

It is illuminating to derive the equations in 3.20 using a different method. The derivation begins with the assumption that the solution is linear over the tetrahedra, and that the nodes are located only on the vertices of each tetrahedron. A three-dimensional linear function is defined by

$$T(x, y, z) = Ax + By + Cz + D, \tag{3.21}$$

and the value of the function at node j is given by

$$T_j(x_j, y_j, z_j) = Ax_j + By_j + Cz_j + D. \tag{3.22}$$

Using j=1 and eliminating the constant D yields

$$T - T_1 = A(x - x_1) + B(y - y_1) + C(z - z_1). \tag{3.23}$$

Equation 3.23 can be used to find A, B, and C:

$$\begin{aligned}
T_2 - T_1 &= A(x_2 - x_1) + B(y_2 - y_1) + C(z_2 - z_1) \\
T_3 - T_1 &= A(x_3 - x_1) + B(y_3 - y_1) + C(z_3 - z_1) \\
T_4 - T_1 &= A(x_4 - x_1) + B(y_4 - y_1) + C(z_4 - z_1).
\end{aligned} \tag{3.24}$$

Solving equation 3.24 for A, B, and C, results in

$$\begin{pmatrix} A \\ B \\ C \end{pmatrix} = \begin{pmatrix} x_2 - x_1 & y_2 - y_1 & z_2 - z_1 \\ x_3 - x_1 & y_3 - y_1 & z_3 - z_1 \\ x_4 - x_1 & y_4 - y_1 & z_4 - z_1 \end{pmatrix}^{-1} \begin{pmatrix} T_2 - T_1 \\ T_3 - T_1 \\ T_4 - T_1 \end{pmatrix}. \tag{3.25}$$

From equation 3.23, it is evident that $T - T_1$ is a linear combination of A, B, and C, and from equation 3.25, it is evident that A, B, and C are linear combinations of $T_j - T_1$ (where $j = 2, 3, 4$). Therefore, $T - T_1$ must be some linear combination of $T_j - T_1$ as well:

$$T - T_1 = \zeta_2(T_2 - T_1) + \zeta_3(T_3 - T_1) + \zeta_4(T_4 - T_1), \tag{3.26}$$

which can be rewritten as

$$\begin{aligned} T &= \zeta_2(T_2 - T_1) + \zeta_3(T_3 - T_1) + \zeta_4(T_4 - T_1) + T_1 \\ &= (1 - \zeta_2 - \zeta_3 - \zeta_4)T_1 + \zeta_2 T_2 + \zeta_3 T_3 + \zeta_4 T_4 \\ &= \zeta_1 T_1 + \zeta_2 T_2 + \zeta_3 T_3 + \zeta_4 T_4. \end{aligned} \tag{3.27}$$

Rewriting equation 3.26 as a matrix equation and substituting equation 3.24 returns

$$\begin{aligned} T - T_1 &= \begin{pmatrix} \zeta_2 & \zeta_3 & \zeta_2 \end{pmatrix} \begin{pmatrix} T_2 - T_1 \\ T_3 - T_1 \\ T_4 - T_1 \end{pmatrix} \\ &= \begin{pmatrix} \zeta_2 & \zeta_3 & \zeta_2 \end{pmatrix} \begin{pmatrix} x_2 - x_1 & y_2 - y_1 & z_2 - z_1 \\ x_3 - x_1 & y_3 - y_1 & z_3 - z_1 \\ x_4 - x_1 & y_4 - y_1 & z_4 - z_1 \end{pmatrix} \begin{pmatrix} A \\ B \\ C \end{pmatrix}. \end{aligned} \tag{3.28}$$

However, from equation 3.23, $T - T_1$ is also given as

$$T - T_1 = \begin{pmatrix} x - x_1 & y - y_1 & z - z_1 \end{pmatrix} \begin{pmatrix} A \\ B \\ C \end{pmatrix}. \tag{3.29}$$

Equating 3.28 and 3.29 cancels A, B, and C, and once again provides the formula used to convert between Cartesian and barycentric coordinates, albeit in a slightly different format:

$$\begin{pmatrix} x - x_1 \\ y - y_1 \\ z - z_1 \end{pmatrix} = \begin{pmatrix} x_2 - x_1 & y_2 - y_1 & z_2 - z_1 \\ x_3 - x_1 & y_3 - y_1 & z_3 - z_1 \\ x_4 - x_1 & y_4 - y_1 & z_4 - z_1 \end{pmatrix} \begin{pmatrix} \zeta_2 \\ \zeta_3 \\ \zeta_4 \end{pmatrix} \tag{3.30}$$

where it is understood that $\zeta_1 = 1 - \zeta_2 - \zeta_3 - \zeta_4$.

The continuity of the solution $u(x, y, z)$ across element boundaries is enforced when simplex elements are used. The argument is easiest to elucidate in two dimensions, where the simplex element is a triangle. A general solution $u(x, y)$ to a two-dimensional differential equation is expanded in the finite element formulation as

$$u(x, y) = \sum_{j=1}^{N} u_j \alpha_j(x, y),$$

and it is understood that the basis function α_j of degree N achieves a value of unity at node j and zero at every other node. If the function $u(x, y)$ is is a polynomial in x and y, $u = u(s)$ along a straight line s drawn anywhere through the triangular element is a polynomial of up to degree N. That straight line may be taken to be one of the element edges, and the polynomial along that edge is determined by the value of the function at the $N + 1$ nodes distributed on the element. This element edge is shared with an adjacent element. The polynomial along the edge of that adjacent element is determined by the *same* $N + 1$ nodes, and therefore the solution must be continuous across the element boundary formed by the shared edge.

The basis functions derived thus far are valid only for a single element. An N-dimensional solution domain may be subdivided into T simplex elements. Over each element τ, the solution u is represented by

$$u^{(\tau)} = \sum_{j=1}^{n} u_j \alpha_j, \tag{3.31}$$

where n is again the number of nodes assigned to a single element. Thus, the solution over the entire region Ω is obtained by summing the approximate solutions for each element:

$$u^{(\Omega)} = \sum_{\tau=1}^{T} u^{(\tau)}. \tag{3.32}$$

For the sake of clarity, a global node numbering system may be introduced, such that the familiar expansion,

$$u = \sum_{j=1}^{N} u_j \alpha_j, \tag{3.33}$$

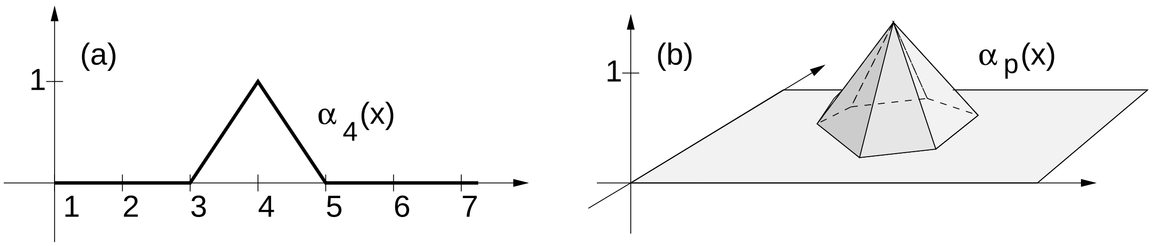

Fig. 3.3. The "tent" functions in (a) one dimension, and (b) two dimensions.

is valid. The basis function is again required to equal one at node j, and vanish at all other nodes. However, a number of elements may share the globally numbered node j, so that the definition must be altered slightly:

$$\bar{\alpha}_j = \sum_m \alpha_{j_{local}}^{(m)} \qquad m = \text{all elements containing node } j, \tag{3.34}$$

where j_{local} is the local node number of global node j, according, for example, to figure 3.2(b). In reality, the sum may be performed over all elements T. However, only the elements containing node j will have a non-zero contribution to the sum.

The modified basis functions $\bar{\alpha_j}$ are the so-called "tent functions", a well-deserved moniker arising from the distinctive shape of the functions in one and two dimensions (figure 3.3). A global node numbering system will always be used in this dissertation. Thus, the overbar will be dropped, and all subsequent references to the basis function α_j indicate the modified basis function $\bar{\alpha_j}$.

Mesh Generation

In one dimension, mesh generation is simply a matter of dividing the line segment representative of the solution domain into smaller line segments. The line segment is the only element available. Nodes may be spaced in order to take advantage of known properties of the solution. For example, a 1D EM algorithm may take advantage of the fact that variations in the field far from the source have a large wavelength. Consequently, the nodes may be spaced logarithmically or geometrically, so that nodes spacing increases with distance from the source.

In two and three dimensions, mesh generation quickly mushrooms in complexity. Once the appropriate element shape has been chosen from the myriad of available options, a mesh must be assembled that conforms to the boundaries and boundary conditions of the model. Entire texts have been devoted to the subject of mesh generation in two and three dimensions, including Ivanenko and Garanzha (2002), Edelsbrunner (2000), and Canann, et. al (2000).

A rectilinear mesh is used for the three dimensional finite element analysis presented in this dissertation. Such a mesh is ideally suited for modeling whole- and halfspaces, layers and rectangular prisms. These prisms may be represent buried inhomogeneities in the Earth, or may be used to model topographic features on the surface (i.e. horsts, grabens, or scarps).

Mesh generation begins with the specification of the minima and maxima of the solution domain in the x, y, and z directions. The number of nodes required for each axis are specified and evenly spaced along that axis. The even spacing is simply a matter of convenience; the nodes could be space logarithmically, geometrically, or even arbitrarily. The prisms defined by the nodes are each divided into six tetrahedra (Liu and Joe, 1996) such that the tetrahedra faces do not overlap other tetrahedra faces within the prism, and in adjacent prisms. The process is illustrated in figure 3.4. The quality of the mesh is quantified by the quality factor Q defined by

$$Q = 12(3V)^{2/3} \left\{ \sum_{i \neq j}^{4} L_{ij}^{2} \right\}^{-1} \tag{3.35}$$

(Liu and Joe, 1996), which relates the combined length of the tetrahedron edges to the tetrahedron volume. In equation 3.35, V is the tetrahedron volume and L_{ij} is the length of the edge connecting vertices i and j. The quality factor is defined such that regular well-shaped tetrahedra have Q values at or near 1.0, and poorly shaped or long, thin tetrahedra have Q values near zero. Acceptable tetrahedra typically have Q values ranging from 0.6

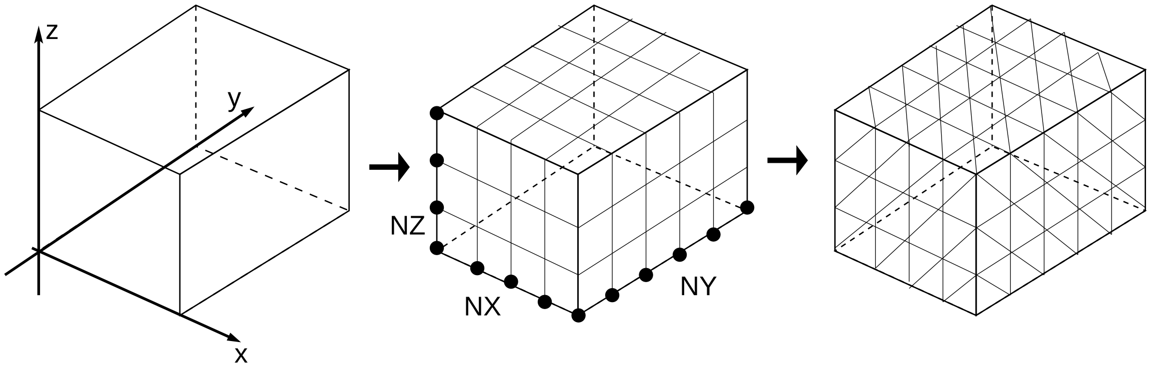

Fig. 3.4. 3D rectangular mesh generation.

to 1.0 (Badea et al., 2001).

Local Mesh Refinement

Oftentimes, greater resolution is required in the solution domain, particularly in regions sharp contrasts in conductivity (i.e. the interface between a buried metal object and the host medium), or where the surface of the conductor is complex. A number of different algorithms are available for local refinement of a finite element mesh, include algorithms by Liu and Joe (1996), and Travis and Chave (1989). The Liu and Joe algorithm is used in this research.

A region of the solution domain is first selected for local refinement after the initial discretization has been performed. Each tetrahedron in the local refinement region is marked, and new nodes, or split points, are added at the midpoint of each tetrahedron edge. The $\texttt{SUB}_8$ refinement scheme is used to subdivide each marked tetrahedron into eight subtetrahedra, as shown in figure 3.5(a). However, once the mesh is refined, overlapping faces exist at the boundary of the refinement region. The $\texttt{SUB}_8$ scheme adds one additional node at the centerpoint of each tetrahedron edge shared with the refined tetrahedra, and three additional nodes on each face shared with a refined tetrahedron. To ensure mesh continuity these “green” tetrahedra must also be refined. The $\texttt{SUB}_2$ and $\texttt{SUB}_4$ schemes are used to refine green tetrahedra that have inherited one and three nodes, respectively. Figure 3.6(a) provides an example of a locally refined mesh.

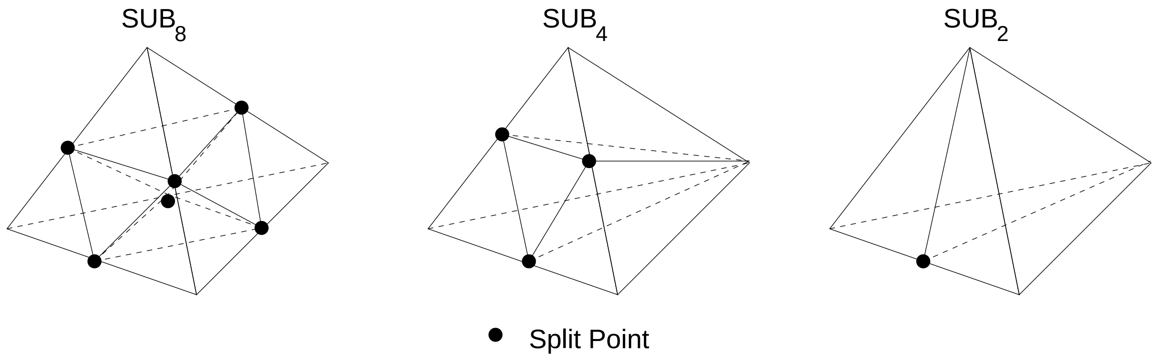

Fig. 3.5. Subdivision of tetrahedra.

Several local mesh refinements may be present within one finite element mesh. Finer resolution may, in fact, be achieved by nesting one or more local refinements. A mesh containing three nested refinements is displayed in figure 3.6(b). Caution must be taken to prevent the formation of poor quality or overlapping tetrahedra, but this quality control is easily automated.

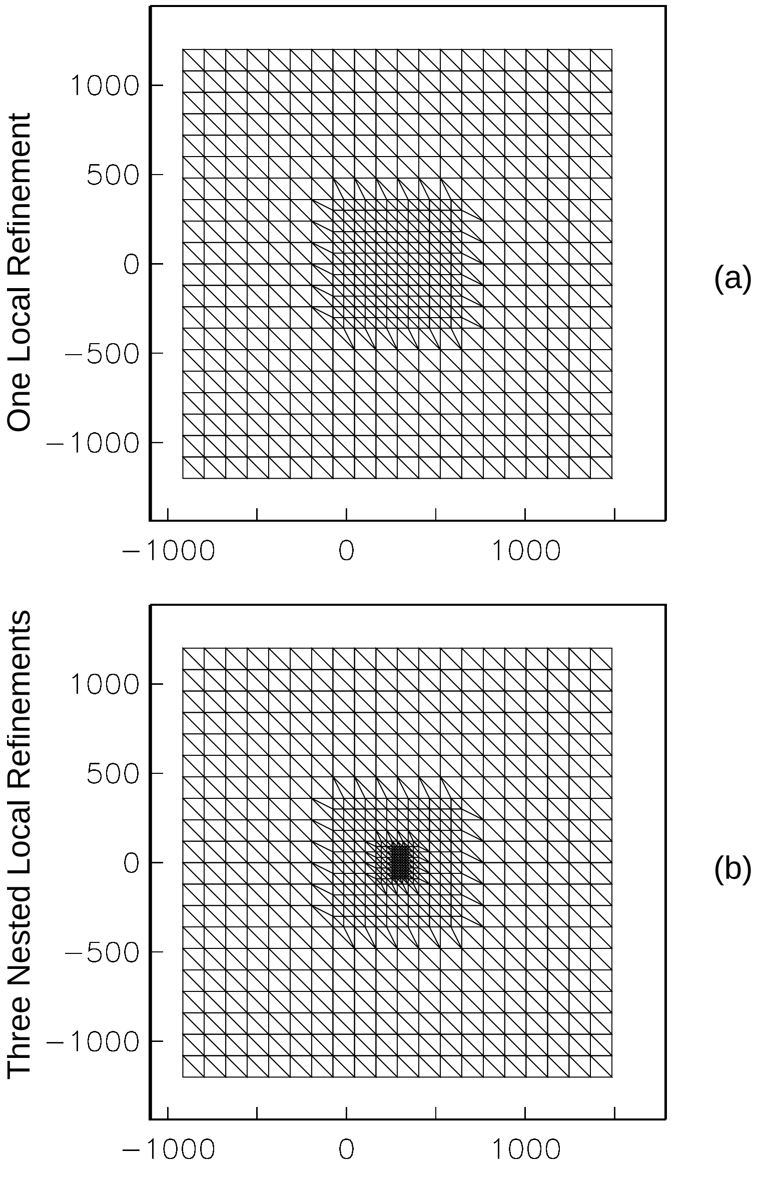

Fig. 3.6. Horizontal projection of a locally refined 3D finite element mesh. (a) A FE mesh with a single locally refined region. (b) The same FE mesh with three nested refinements.

CHAPTER IV

VALIDATION OF METHOD: “TOY” PROBLEMS

The Galerkin finite element method will be used to solve the $(\mathbf{A}, \Psi)$ coupled-potential formulation of Maxwell’s equations for a fully three-dimensional conductivity distribution. That is, the response of a CSEM experiment conducted over an earth containing arbitrarily shaped bodies of different conductivities will be calculated. However, in order to ensure the accuracy of the solution and the proper operation of the computer code designed to perform the calculations, the validity of the solution of much simpler “toy” problems is first evaluated. After the solution of a “toy” problem is verified against analytic or previously published results, the complexity of the “toy” problem is advanced, and the solution is again verified.

One Dimensional “Toy” Problems

A simple one-dimensional partial differential equation (PDE) is considered:

$$\frac{d^2u(x)}{dx^2} + \tau^2 u(x) = 0 \tag{4.1}$$

$$u(0) = g_0 \tag{4.2}$$

$$u(L_1) = g_1, \tag{4.3}$$

where $\tau^2 = \alpha + i\beta$. The analytic solution $u(x)$ is given by

$$u(x) = \frac{g_0[e^{-i\tau(2L_1-x)} - e^{-i\tau x}] + g_1[e^{-i\tau(L_1+x)} - e^{-i\tau(L_1-x)}]}{e^{-2i\tau L_1} - 1}. \tag{4.4}$$

The problem is one-dimensional, and the simplest possible element of a one-dimensional solution domain L is a line segment. Of course, in one-dimension, a line segment is the only possible element. This is the one-dimensional simplex element, containing $N+1$ “vertices”, where N is the dimensionality of the problem. Following the logic presented in the previous chapter, the nodes will be coincident with the vertices of the line segment, causing the basis functions α_j to be linear.

The solution u may be approximated by the expansion

$$u(x) = \sum_{j=1}^{N} u_j \alpha_j(x). \tag{4.5}$$

However, node 1 and node N are located at the boundaries of the solution domain L, and the value of the solution at these boundary nodes is given in equation 4.3. Therefore, the expansion can be rewritten as

$$u(x) = \sum_{j=2}^{N-1} a_j \alpha_j(x) + \sum_{k=1,N} b_k \alpha_k(x) \tag{4.6}$$

where the coefficient a_j is the value of the solution at internal node j, and b_k is the given value of the solution at boundary node k, so that $b_1 = g_0$ and $b_N = g_1$.

The expansion is substituted into the original differential equation (4.3):

$$\frac{d^2}{dx^2}\left[\sum_{j=2}^{N-1} a_j \alpha_j + \sum_{k=1,N} b_k \alpha_k\right] + \tau^2 \left[\sum_{j=2}^{N-1} a_j \alpha_j + \sum_{k=1,N} b_k \alpha_k\right] = 0. \tag{4.7}$$

The known boundary terms b_k are moved to the RHS of the equation, yielding

$$\sum_{j=2}^{N-1} a_j \left(\frac{d^2\alpha_j}{dx^2} + \tau^2 \alpha_j\right) = -\sum_{k=1,N} b_k \left(\frac{d^2\alpha_k}{dx^2} + \tau^2 \alpha_k\right). \tag{4.8}$$

The approximate weak formulation of this equation is obtained by multiplying equation 4.6 by the test function β_i (where $i = 1, \ldots, M$), and integrating over the solution domain L:

$$\int_{L_0}^{L_1} \beta_i \left[\sum_{j=2}^{N-1} a_j \left(\frac{d^2\alpha_j}{dx^2} + \tau^2 \alpha_j\right)\right] = -\int_{L_0}^{L_1} \beta_i \left[\sum_{k=1,N} b_k \left(\frac{d^2\alpha_k}{dx^2} + \tau^2 \alpha_k\right)\right]. \tag{4.9}$$

This is a system of M equations in $N-2$ unknowns. The coefficients a_j and b_k are constant, and may be moved outside of both the derivative and the integral. Furthermore, the order of differentiation may be reduced by integrating the equation above by parts, yielding

$$\begin{gathered}\sum_{j=2}^{N-1} a_j \left\{ \beta_i \left. \frac{d\alpha_j}{dx} \right|_{L_0}^{L_1} - \int_{L_0}^{L_1} \frac{d\alpha_j}{dx}\frac{d\beta_i}{dx} + \tau^2 \alpha_j \beta_i \; dx \right\} = \\ - \sum_{k=1,N} b_k \left\{ \beta_i \left. \frac{d\alpha_k}{dx} \right|_{L_0}^{L_1} - \int_{L_0}^{L_1} \frac{d\alpha_k}{dx}\frac{d\beta_i}{dx} + \tau^2 \alpha_j \beta_i \; dx \right\}.\end{gathered} \tag{4.10}$$

The Galerkin method prescribes choosing the test functions β_i from the same space as the basis functions α_j. The simplest way to accomplish this is to allow $\beta_i = \alpha_i$ where $i = 2, \ldots, N-1$. The Galerkin formulation has the added bonus of causing the $M \times N - 2$ system of equations to become well-determined; it now consists of $N - 2$ equations in $N - 2$ unknowns. Moreover, because $i = 2, \ldots, N-1$, α_i will always vanish at the "mesh" boundaries, allowing the boundary terms in equation 4.10 to vanish, yielding

$$\sum_{j=2}^{N-1} a_j \left[-\left(\frac{d\alpha_i}{dx}, \frac{d\alpha_j}{dx} \right)_L + \tau^2 (\alpha_i, \alpha_j)_L \right] = -\sum_{k=1,N} b_k \left[-\left(\frac{d\alpha_i}{dx}, \frac{d\alpha_k}{dx} \right)_L + \tau^2 (\alpha_i, \alpha_k)_L \right], \tag{4.11}$$

where

$$(a, b)_L = \int_{L_0}^{L_1} ab \; dx.$$

The known terms in this equation may be consolidated in the interest of simplicity, where

$$\mathcal{T}_{ij} = \int_{L_0}^{L_1} \frac{d\alpha_i}{dx}\frac{d\alpha_j}{dx} \; dx \tag{4.12}$$

and

$$\mathcal{R}_{ij} = \int_{L_0}^{L_1} \alpha_i \alpha_j \; dx. \tag{4.13}$$

Thus, equation 4.11 may be rewritten as

$$\sum_{j=2}^{N-1} a_j [\mathcal{T}_{ij} + \tau^2 \mathcal{R}_{ij}] = -\sum_{k=1,N} b_k [\mathcal{T}_{ik} + \tau^2 \mathcal{R}_{ik}]. \tag{4.14}$$

Recalling that the basis functions α_j are equal to one at node j, and zero at all other nodes, it is evident that $\mathcal{T}_{ij}$ is only nonzero if i is equal to j, or if nodes i and j are members of the same element. Thus, the system of equations becomes very sparse. This sparsity is advantageous because many computer algorithms exist that exploit such sparsity to increase the efficiency with which the solution to a system of equations is discovered.

This simple system of equations was solved rapidly using the drop-in lower and upper (LU) decomposition and back-substitution subroutines `LUDCMP` and `LUBKSB` taken from *Numerical Recipes in FORTRAN* (Press et al., 1992). A more efficient solver could have been implemented, but the advantage of using such a solver would be negligible for this simple test case. The finite element approximation is compared to the analytical solution in figure 4.1(a), where $L_0 = 0$, $L_1 = 1$, $\alpha = 1$, and $\beta = 2$. The finite element solution error, defined simply as

$$\mathrm{err}(x) = u^{\mathrm{analytic}}(x) - u^{\mathrm{FEM}}(x), \tag{4.15}$$

is displayed in figure 4.1(b). The finite element approximation of $u(x)$ is in excellent agreement with the analytic solution.

Equation 4.3 is made inhomogeneous if the right hand side is replaced with the non-zero term $f(x)$:

$$\frac{d^2u(x)}{dx^2} + \tau^2 u(x) = f(x) \tag{4.16}$$

$$u(L_0) = g_0 \tag{4.17}$$

$$u(L_1) = g_1. \tag{4.18}$$

The right hand side may be manufactured by specifying an arbitrary solution $u(x)$. If

$$u(x) = e^{i\frac{\alpha}{\beta}x}, \tag{4.19}$$

then the RHS becomes

$$f(x) = \left[\alpha + i\beta - \frac{\alpha^2}{\beta^2}\right] e^{i\frac{\alpha}{\beta}x}.$$

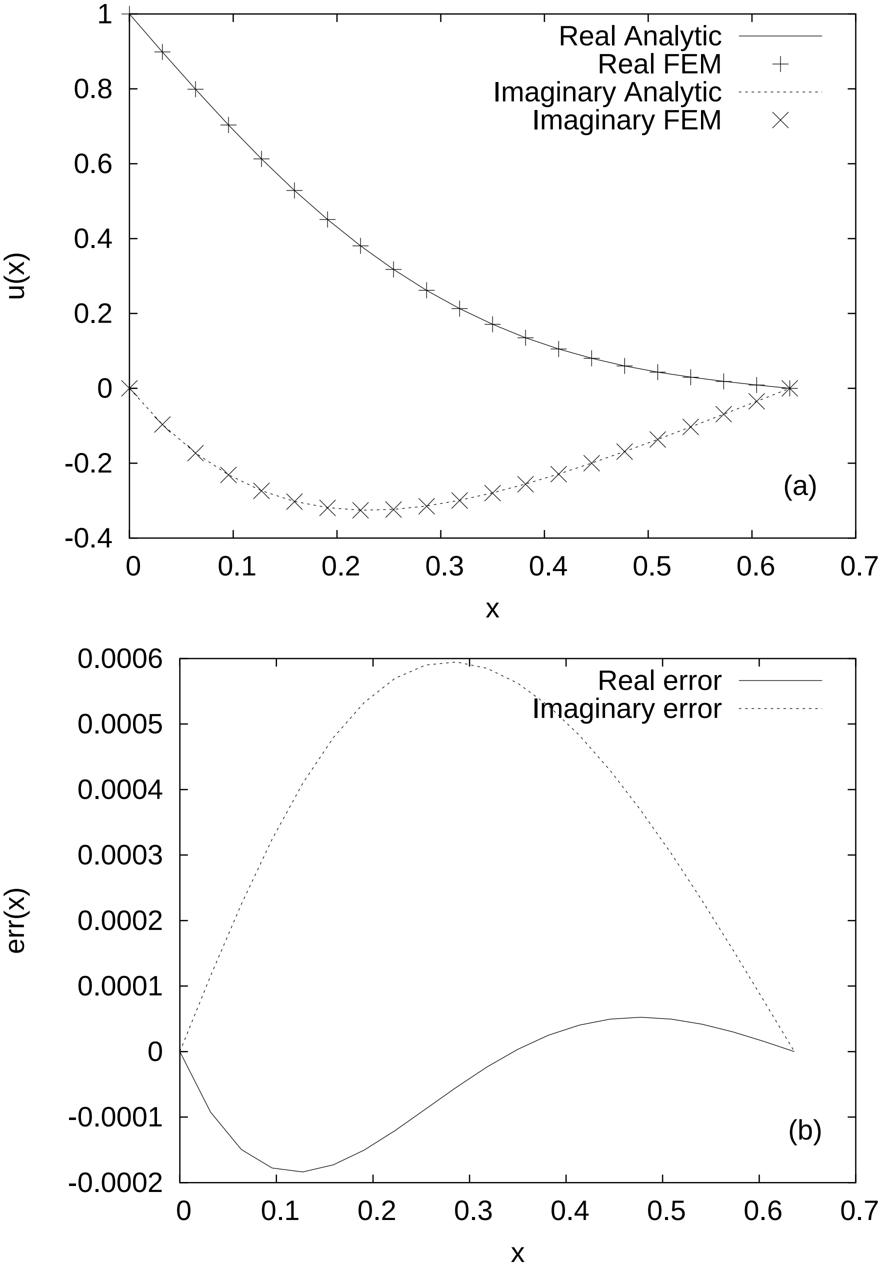

Fig. 4.1. The finite element solution of a complex one-dimensional “toy” problem (a) and the error incurred (b). The calculated finite element solution is displayed as symbols, and the analytic solution is displayed as a line. The error is calculated according to equation 4.15.

The equation is expanded and Galerkin's method is applied as before, recognizing that the RHS must also be multiplied by each test function α_i and integrated over L:

$$\sum_{j=2}^{N-1} a_j[\mathcal{T}_{ij} + \tau^2\mathcal{R}_{ij}] = (f, \alpha_i)_L - \sum_{k=1,N} b_k[\mathcal{T}_{ik} + \tau^2\mathcal{R}_{ik}]. \tag{4.20}$$

The integral $(f, \alpha_i)_L$ is comprised of known terms, and may be calculated using several different approaches. (1) The integral may be calculated numerically using a method such as Gaussian quadrature. (2) If f is assumed constant over each element, it may be brought outside the integral. (3) The function f may be expanded in the same manner as the solution u, so that $(f, \alpha_i) \to \sum_\ell f_\ell(\alpha_\ell, \alpha_i)_L$.

Method (2) will be used to calculate $(f, \alpha_i)_L$ in equation 4.20. Because $\alpha_i(x)$ vanishes at all nodes except i, the integral need only be calculated from node $i-1$ to node $i+1$:

$$(f, \alpha_i)_L = f_{i-\frac{1}{2}} \int_{i-1}^{i} \alpha_i(x)\ dx + f_{i+\frac{1}{2}} \int_{i}^{i+1} \alpha_i(x)\ dx, \tag{4.21}$$

where $f_{i-\frac{1}{2}}$ and $f_{i+\frac{1}{2}}$ are the values of $f(x)$ at the center of the elements to the left and right of node i, respectively.

The finite element approximation of the solution (figure 4.2(a)) agrees well with the analytic solution, equation 4.19, where $\alpha = 1$ and $\beta = 2$.

Three Dimensional "Toy" Problems

The validity of the basic tenets of the finite element algorithm have been demonstrated in one dimension. The concepts and methods developed in the previous chapter may therefore be built upon in order to develop a three dimensional finite element algorithm. The accuracy of this algorithm is similarly demonstrated using simple "toy" differential equations with known analytic solutions. Finally, the full three dimensional electromagnetic algorithm is constructed and compared to published 3D electromagnetic model responses.

1D "toy" problems on a 3D mesh— As a first order check of the three dimensional code, including the mesh generator, several one dimensional test equations are solved. The

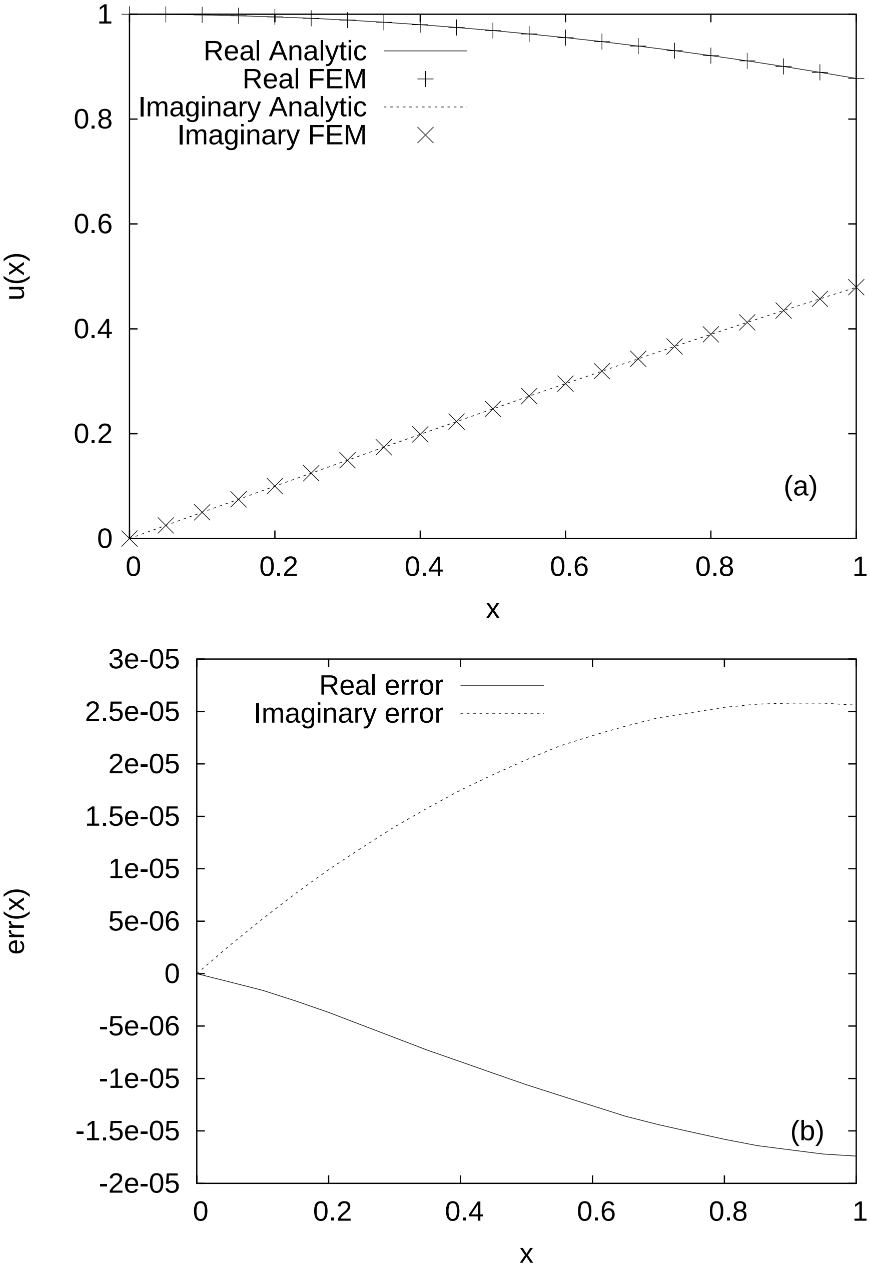

Fig. 4.2. The finite element solution of an inhomogeneous complex one-dimensional “toy” problem (a) and the error incurred (b). The calculated finite element solution is displayed with symbols, and the analytic solution is displayed as a line.

1D complex inhomogeneous equation from the previous chapter is recalled:

$$\frac{d^2u(x)}{dx^2} + \tau^2 u(x) = f(x). \tag{4.22}$$

The solution $u(x)$ is again expanded in the finite element basis functions. Because the mesh is three dimensional, the basis functions are also three dimensional, such that

$$u(x) = \sum_{j=1}^{N} u_j \alpha_j(x, y, z). \tag{4.23}$$

The expansion is separated in a known (boundary) portion, and an unknown (interior) portion, and is substituted into the original equation. Both the Galerkin method and integrating by parts are applied:

$$\sum_j a_j[\mathcal{T}_{ij} + \tau^2 \mathcal{R}_{ij}] = (f, \alpha_i)_\Omega - \sum_k b_k[\mathcal{T}_{ik} + \tau^2 \mathcal{R}_{ik}], \qquad (j \in \text{interior nodes})$$

$$(k \in \text{boundary nodes}) \tag{4.24}$$

where the boundary values are specified at all mesh boundaries, rather than simply at $z = L_0$ and $z = L_1$. For this simple test case, it is sufficient to use the known analytic solution to generate boundary values "on the fly".

The terms $\mathcal{T}_{ij}$ and $\mathcal{R}_{ij}$ must be modified for three dimensions as well:

$$\mathcal{T}_{ij} = \int_\Omega \frac{\partial \alpha_i(x, y, z)}{\partial x} \frac{\partial \alpha_j(x, y, z)}{\partial x}\, d\Omega \tag{4.25}$$

$$\mathcal{R}_{ij} = \int_\Omega \alpha_i(x, y, z) \alpha_j(x, y, z)\, d\Omega, \tag{4.26}$$

where Ω is the 3D solution domain. Because the differential equation is one dimensional, the derivatives must become partial derivatives. In 1D, calculation of these integrals is simple and straight forward. In 3D, the integrals also reduce to simple operations with a bit of manipulation.

The integral is greatly simplified if the definition of the modified basis function (equation 3.34) is inserted into equations 4.25 and 4.26:

$$\mathcal{T}_{ij} = \sum_{\tau} \int_{\Omega_\tau} \frac{\partial \alpha^{(\tau)}_{i_{local}}}{\partial x} \frac{\partial \alpha^{(\tau)}_{j_{local}}}{\partial x} \; d\Omega_\tau \tag{4.27}$$

$$\mathcal{R}_{ij} = \sum_{\tau} \int_{\Omega_\tau} \alpha^{(\tau)}_{i_{local}} \alpha^{(\tau)}_{j_{local}} \; d\Omega_\tau, \tag{4.28}$$

where τ indicates all tetrahedra shared by nodes i and j. The definition of $\alpha^{\tau}_{i_local}$ is considered:

$$\alpha_i^{(\tau)} = \frac{\begin{vmatrix} 1 & x & y & z \\ 1 & x_j & y_j & z_j \\ 1 & x_k & y_k & z_k \\ 1 & x_l & y_l & z_l \end{vmatrix}}{\begin{vmatrix} 1 & x_i & y_i & z_i \\ 1 & x_j & y_j & z_j \\ 1 & x_k & y_k & z_k \\ 1 & x_l & y_l & z_l \end{vmatrix}}, \tag{4.29}$$

where i,j,k, and l are the locally numbered nodes of the tetrahedron τ. Expanding the numerator, and allowing the denominator to equal Γ,

$$\alpha_i^{(\tau)} = \frac{1}{\Gamma} \left[\begin{vmatrix} x_j & y_j & z_j \\ x_k & y_k & z_k \\ x_l & y_l & z_l \end{vmatrix} - x \begin{vmatrix} 1 & x_j & z_j \\ 1 & x_k & z_k \\ 1 & x_l & z_l \end{vmatrix} + y \begin{vmatrix} 1 & x_j & z_j \\ 1 & x_k & z_k \\ 1 & x_l & z_l \end{vmatrix} - z \begin{vmatrix} 1 & x_j & y_j \\ 1 & x_k & y_k \\ 1 & x_l & y_l \end{vmatrix} \right], \tag{4.30}$$

reveals that any spatial derivative of α_i will be a constant. For example,

$$\frac{\partial \alpha_i}{\partial x} = -\frac{1}{\Gamma} \begin{vmatrix} 1 & y_j & z_j \\ 1 & y_k & z_k \\ 1 & y_l & z_l \end{vmatrix}. \tag{4.31}$$

Thus $\mathcal{T}_{ij}$ simply becomes

$$\mathcal{T}_{ij} = \sum_{\tau} \frac{\partial \alpha_i^{(\tau)}}{\partial x} \frac{\partial \alpha_j^{(\tau)}}{\partial x} V_\tau, \tag{4.32}$$

where V_τ is the volume of tetrahedron τ.

The quantity $\mathcal{R}_{ij}$ may be evaluated using formulae presented by Eisenburg and Malvern (1973). These equations, originally derived empirically, describe integration in barycentric coordinates for various element shapes. For a tetrahedron, the formula is

$$\int_V \zeta_1^a \zeta_2^b \zeta_3^c \zeta_4^d \; dV. = \frac{a!b!c!d!}{(a+b+c+d+3)!} 6V \tag{4.33}$$

The local basis function α_j is equal to ζ_j, so that the integral is quite simple. Thus equation 4.26 simplifies to

$$\mathcal{R}_{ij} = \begin{cases} \sum_\tau \frac{V_\tau}{20} & \text{if } i \neq j \\ \sum_\tau \frac{V_\tau}{10} & \text{if } i = j \end{cases} \tag{4.34}$$

The right hand side must also be adjusted for three dimensions. If it is assumed, as before, that f is constant over each element, then it can be moved outside the integral. Inserting the definition of the local basis function, the RHS becomes

$$\sum_\tau f_\tau \int_{\Omega_\tau} \alpha_{i_{local}}^{(\tau)} \; d\Omega, \tag{4.35}$$

which reduces to

$$\sum_\tau f_\tau \frac{V_\tau}{4} \tag{4.36}$$

using equation 4.33.

With all of the quantities specified, the finite element system of equations (4.24) may be assembled. This system of equations is solved using the subroutine `ILUSPARSE`, a robust, monotonically convergent subroutine designed to take advantage of the sparsity of the system of equations (Everett and Schultz, 1996). The results are displayed in figure 4.3 for $\alpha = 1$ and $\beta = 2$ for a solution domain Ω defined as $0 \leq x \leq 1$, $-1 \leq y \leq 1$, and

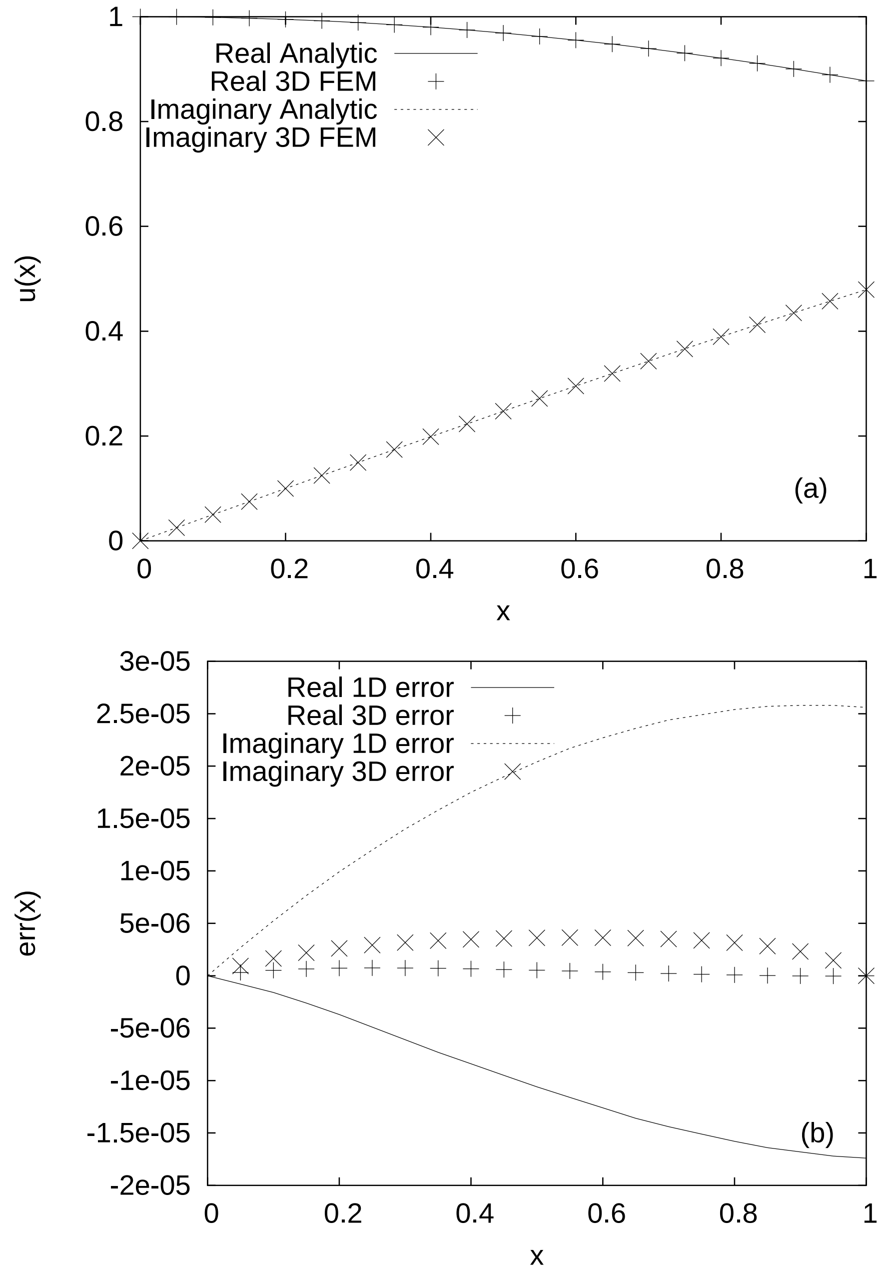

Fig. 4.3. A 1D “toy” problem solved on a 3D finite element mesh (a), and the error incurred (b). The calculated finite element solution is displayed with symbols, and the analytic solution is displayed as a line.

$-1 \leq z \leq 1$.

In anticipation of the coupled-vector nature of the $(\mathbf{A}, \Psi)$ CSEM model, a 1D coupled vector problem is considered:

$$\frac{d^2u(z)}{dz^2} - \tau^2 v(z) = f(z) \tag{4.37}$$

$$\frac{d^2v(z)}{dz^2} - \tau^2 u(z) = g(z), \tag{4.38}$$

where the functions u and v may represent, for example, the x and y components of a one dimensional vector, and are expanded as

$$u(z) = \sum_j a_j \alpha_j(x, y, z) + \sum_k b_k \alpha_k(x, y, z) \tag{4.39}$$

$$v(z) = \sum_j c_j \alpha_j(x, y, z) + \sum_k d_k \alpha_k(x, y, z). \tag{4.40}$$

By the usual method, equations 4.37 and 4.37 become

$$-\sum_j a_j \mathcal{T}_{ij} - \tau^2 c_j \mathcal{R}_{ij} = (f(z), \alpha_i) + \sum_k b_k \mathcal{T}_{ik} + \tau^2 d_k \mathcal{R}_{ik} = \mathcal{S}_i \tag{4.41}$$

and

$$-\sum_j c_j \mathcal{T}_{ij} - \tau^2 a_j \mathcal{R}_{ij} = (g(z), \alpha_i) + \sum_k d_k \mathcal{T}_{ik} + \tau^2 b_k \mathcal{R}_{ik} = \mathcal{U}_i \tag{4.42}$$

respectively.

Because the two systems of equations are coupled, both must be solved simultaneously.

Therefore, each location i, j in the finite element matrix is replaced with a 4×4 submatrix,

$$\begin{pmatrix} \begin{pmatrix} \mathcal{T}_{11} & \tau^2\mathcal{R}_{11} \\ \tau^2\mathcal{R}_{11} & \mathcal{T}_{11} \end{pmatrix} & \begin{pmatrix} \mathcal{T}_{12} & \tau^2\mathcal{R}_{12} \\ \tau^2\mathcal{R}_{12} & \mathcal{T}_{12} \end{pmatrix} & \cdots & \begin{pmatrix} \mathcal{T}_{1M} & \tau^2\mathcal{R}_{1M} \\ \tau^2\mathcal{R}_{1M} & \mathcal{T}_{1M} \end{pmatrix} \\ \begin{pmatrix} \mathcal{T}_{21} & \tau^2\mathcal{R}_{21} \\ \tau^2\mathcal{R}_{21} & \mathcal{T}_{21} \end{pmatrix} & \begin{pmatrix} \mathcal{T}_{22} & \tau^2\mathcal{R}_{22} \\ \tau^2\mathcal{R}_{22} & \mathcal{T}_{22} \end{pmatrix} & \cdots & \begin{pmatrix} \mathcal{T}_{2M} & \tau^2\mathcal{R}_{2M} \\ \tau^2\mathcal{R}_{2M} & \mathcal{T}_{2M} \end{pmatrix} \\ \vdots & \vdots & \ddots & \vdots \\ \begin{pmatrix} \mathcal{T}_{M1} & \tau^2\mathcal{R}_{M1} \\ \tau^2\mathcal{R}_{M1} & \mathcal{T}_{M1} \end{pmatrix} & \begin{pmatrix} \mathcal{T}_{M2} & \tau^2\mathcal{R}_{M2} \\ \tau^2\mathcal{R}_{M2} & \mathcal{T}_{M2} \end{pmatrix} & \cdots & \begin{pmatrix} \mathcal{T}_{MM} & \tau^2\mathcal{R}_{MM} \\ \tau^2\mathcal{R}_{MM} & \mathcal{T}_{MM} \end{pmatrix} \end{pmatrix} \begin{pmatrix} \begin{pmatrix} a_1 \\ c_1 \end{pmatrix} \\ \begin{pmatrix} a_2 \\ c_2 \end{pmatrix} \\ \vdots \\ \begin{pmatrix} a_M \\ c_M \end{pmatrix} \end{pmatrix}$$

$$= \begin{pmatrix} \begin{pmatrix} \mathcal{S}_1 \\ \mathcal{U}_1 \end{pmatrix} \\ \begin{pmatrix} \mathcal{S}_2 \\ \mathcal{U}_2 \end{pmatrix} \\ \vdots \\ \begin{pmatrix} \mathcal{S}_M \\ \mathcal{U}_M \end{pmatrix} \end{pmatrix},$$

where M is the number of free (interior) nodes in the mesh. Doubling the number of unknowns quadruples the size of the matrix that must be inverted, rapidly increasing the computer resources necessary to solve the finite element system of equations.

The solutions u and v are given as

$$u(z) = e^{i\tau z} \tag{4.43}$$

$$v(z) = e^{2i\tau z}, \tag{4.44}$$

and the right hand sides $f(z)$ and $g(z)$ are manufactured accordingly for $\tau = \sqrt{1+2i}$. The results are shown in figure 4.4 for a solution domain Ω where $-1 \leq x \leq 1$, $-1 \leq y \leq 1$, and $0 \leq z \leq 1$. The error incurred in the finite element approximation is shown in figure 4.5.

The three dimensional finite element method yields results comparable to, if not better than, the one dimensional results.

Three dimensional “toy” problems— A simple, but fully three dimensional scalar “toy” differential equation is given by

$$\nabla^2 u(x,y,z) - \tau^2 u(x,y,z) = f(x,y,z), \tag{4.45}$$

where, as before, $\tau^2 = \alpha + i\beta$. This equation has the arbitrarily assigned solution

$$u(x,y,z) = \sin(x\tau)\cos(y\tau)\exp(i\frac{\alpha}{\beta}z). \tag{4.46}$$

The solution is expanded and inserted into the original equation, which is multiplied by the basis function $\alpha_i(x,y,z)$:

$$\sum_j u_j[(\nabla^2\alpha_j,\alpha_i) - \tau^2(\alpha_j,\alpha_i)] = (f,\alpha_i) - \sum_k b_k[(\nabla^2\alpha_k,\alpha_i) - \tau^2(\alpha_k,\alpha_i)], \tag{4.47}$$

where j is one of the free nodes in the interior of the mesh, and k is one of the mesh boundary nodes. Green’s theorem (3D integration by parts) is applied to eliminate the second order derivatives:

$$\sum_j u_j[-(\nabla\alpha_j,\nabla\alpha_i) - \tau^2(\alpha_j,\alpha_i)] = (f,\alpha_i) - \sum_k b_k[-(\nabla\alpha_k,\nabla\alpha_i) - \tau^2(\alpha_k,\alpha_i)]. \tag{4.48}$$

Redefining $\mathcal{T}_{ij}$ and $\mathcal{R}_{ij}$ for three dimensions,

$$\mathcal{T}_{ij} = \int_\Omega \nabla\alpha_i\nabla\alpha_j \; d\Omega \qquad\qquad \mathcal{R}_{ij} = \int_\Omega \alpha_i\alpha_j \; d\Omega \tag{4.49}$$

equation 4.48 simplifies to

$$\sum_j u_j[-\mathcal{T}_{ij} - \tau^2\mathcal{R}_{ij}] = (f,\alpha_i) - \sum_k b_k[-\mathcal{T}_{ik} - \tau^2\mathcal{R}_{ik}], \tag{4.50}$$

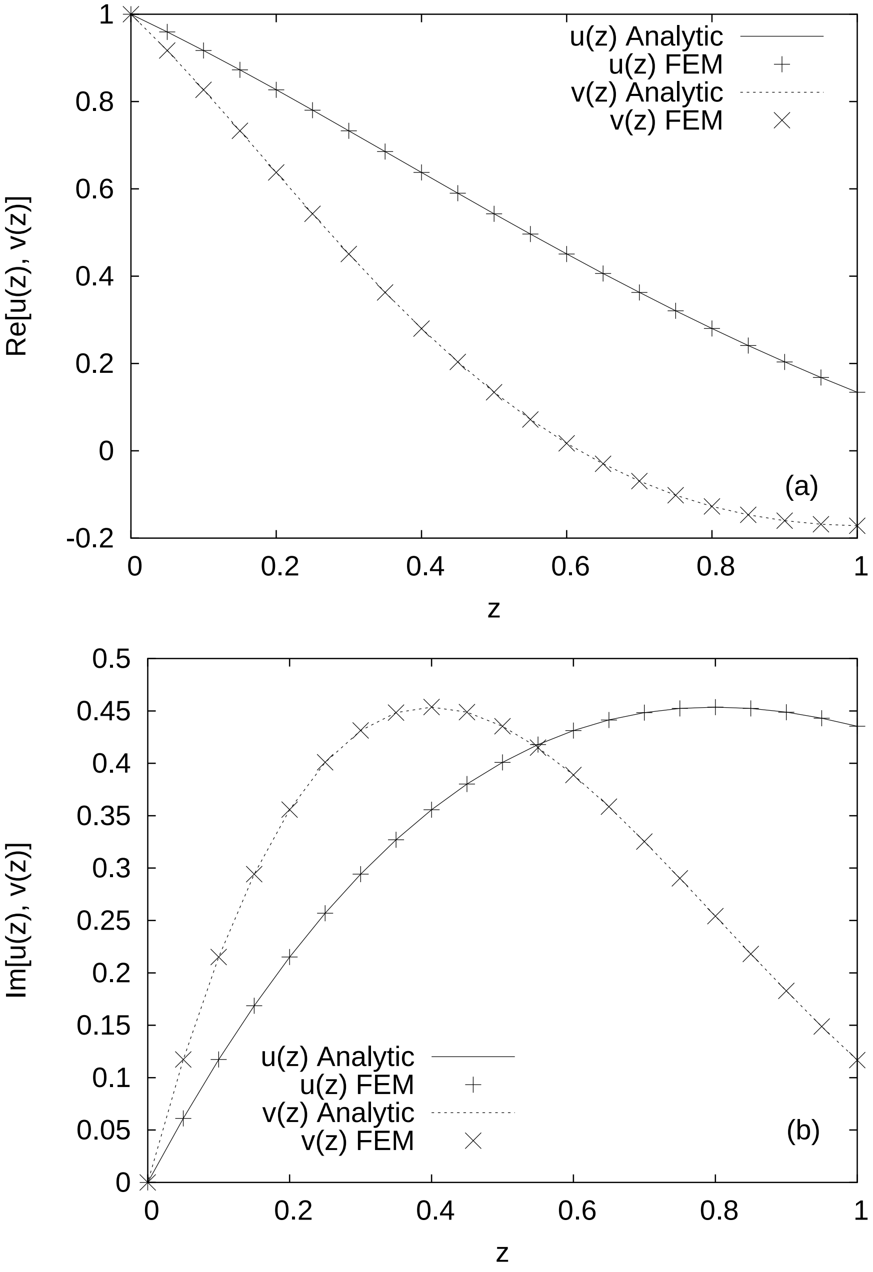

Fig. 4.4. The real (a) and imaginary (b) parts of a finite element approximation of the solutions to a pair of coupled vector differential equations. The calculated finite element solutions are shown with symbols, and the analytic solutions are shown as lines.

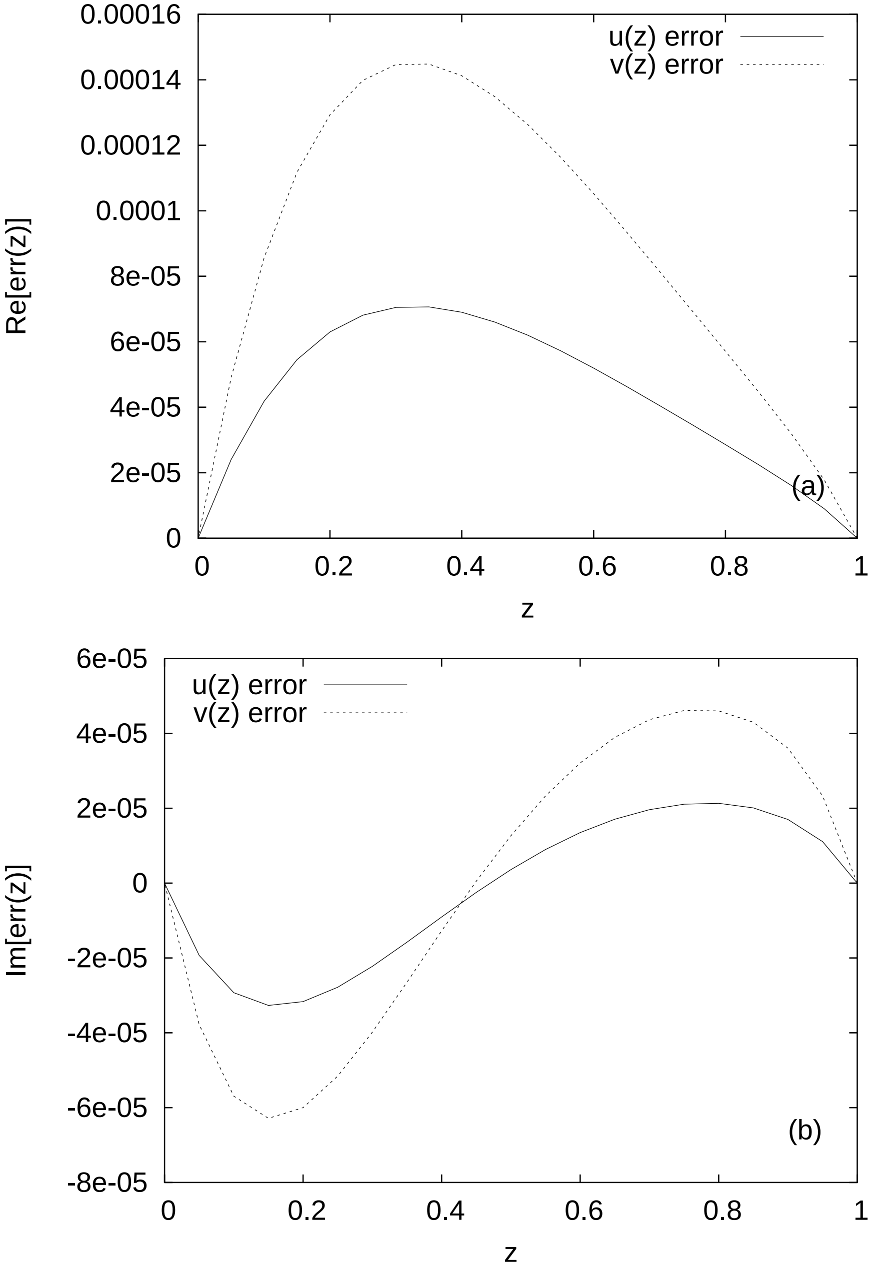

Fig. 4.5. The real (a) and imaginary (b) parts of a finite element approximation error in the solutions to a pair of coupled vector differential equations.

where $\mathcal{R}_{ij}$ is defined as in the previous section, and $\mathcal{T}_{ij}$ becomes

$$\mathcal{T}_{ij} = \sum_{\tau} \left] \frac{\partial \alpha_i^{(\tau)}}{\partial x} \frac{\partial \alpha_j^{(\tau)}}{\partial x} + \frac{\partial \alpha_i^{(\tau)}}{\partial y} \frac{\partial \alpha_j^{(\tau)}}{\partial y} + \frac{\partial \alpha_i^{(\tau)}}{\partial z} \frac{\partial \alpha_j^{(\tau)}}{\partial z} \right] V_{\tau}, \tag{4.51}$$

because, as above, the spatial derivatives of $\alpha_i^{(\tau)}(x, y, z)$ reduce to constants (see equation 4.30).

A profile in the z-direction of the finite element solution for $\alpha = 1$ and $\beta = 2$ at $x = y = 0.5$ is displayed in figure 4.6.

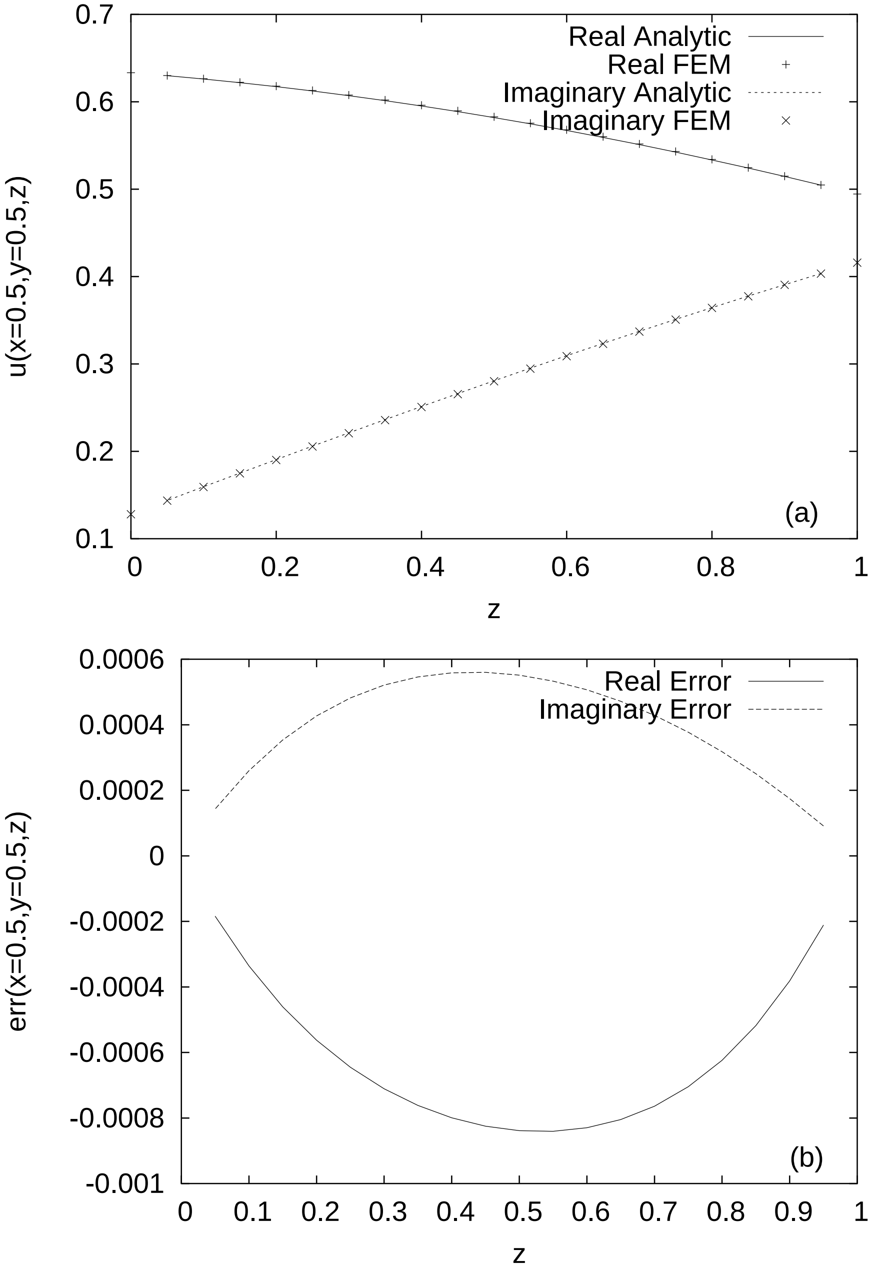

Fig. 4.6. A finite element solution of a simple “toy” 3D differential equation (a) and the error incurred (b). The finite element solution (symbols) is compared to the known analytic solution (lines).

CHAPTER V

VALIDATION OF METHOD: FREQUENCY DOMAIN CSEM MODELING

The finite element solution of the one and three dimensional “toy” differential equations presented thus far provide the basic framework from which one and three dimensional controlled-source electromagnetic modeling algorithms may be developed. Maxwell’s equations governing the CSEM response are simply differential equations that may be plugged into the previously developed 1D and 3D algorithms, provided the equations can be massaged into the correct form.

The method is first verified in one dimension against a semi-analytic 1D solution from Ward and Hohmann (1987). Subsequently, the fully three-dimensional finite element solution of Maxwell’s equations is presented in comparison with several models from Badea, et al. (2001) and Pridmore, et al. (1981).

One Dimensional EM Modeling

The one-dimensional finite element algorithm developed above may be expanded to model the frequency-domain response of a one-dimensional (i. e. layered) earth energized by an oscillating finite magnetic dipole loop source of radius a located at height h above the Earth’s surface.

The governing vector diffusion equation in a cylindrical coordinate system for the electric field in the frequency domain is

$$\nabla \times \nabla \times \mathbf{E}(\rho, z) + i\mu_0\omega\sigma(\mathbf{r})\mathbf{E}(\rho, z) = -i\mu_0\omega\mathbf{J}_P(\rho, z), \tag{5.1}$$

where an $e^{i\omega t}$ time dependence is implied. Because the source current is a magnetic dipole current loop, the use of a cylindrical coordinate system is indicated. Compliance with the principle of conservation of charge implies that the secondary current flow generated in the subsurface must flow in closed loops, such that

$$\mathbf{J}_S = J_{S\phi}(\rho, z)\hat{\phi}. \tag{5.2}$$

From Ohm's Law ($\mathbf{J} = \sigma\mathbf{E}$) then, the electric field must also follow suit:

$$\mathbf{E} = E_\phi(\rho, z)\hat{\phi}. \tag{5.3}$$

The conductivity of the model varies only in the z direction, so that

$$\sigma(\mathbf{r}) = \sigma(z). \tag{5.4}$$

The electric field and conductivity are divided into a known primary and an unknown secondary portion in order to avoid numerical difficulties associated with the singularity in the primary field at the center of the loop source:

$$\begin{gathered}\mathbf{E}(\rho, z) = \mathbf{E}_P(\rho, z) + \mathbf{E}_S(\rho, z) = E_\phi(\rho, z) = E_{\phi P}(\rho, z) + E_{\phi S}(\rho, z) \\ \sigma(z) = \sigma_P(z) + \sigma_S(z)\end{gathered} \tag{5.5}$$

These expressions are inserted into equation 5.1:

$$\nabla \times \nabla \times (E_P + E_S) + i\mu_0\omega(\sigma_P + \sigma_S)(E_P + E_S) = -i\mu_0\omega J_P. \tag{5.6}$$

Recalling that the primary field satisfies the equation

$$\nabla \times \nabla \times E_P + i\mu_0\omega\sigma_P E_P = -i\mu_0\omega J_P, \tag{5.7}$$

the primary terms may be eliminated from equation 5.6:

$$\nabla \times \nabla \times E_S + i\mu_0\omega\sigma E_S = -i\mu_0\omega\sigma_S E_P. \tag{5.8}$$

The 1D scalar diffusion equation is obtained by rewriting the curl-curl term using the definition of curl in cylindrical coordinates:

$$\frac{\partial}{\partial \rho}\left(\frac{1}{\rho}\frac{\partial}{\partial \rho}[\rho E_S]\right) + \frac{\partial^2 E_S}{\partial z^2} + \alpha(z)^2 E_S = i\mu_0\omega\sigma_S E_P, \tag{5.9}$$

where

$$\alpha(z) \equiv \sqrt{-i\mu_0\omega\sigma(z)} \tag{5.10}$$

is the characteristic wave number of each conducting layer.

A Hankel transform is defined as

$$E_S(\rho, z) = \int_0^\infty \bar{E}_S(\lambda, z) J_1(\lambda\rho)\lambda \; d\lambda, \tag{5.11}$$

where $J_1(\lambda\rho)$ is the Bessel function of the first kind of order 1, and is inserted into equation 5.9:

$$\begin{aligned}\int_0^\infty \lambda \; d\lambda \left\{ \bar{E}_S(\lambda, z)\frac{\partial}{\partial \rho}\left(\frac{1}{\rho}\frac{\partial}{\partial \rho}[\rho J_1(\lambda\rho)]\right) + \frac{\partial^2 \bar{E}_S(\lambda, z) J_1(\lambda\rho)}{\partial z^2} + \alpha^2 \bar{E}_S(\lambda, z) J_1(\lambda\rho)\right\} \\ = i\mu_0\omega\sigma_S(z)\int_0^\infty \bar{E}_P(\lambda, z) J_1(\lambda\rho)\lambda \; d\lambda. \end{aligned} \tag{5.12}$$

The first term in the left hand integral satisfies the Bessel equation

$$\frac{\partial}{\partial \rho}\left(\frac{1}{\rho}\frac{\partial}{\partial \rho}[\rho J_1(\lambda\rho)]\right) = -\lambda^2 J_1(\lambda\rho). \tag{5.13}$$

Inserting this expression into equation 5.12 and equating the integrands yields the governing ODE for the 1D EM response of a layered earth in the wavenumber domain:

$$\frac{d^2 \bar{E}_S(\lambda, z)}{dz^2} + \gamma(z)^2 \bar{E}_S(\lambda, z) = i\mu_0\omega\sigma_S(z)\bar{E}_P(\lambda, z) \tag{5.14}$$

where

$$\gamma(z)^2 = \alpha(z)^2 - \lambda^2. \tag{5.15}$$

Equation 5.14 is identical in form to equation 4.18, the 1D inhomogeneous “toy” problem, where $u(x) = \bar{E}_S(x)$, $\tau^2 = \gamma^2$, and $f(x) = i\mu_0\omega\sigma_S(z)E_P(z)$. Hence, finite element formulation will be achieved by the same method.

The secondary electric field E_S vanishes at infinity. Thus, the natural boundary conditions are

$$\begin{aligned} E_S(z = -\infty) &= 0 \\ E_S(z = \infty) &= 0. \end{aligned} \tag{5.16}$$

These boundary conditions are, of course, impractical for seeking a numerical solution to equation 5.14. It is acceptable practice to allow the electric field to vanish at 3 × δ, where δ is the skin depth of a conductor, given as

$$\delta = \sqrt{\frac{2}{\sigma\mu_0\omega}}, \tag{5.17}$$

and defined as the distance at which a planar electric field within a material of conductivity σ will decrease in magnitude by a factor of $1/e$. The skin depth is only an approximation, because the modeled source is a dipolar rather than planar. Additionally, because the modeled Earth is layered, an average conductivity is used to calculate the skin depth.

Although the electric field decays much more slowly in the air, it will suffice to allow the electric field to vanish in the air at several times the distance specified for the Earth. Alternatively, the air layer may be avoided altogether with the application of an impedance boundary condition at the Earth’s surface. The governing ODE in the air simplifies to

$$\frac{d^2\bar{E}_S}{dz^2} - \lambda^2 E_S = 0, \tag{5.18}$$

because $\sigma_P = \sigma_S = 0$. This equation has the general solution

$$\bar{E}_s = Ae^{\lambda z}, \tag{5.19}$$

so that

$$\frac{d\bar{E}_S}{dz} = \lambda A e^{\lambda z} = \lambda \bar{E}_S. \tag{5.20}$$

Therefore, the impedance boundary condition

$$\frac{d\bar{E}_S(\lambda, z=0)}{dz} - \lambda \bar{E}_S(\lambda, z=0) = 0 \tag{5.21}$$

can be applied at the Earth's surface.

Equation 5.14 is expanded and the Galerkin method is applied as before, with the exception that the subscripts i and j range from 1 to $N-1$ (rather than from 2 to $N-1$). In consequence, the surface term does not vanish when the resulting equation is integrated by parts:

$$\sum_{j=1}^{N-1} \bar{E}_{Sj} \left[\left(\alpha_i(z) \left. \frac{d\alpha_j(z)}{dz} \right|_0^{z_L} - \mathcal{T}_{ij} \right) + \gamma(z)^2 \mathcal{R}_{ij} \right] = i\mu_0 \omega \sigma_S (\bar{E}_P, \alpha_i). \tag{5.22}$$

The surface term is expanded as

$$\alpha_i(z) \left. \frac{d\alpha_j(z)}{dz} \right|_0^{z_L} = \alpha_i(z_L) \frac{d\alpha_j(z_L)}{dz} - \alpha_i(0) \frac{d\alpha_j(0)}{dz}, \tag{5.23}$$

which can be greatly simplified by recalling that the basis function α_j is equal to zero at all nodes except i. The terms on the right hand side then become

$$\alpha_i(0) = \begin{cases} 1 & i = 1 \\ 0 & i \neq 1 \end{cases} = \delta_{i1} \qquad\qquad \alpha_i(z_L) = 0 \text{ for all } i$$

$$\frac{d\alpha_j(0)}{dz} = \lambda \alpha_j(0) = \lambda \delta_{1j}, \tag{5.24}$$

where δ_{ij} is the Kroenecker delta function. The finite element formulation of the 1D electric field equation in the wavenumber domain thus becomes

$$\sum_{j=1}^{N-1} \bar{E}_{Sj} \left[-\lambda\delta_{i1}\delta_{1j} - \mathcal{T}_{ij} + \gamma^2\mathcal{R}_{ij}\right] = i\mu_0\omega\sigma_S(\bar{E}_P, \alpha_i), \tag{5.25}$$

if an impedance boundary condition is enforced at the Earth's surface.

The primary field $\bar{E}_P$ is the the electric field of a loop source of radius a, frequency ω, and current I in free space, which is described by

$$\bar{E}_P(\lambda, z) = \frac{-i\mu_0\omega I a J_1(\lambda a)}{2\lambda}\, e^{-\lambda|z+h|}, \tag{5.26}$$

where the Bessel function J_1 is calculated using the subroutine `BESSJ1` from *Numerical Recipes in FORTRAN* (Press et al., 1992). Refer to Ward and Hohmann (1987) for a derivation of this equation.

The finite element solution of equation 5.14 returns the value of $\bar{E}_S(\lambda, z)$ at each element node, for a specific wavenumber λ. The solution must be Hankel transformed back into the spatial domain via equation 5.11. The Hankel transform is performed numerically using the digital filter method of Guptasarma and Singh (1997). The digital filter is defined as

$$E_S(\rho, z) = \frac{1}{\rho}\sum_{i=1}^{N}(\bar{E}_S(\lambda_i, z)W_i) \tag{5.27}$$

where

$$\lambda_i = \frac{1}{\rho}10^{[s_1+(i-1)s_2]}. \tag{5.28}$$

The length of the filter N, the weights W_i, and the constants s_1 and s_2 depend upon the order of transform desired; these parameters are specified in Guptasarma and Singh (1997). Thus for each radial coordinate ρ at which the solution is desired, the finite element solution to equation 5.14 must be determined N times. For the 0th order Hankel transform, $N = 120$, and $N = 140$ for the 1st order transform.

In an actual CSEM survey, it is the magnetic field that is measured. If the receiver is a vertical magnetic dipole, only the z component of the magnetic field is measured. Faraday's Law in the frequency domain,

$$\nabla \times \mathbf{E}_S = -i\omega \mathbf{B}_S, \tag{5.29}$$

suggests that the magnetic field may be obtained from the electric field. It has been established that the electric field in cylindrical coordinates is a scalar. Accordingly, equation 5.29 may be rewritten as

$$\hat{\rho}\left(-\frac{\partial E_{S\phi}}{\partial z}\right) + \hat{z}\left(\frac{1}{\rho}\frac{\partial}{\partial \rho}(\rho E_{S\phi})\right) = -i\omega(B_{S\rho}\hat{\rho} + B_{Sz}\hat{z}) \tag{5.30}$$

The vertical component of the magnetic field may be restated by substituting the Hankel transform expression, equation 5.11, for $E_{S\phi}(\rho, z)$:

$$\frac{i}{\omega\rho}\frac{\partial}{\partial\rho}\left[\rho\int_0^\infty \bar{E}_{S\phi}(\lambda, z)\lambda J_1(\lambda\rho)\, d\lambda\right] = B_{Sz}(\rho, z), \tag{5.31}$$

using the identity

$$\frac{1}{i} = -i.$$

Consolidating the ρ terms under the integral and using the identity

$$\frac{1}{\rho}\frac{\partial}{\partial\rho}[\rho J_1(\lambda\rho)] = \lambda J_0(\lambda\rho), \tag{5.32}$$

equation 5.31 can be simplified to

$$B_{Sz}(\rho, z) = \frac{i}{\omega}\int_0^\infty \bar{E}_{S\phi}(\lambda, z)\lambda^2 J_0(\lambda\rho)\, d\lambda. \tag{5.33}$$

This Hankel transform is easily implemented using the digital filter method of Guptasarma and Singh. The kernel function $\bar{E}_{S\phi}(\lambda, z)$ is the same function found above using the finite element method.

A conductive halfspace model is shown in figure 5.1. A circular transmitter loop with

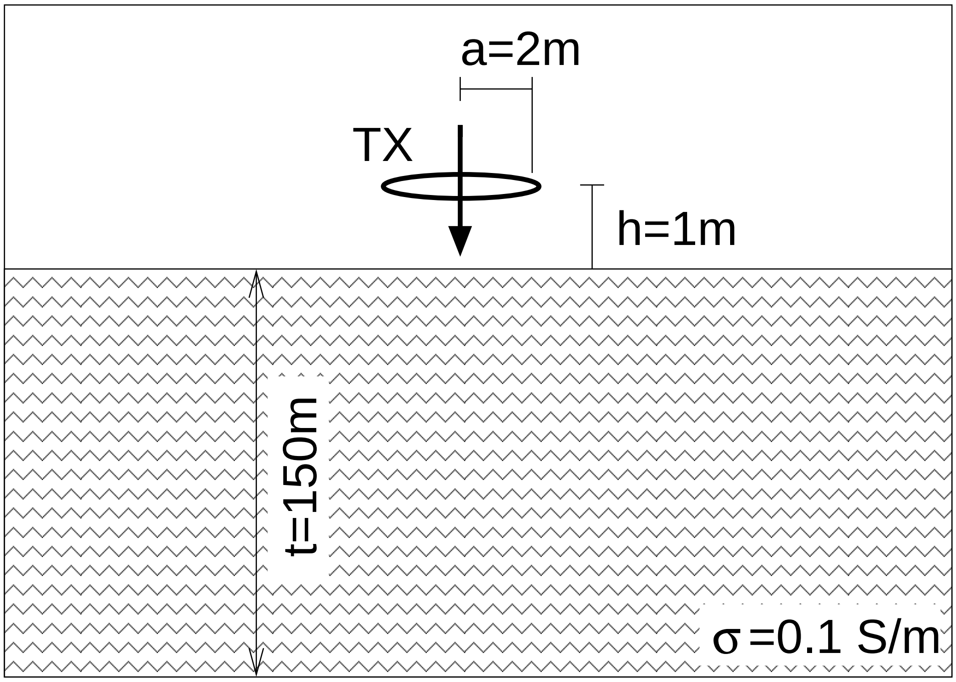

Fig. 5.1. A one-dimensional halfspace conductivity model. The transmitter operates at 1 kHz, with a maximum current of 2 A.

a radius of $a = 2$ m, a maximum current of $I = 2$ A, and a frequency of $f = 1$ kHz is placed $h = 1$ m above a halfspace of conductivity $\sigma = 0.1$ S/m. The model has a skin depth of $\delta \simeq 50$ m. The zero Dirichlet boundary condition will be set at a depth of $z_L = 150$ m, or three skin depths. The greatest variation in the $\bar{E}_S$ field occurs near the transmitter. Thus, the nodes are spaced geometrically, so that each element is 10% longer than the previous element.

The real and imaginary components of the secondary wavenumber domain electric field, $\bar{E}_S(\lambda, z)$ for radial distances of $\rho = 5$ m, 10 m, and 50 m from the transmitter, and for $\lambda = \lambda_{91}$ (where λ_{91} is the wavenumber calculated using the 91^{st} digital filter coefficient) are displayed in figures 5.2(a) and (b) respectively. The analytic solution is also displayed for comparison. The finite element and analytic solutions compare well.

The total electric field in the wavenumber domain for this model is shown in figure 5.3, again compared with the analytic solution. The agreement with the analytic solution is again quite good.

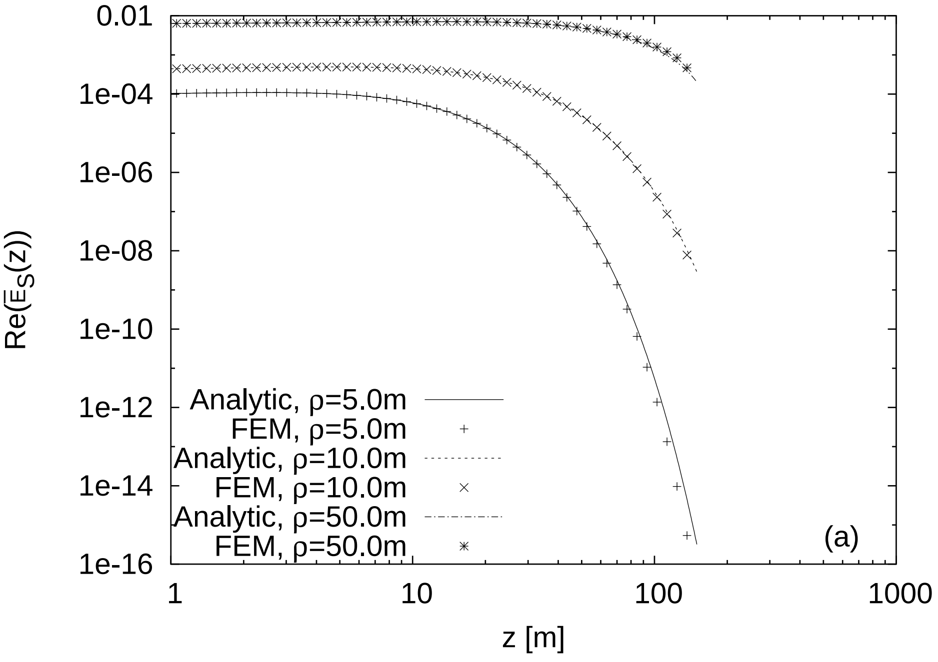

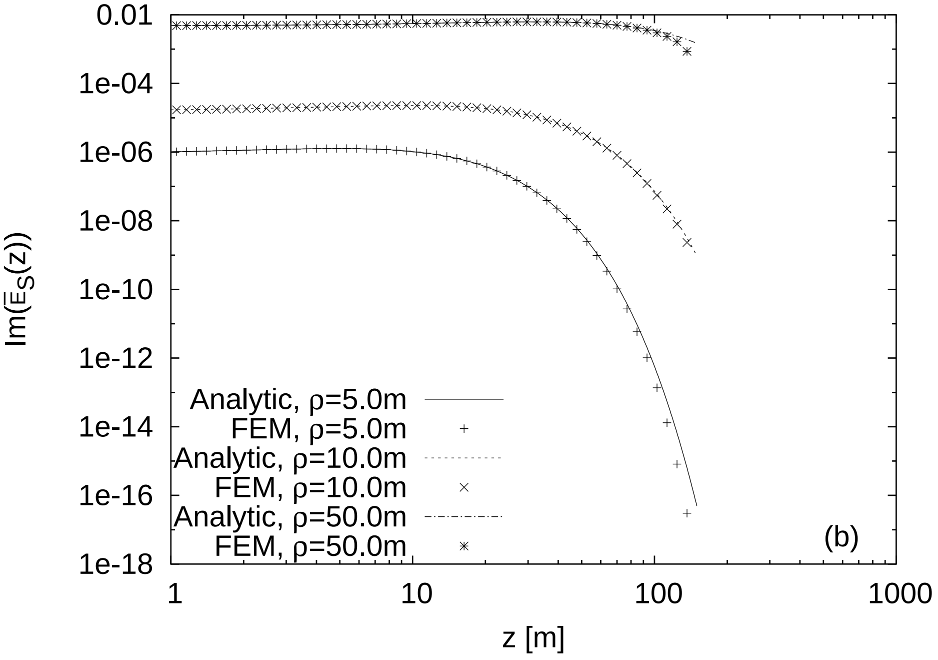

Fig. 5.2. The real and imaginary parts of $\bar{E}_S(\lambda, z)$, for the halfspace illustrated in figure 5.1.

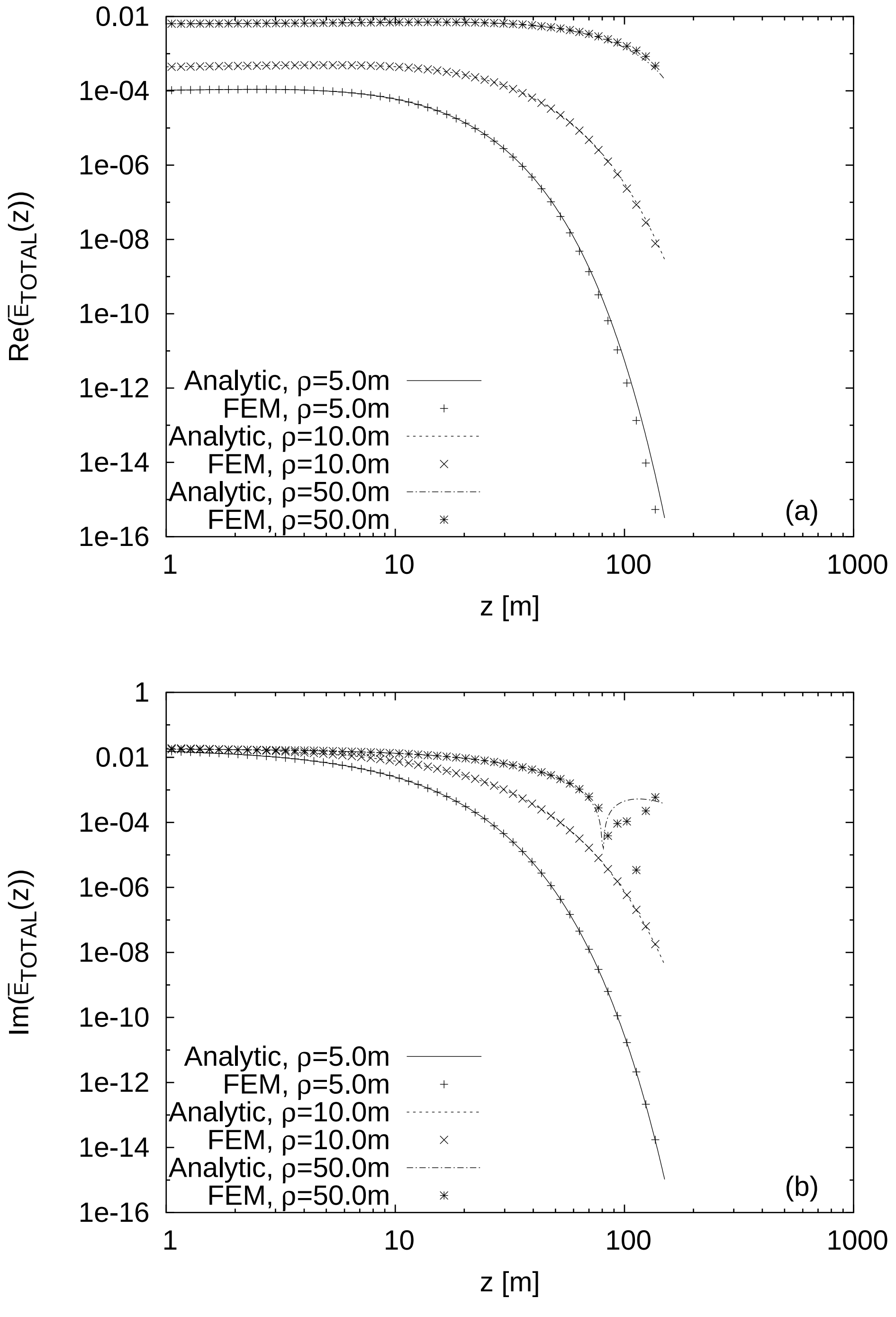

Fig. 5.3. The real and imaginary parts of $\bar{E}_{TOTAL}(\lambda, z)$, for the halfspace illustrated in figure 5.1.

The total electric field in the spatial (ρ, z) domain is displayed in figure 5.4. The finite element solution agrees well with the analytic solution for all but the farthest nodes from the transmitter.

A two-layer one dimensional model is illustrated in figure 5.5. This model is essentially the same as the halfspace model discussed above with an added 35 m thick layer of conductivity $\sigma_0 = 1.0$ S/m. The real and imaginary components of $\bar{E}_S(\lambda_{91}, z)$, $\bar{E}_{TOTAL}(\lambda_{91}, z)$ and $E_{TOTAL}(\rho, z)$ are provided in figures 5.6, 5.7, and 5.8 respectively.

The analytic solution is again included for comparison. As before, the wavenumber domain finite element solutions agree very well with the analytic solution. However, the spatial domain solution contains errors at the interface between the two layers and at depth. The error is presumed to arise from several sources. Errors at the interface between the layers may be due to rounding error in the digital filter Hankel transform. Also, the analytic solution has a discontinuity at the layer interface, which the finite element solution can only approximate. Additionally, at wavenumbers λ_i where i is small, λ becomes large, and at depths of $z = 150$ m, the zero Dirichlet boundary condition is no longer valid.

Three Dimensional EM Modeling

Maxwell's equations formulated in terms of the Coulomb-gauged magnetic vector potential $\mathbf{A}$ and the scalar electric potential Ψ are recalled:

$$\nabla^2 \mathbf{A}_S - i\omega\mu_0\sigma(\mathbf{A}_S + \nabla\Psi_S) = i\omega\mu_0\sigma_S(\mathbf{A}_P + \nabla\Psi_P) = \mathbf{f} \tag{5.34}$$

$$\nabla \cdot [-i\omega\mu_0\sigma(\mathbf{A}_S + \nabla\Psi_S)] = \nabla \cdot [i\mu_0\omega\sigma_S(\mathbf{A}_P + \nabla\Psi_P)] = g. \tag{5.35}$$

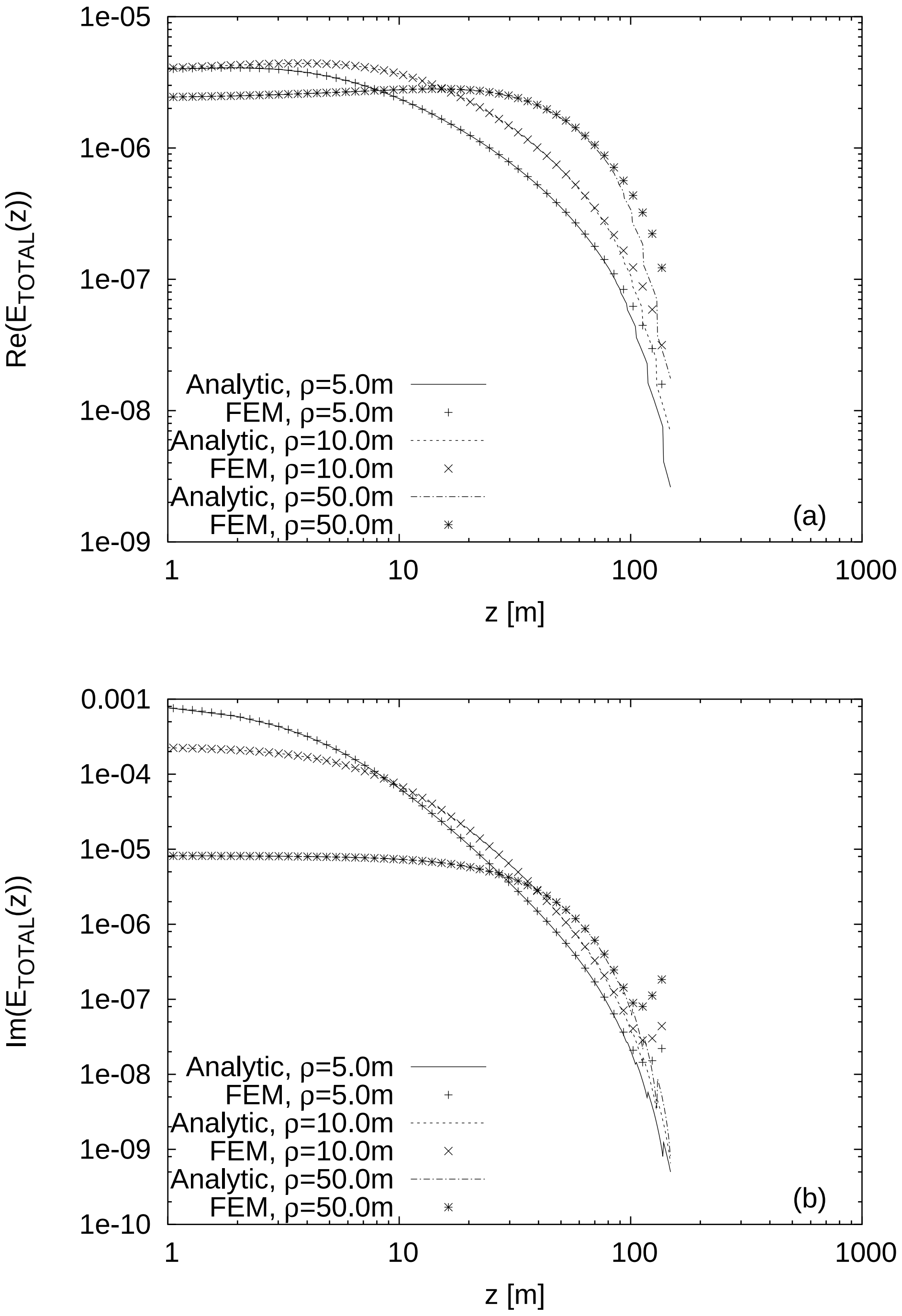

Fig. 5.4. The real and imaginary parts of $E_{TOTAL}(\rho, z)$ for the halfspace illustrated in figure 5.1.

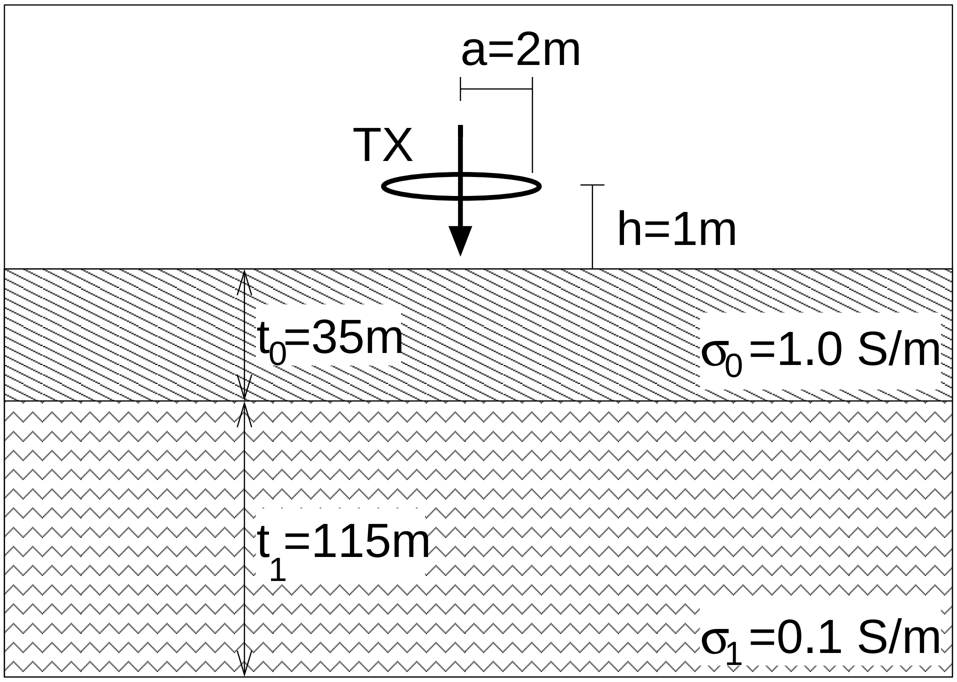

Fig. 5.5. A two layer one-dimensional conductivity model.

Each unknown function is expanded in the finite element basis,

$$A_{Sx}(x,y,z) = \sum_j A_{Sxj}\alpha_j(x,y,z) + \sum_k A_{Sxk}\alpha_k(x,y,z) \tag{5.36}$$

$$A_{Sy}(x,y,z) = \sum_j A_{Syj}\alpha_j(x,y,z) + \sum_k A_{Syk}\alpha_k(x,y,z) \tag{5.37}$$

$$A_{Sz}(x,y,z) = \sum_j A_{Szj}\alpha_j(x,y,z) + \sum_k A_{Szk}\alpha_k(x,y,z) \tag{5.38}$$

$$\Psi_S(x,y,z) = \sum_j \Psi_{Sj}\alpha_j(x,y,z) + \sum_k \Psi_{Sk}\alpha_k(x,y,z), \tag{5.39}$$

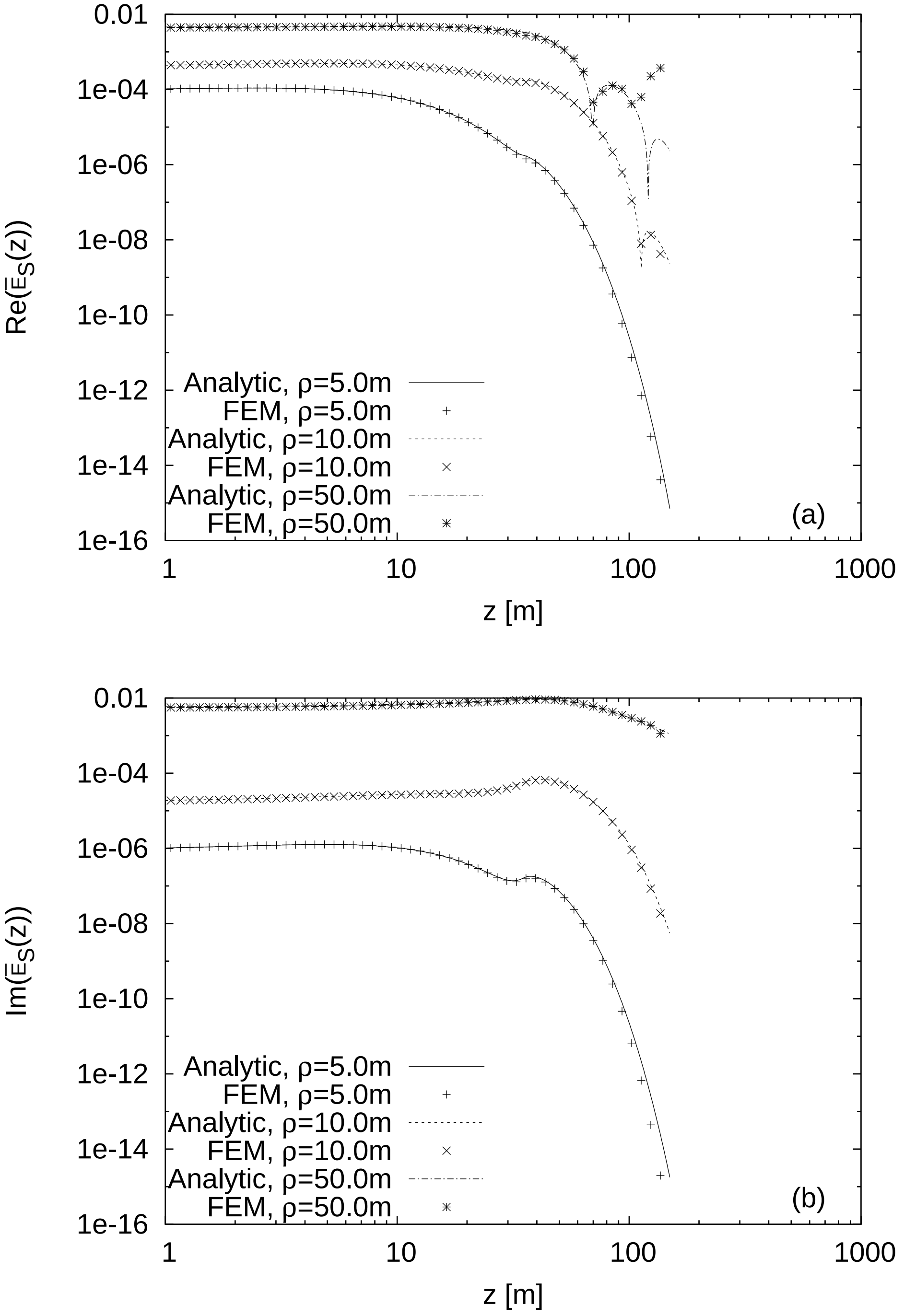

Fig. 5.6. The real and imaginary parts of $\bar{E}_S(\lambda, z)$ for the two-layer model illustrated in figure 5.5.

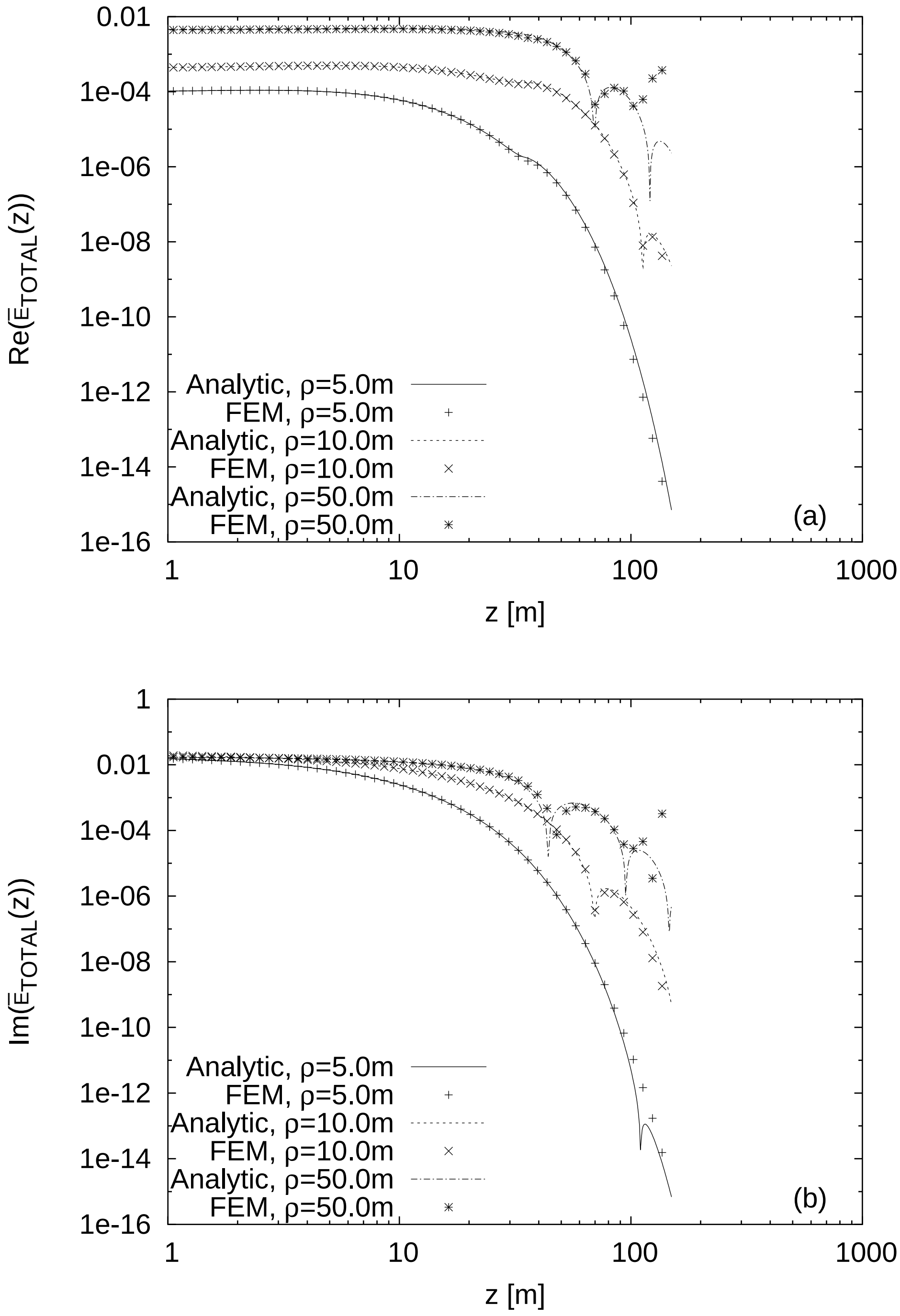

Fig. 5.7. The real and imaginary parts of $\bar{E}_{TOTAL}(\lambda, z)$ for the two-layer model illustrated in figure 5.5.

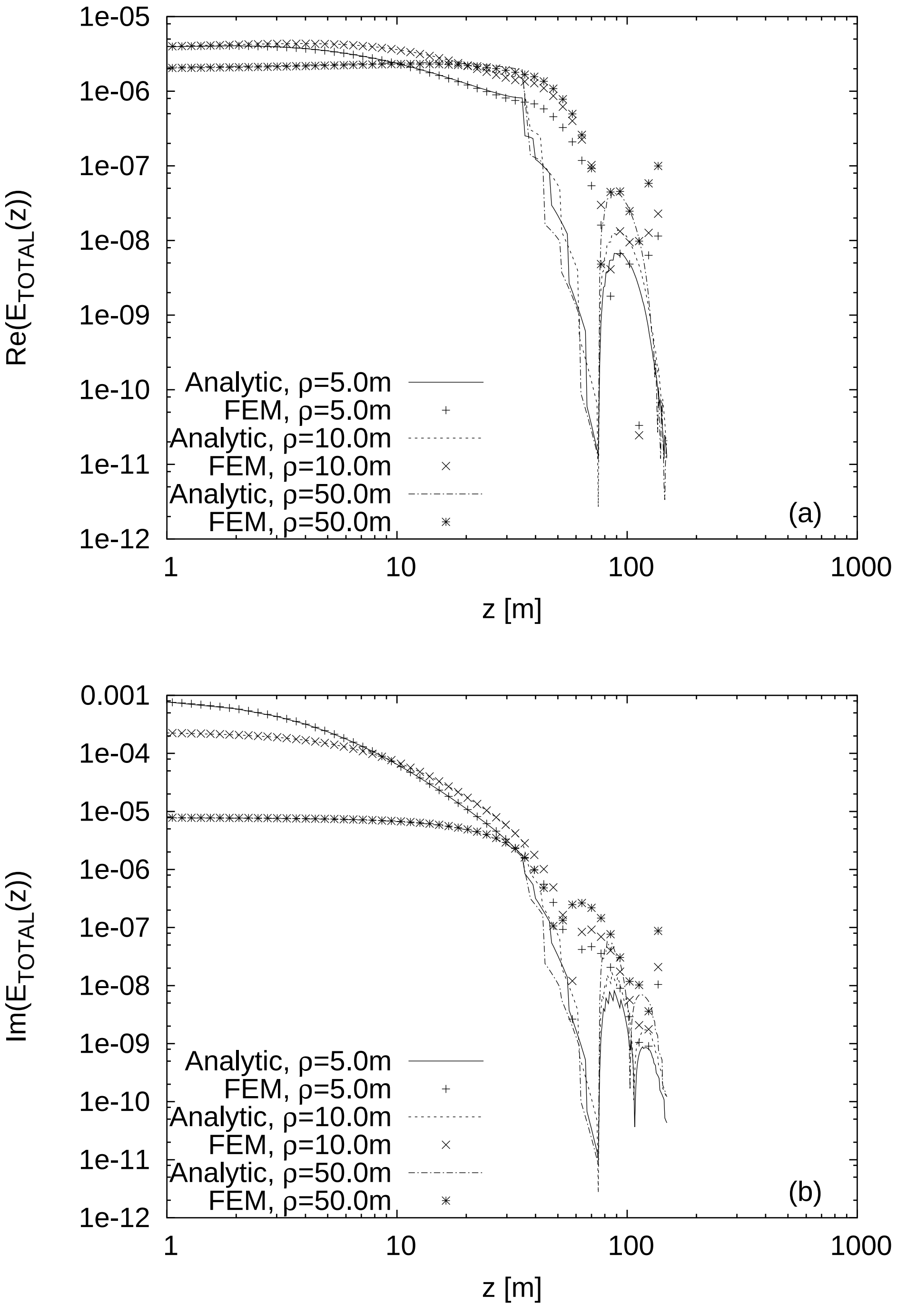

Fig. 5.8. The real and imaginary parts of $E_{TOTAL}(\rho, z)$ for the two-layer model illustrated in figure 5.5.

and substituted back into equations 5.34 and 5.35. The Galerkin method is applied to equation 5.34, and Green's theorem is invoked to reduce the order of differentiation:

$$\begin{aligned}\sum_j [A_{Sx_j}(-\mathcal{T}_{ij} - i\omega\mu_0\mathcal{R}_{ij}) - i\omega\mu_0\Psi_{S_j}\mathcal{L}_{ij}] = (f_x, \alpha_i)\\ - \sum_k [A_{Sx_k}(-\mathcal{T}_{ik} - i\omega\mu_0\mathcal{R}_{ik}) - i\omega\mu_0\Psi_{S_k}\mathcal{L}_{ik}]\end{aligned} \tag{5.40}$$

$$\begin{aligned}\sum_j [A_{Sy_j}(-\mathcal{T}_{ij} - i\omega\mu_0\mathcal{R}_{ij}) - i\omega\mu_0\Psi_{S_j}\mathcal{M}_{ij}] = (f_x, \alpha_i)\\ - \sum_k [A_{Sy_k}(-\mathcal{T}_{ik} - i\omega\mu_0\mathcal{R}_{ik}) - i\omega\mu_0\Psi_{S_k}\mathcal{M}_{ik}]\end{aligned} \tag{5.41}$$

$$\begin{aligned}\sum_j [A_{Sy_j}(-\mathcal{T}_{ij} - i\omega\mu_0\mathcal{R}_{ij}) - i\omega\mu_0\Psi_{S_j}\mathcal{N}_{ij}] = (f_x, \alpha_i)\\ - \sum_k [A_{Sy_k}(-\mathcal{T}_{ik} - i\omega\mu_0\mathcal{R}_{ik}) - i\omega\mu_0\Psi_{S_k}\mathcal{N}_{ik}],\end{aligned} \tag{5.42}$$

where

$$\mathcal{T}_{ij} = (\nabla\alpha_i, \nabla\alpha_j)_\Omega \qquad \mathcal{R}_{ij} = (\alpha_i, \sigma\alpha_j)_\Omega$$

$$\mathcal{L}_{ij} = \left(\alpha_i, \sigma\frac{\partial\alpha_j}{\partial x}\right)_\Omega \qquad \mathcal{M}_{ij} = \left(\alpha_i, \sigma\frac{\partial\alpha_j}{\partial y}\right)_\Omega \qquad \mathcal{N}_{ij} = \left(\alpha_i, \sigma\frac{\partial\alpha_j}{\partial z}\right)_\Omega .$$

The terms $\mathcal{T}_{ij}$ and $\mathcal{R}_{ij}$ are calculated as before, taking into account the additional conductivity term in $\mathcal{R}$. The remaining terms are easily calculated using the method of Eisenberg and Malverne (1973):

$$\mathcal{L}_{ij} = \sum_\tau \frac{V_\tau\sigma_\tau}{4}\frac{\partial\alpha^{(\tau)}_{j\ local}}{\partial x} \qquad \mathcal{M}_{ij} = \sum_\tau \frac{V_\tau\sigma_\tau}{4}\frac{\partial\alpha^{(\tau)}_{j\ local}}{\partial y} \qquad \mathcal{N}_{ij} = \sum_\tau \frac{V_\tau\sigma_\tau}{4}\frac{\partial\alpha^{(\tau)}_{j\ local}}{\partial z},$$

where τ is again each of the tetrahedra shared by nodes i and j.

Equation 5.35 is also subjected to the Galerkin method,

$$-i\omega\mu_0 \sum_j \left[A_{Sx_j}\mathcal{L}_{ij} + A_{Sy_j}\mathcal{M}_{ij} + A_{Sz_j}\mathcal{N}_{ij} + \Psi_{S_j}(\alpha_i, \nabla\cdot[\sigma\alpha_j])_\Omega\right] =$$
$$(g,\alpha_i) + i\omega\mu_0 \sum_k \left[A_{Sx_k}\mathcal{L}_{ik} + A_{Sy_k}\mathcal{M}_{ik} + A_{Sz_k}\mathcal{N}_{ik} + \Psi_{S_k}(\alpha_i, \nabla\cdot[\sigma\alpha_k])_\Omega\right], \tag{5.43}$$

and an identity related to Green's theorem,

$$(\alpha_i, \nabla\cdot[\sigma\alpha_j])_\Omega = -(\sigma\nabla\alpha_i, \nabla\alpha_j)_\Omega + \text{surface terms} \tag{5.44}$$

(Badea et al., 2001), and is rewritten as

$$\begin{aligned} &-i\omega\mu_0 \sum_j \left[A_{Sx_j}\mathcal{L}_{ij} + A_{Sy_j}\mathcal{M}_{ij} + A_{Sz_j}\mathcal{N}_{ij} - \Psi_{S_j}\mathcal{S}_{ij}\right] = \\ &\qquad (g,\alpha_i) + i\omega\mu_0 \sum_k \left[A_{Sx_k}\mathcal{L}_{ik} + A_{Sy_k}\mathcal{M}_{ik} + A_{Sz_k}\mathcal{N}_{ik} - \Psi_{S_k}\mathcal{S}_{ik}\right], \end{aligned} \tag{5.45}$$

where

$$\mathcal{S}_{ij} = (\nabla\alpha_i, \sigma\nabla\alpha_j)_\Omega,$$

which is calculated in a manner similar to $\mathcal{T}$, taking into account the additional conductivity term. The surface terms in equation 5.44 vanish because the basis functions vanish at the mesh boundary.

The magnetic potential **A** is a vector, and the equations are coupled together. Hence, the finite element algorithm must find a four component vector solution at each free node in the solution domain. Consequently, each i, j pair contributes a 4×4 submatrix to the finite element matrix.

The terms $(\mathbf{f}, \alpha_i)$ and (g, α_i) are simplified by expanding $\mathbf{f}$ and g in the finite element basis, and by recognizing that Ψ_P is everywhere zero:

$$(\mathbf{f}, \alpha_i) = i\omega\mu_0 \sum_{\ell} \mathbf{A}_{P_\ell}(\sigma_S \alpha_\ell, \alpha_i) \tag{5.46}$$

$$(g, \alpha_i) = i\omega\mu_0 \sum_{\ell} (\nabla \cdot \sigma_S \mathbf{A}_{P_\ell} \alpha_\ell, \alpha_i). \tag{5.47}$$

Invoking the identity in equation 5.44, equation 5.47 becomes

$$(g, \alpha_i) = i\omega\mu_0 \sum_{\ell} (A_{P_{x_\ell}} \mathcal{B}_{i\ell} + A_{P_{y_\ell}} \mathcal{C}_{i\ell} + A_{P_{z_\ell}} \mathcal{D}_{i\ell}), \tag{5.48}$$

where

$$\mathcal{B}_{i\ell} = \left(\sigma_S \frac{\partial \alpha_i}{\partial x}, \alpha_\ell\right)_\Omega \qquad \mathcal{C}_{i\ell} = \left(\sigma_S \frac{\partial \alpha_i}{\partial y}, \alpha_\ell\right)_\Omega \qquad \mathcal{D}_{i\ell} = \left(\sigma_S \frac{\partial \alpha_i}{\partial z}, \alpha_\ell\right)_\Omega .$$

The right hand sides of equations 5.34 and 5.35 require a known model response for the $\mathbf{A}$ and Ψ potentials. The models presented in this study used as the primary model either an inductively coupled finite current loop suspended in free space, or the same loop in an air layer at a height h above a halfspace of conductivity σ_P. For either of these models, the scalar potential Ψ is everywhere zero. The vector potential $\mathbf{A}_P$ is easily derived from Maxwell's equations. The derivation closely follows that of the one dimensional electric field of either model, and is not presented here.

The primary magnetic vector potential of a loop in free space is given by

$$\mathbf{A}_P(\rho, z) = \frac{\mu_0 I_0 a}{2} \int_0^\infty \exp(-\lambda|z + h|) J_1(\lambda a) J_1(\lambda \rho)\, d\lambda\ \hat{\phi}, \tag{5.49}$$

for a loop of radius a and current I_0. The same loop at height h above a halfspace of conductivity σ_P generates the primary vector potential

$$\mathbf{A}_P^{AIR} = \frac{\mu_0 I_0 a}{2} \int_0^\infty [\exp(-\lambda|z+h|) + R\exp(-\lambda|z-h|)] J_1(\lambda a) J_1(\lambda\rho)\, d\lambda\, \hat{\phi} \tag{5.50}$$

$$\mathbf{A}_P^{EARTH} = \frac{\mu_0 I_0 a}{2} \int_0^\infty [\exp(-\lambda h) + R\exp(-\lambda h)] \exp(-i\gamma z) J_1(\lambda a) J_1(\lambda\rho)\, d\lambda\, \hat{\phi}, \tag{5.51}$$

where R is the reflection coefficient defined as

$$R = \frac{\lambda + i\gamma}{\lambda - i\gamma}, \tag{5.52}$$

and γ is defined by equation 5.15.

Solution of equations 5.34 and 5.35 yields the discrete values of the electromagnetic potentials $\mathbf{A}$ and Ψ at the nodes of the finite element mesh. The electric field $\mathbf{E}$ and the magnetic field $\mathbf{H}$ must be recovered from the potentials by numerical differentiation. A review of numerical differentiation algorithms well-suited for this operation is found in Omeragic and Silvester (1996). In some cases, simple differencing of nodal values is sufficient, but often, this can lead to significant errors. This is particularly true when the mesh is irregular, as is the case when local refinement is used (Badea et al., 2001).

Following Badea et al. (2001), derivatives are obtained with the moving least squares interpolation (MLSI) algorithm (Tabarra et al., 1994). If the spatial derivatives of discrete data set are desired at point P, then a linear function of the form $ax + by + cz + d$ is fit to the value of the potential at the N finite element mesh nodes closest (in space) to point P. The fit is accomplished by minimizing the residual between the linear function and these potential values, weighted according to distance from point P. The weighting function,

$$w(x,y,z) = \exp\left(-c^2\left[\left(\frac{x - x_P}{dx_{max}}\right)^2 + \left(\frac{y - y_P}{dy_{max}}\right)^2 + \left(\frac{z - z_P}{dz_{max}}\right)^2\right]\right), \tag{5.53}$$

causes the influence of each node to fall off exponentially with distance from P. The algorithm requires the specification of appropriate values for N and c. However, the default values, N= 20 and $c = 3.0$ recommended by Tabarra, et al. (1994) are sufficient in most

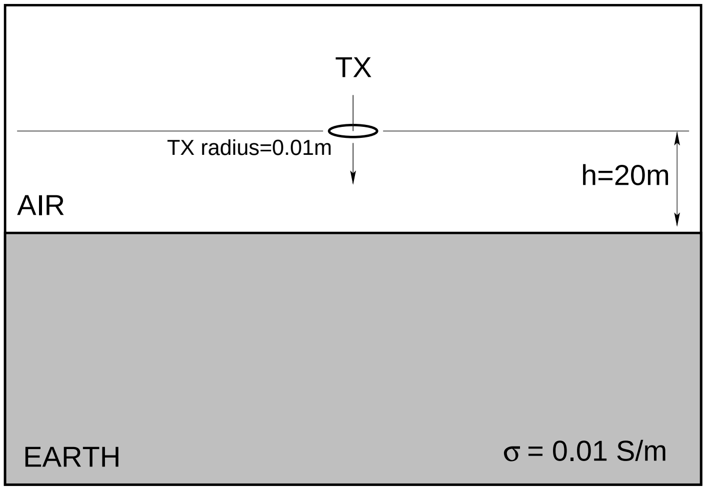

Fig. 5.9. A three-dimensional double halfspace model. The transmitter operates at a frequency of 30 kHz and has a moment of 1 A m^2.

cases.

Double halfspace model— A double halfspace conductivity model $\sigma(\mathbf{r})$ is illustrated in figure 5.9. The upper halfspace is intended to represent an air layer, and as such the conductivity of the upper halfspace is made arbitrarily small ($\sigma = 1 \times 10^{-20}$ S/m). The lower halfspace is assigned a conductivity of 0.01 S/m. The transmitter is a circular current loop oscillating at a frequency of 30 kHz with a maximum amplitude of 6 A, at a height of 20 meters above the lower halfspace. Receivers sensitive to the z-component of the magnetic field are located every five meters from -100 m$\leq x \leq 100$ m. The primary fields were those of the transmitter located in free space.

The secondary vertical magnetic field at the receiver locations are compared in figure 5.10 to an analytic solution taken from Ward and Hohmann (1987) for several different mesh sizes. In each case, the node separation distance is 10 meters in x, y, and z. As the boundaries of the mesh are placed further from the transmitter, the finite element solution approaches the field calculated analytically. The primary magnetic field induces a broad, diffuse current density in the lower halfspace that decays slowly away from the transmitter. The secondary magnetic field of this current density is incorrectly modeled if the secondary potentials are forced to zero too rapidly by mesh boundaries that are not sufficiently distant

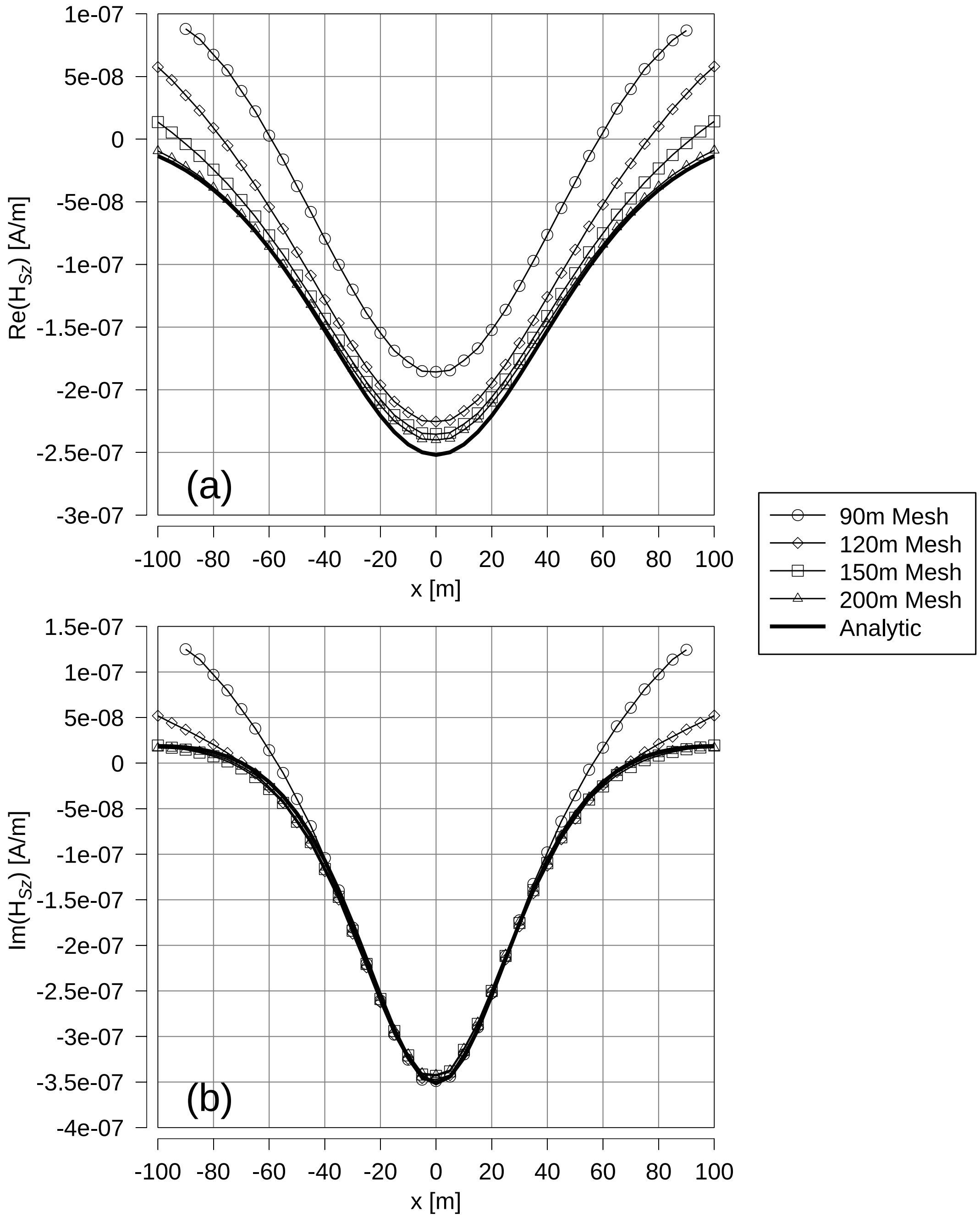

Fig. 5.10. The real (a) and imaginary (b) parts of the secondary vertical magnetic field calculated for the double halfspace model in figure 5.9 using the finite element algorithm, compared to the analytic solution. The results are shown for several different mesh sizes, emphasizing that using a mesh of insufficient physical extent may result in misleading modeling results.

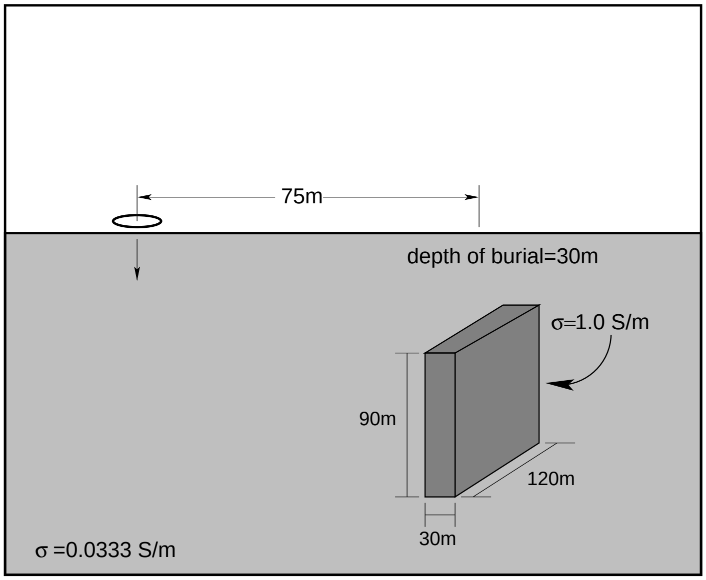

Fig. 5.11. A fully three-dimensional conductivity model. Modified from Pridmore, et al. (1981).

from the transmitter. However, the physical dimensions of more complex models may be limited by using an analytic double halfspace primary potential.

Buried conductive slab— A fully three-dimensional conductivity model is created by placing a conductive prism in a conductive halfspace below an insulating air layer. The model is configured to the dimensions specified in Pridmore, et al. (1981), and is illustrated in figure 5.11. The finite element results will be compared to the results obtained by Pridmore, et al., which in turn have been verified against integral equation calculations described in Hohmann (1975). The modeling results of Pridmore, et al. were calculated using a finite element formulation of Maxwell's equations in terms of the electric field. The magnetic field was recovered via numerical differentiation of the calculated electric field using both simple node differencing and a Green's function approach. The electric field response of the three-dimensional conductivity model calculated by this finite element approach did not match well with previous integral equation solutions. However, the magnetic fields derived therefrom did agree well with the integral equation solution when the Green's function approach was used to calculate the required derivatives.

The transmitter is placed directly on the surface of the lower halfspace 75m to the left of the slab center in x. It is a current loop oscillating at a frequency of 1 kHz, with a radius of 1 meter, and a maximum current of 4 A. The slab is buried at a depth of 30 meters, and is assigned a conductivity of 1 S/m. The slab measures 30 meters in the x-direction, 120 meters in the y-direction, and 90 meters in the z-direction. The transmitter is located at $x = 225$ m, and the slab is centered at $x = 300$ m. The lower halfspace is assigned a conductivity of 0.0333 S/m, providing a 30:1 conductivity contrast between the slab and the host medium.

The dimensions of the slab suggest an initial mesh discretization of 30 meters in all Cartesian directions. The initial mesh measures $1230 \times 1200 \times 900$ meters, requiring $42 \times 41 \times 31 = 53382$ nodes. The values of 4 unknown quantities (the three Cartesian components of the vector potential $\mathbf{A}$, and the single component of the scalar potential Ψ) are desired at each node, so that a total of 213528 unknown values are requested from the finite element algorithm. Although the finite element matrix is sparse, each non-zero node matrix location ij contributes a 4×4 submatrix to the finite element matrix, each containing ten nonzero entries, for a total of 6,482,220 nonzero entries. Runtime for this model is approximately 3 hours on a dual-processor 750 MHz Pentium III computer. No optimization is applied.

The results are displayed in figure 5.12 for a profile from $x = 0$ m to $x = 600$ m, where $y = z = 0$ m. A reasonably good fit is achieved for the real part of the vertical magnetic field. However, the imaginary fit is less than ideal. The poor fit is most likely attributable to a lack of resolution of minute details in the secondary potential within the plate and at the conductivity contrast between the plate and the host, or to a choice of MLSI parameters that are inappropriate for the current model.

Local mesh refinement in the region of the plate is applied to overcome the lack of resolution in the secondary potentials. Figure 5.13 depicts the region of the mesh that is refined, and a plan view of a horizontal slice through the mesh. Figure 5.14 compares the results of Pridmore, et al. to the locally refined finite element numerical results. The fit for the imaginary part is better, but the agreement of the real part has lessened somewhat.

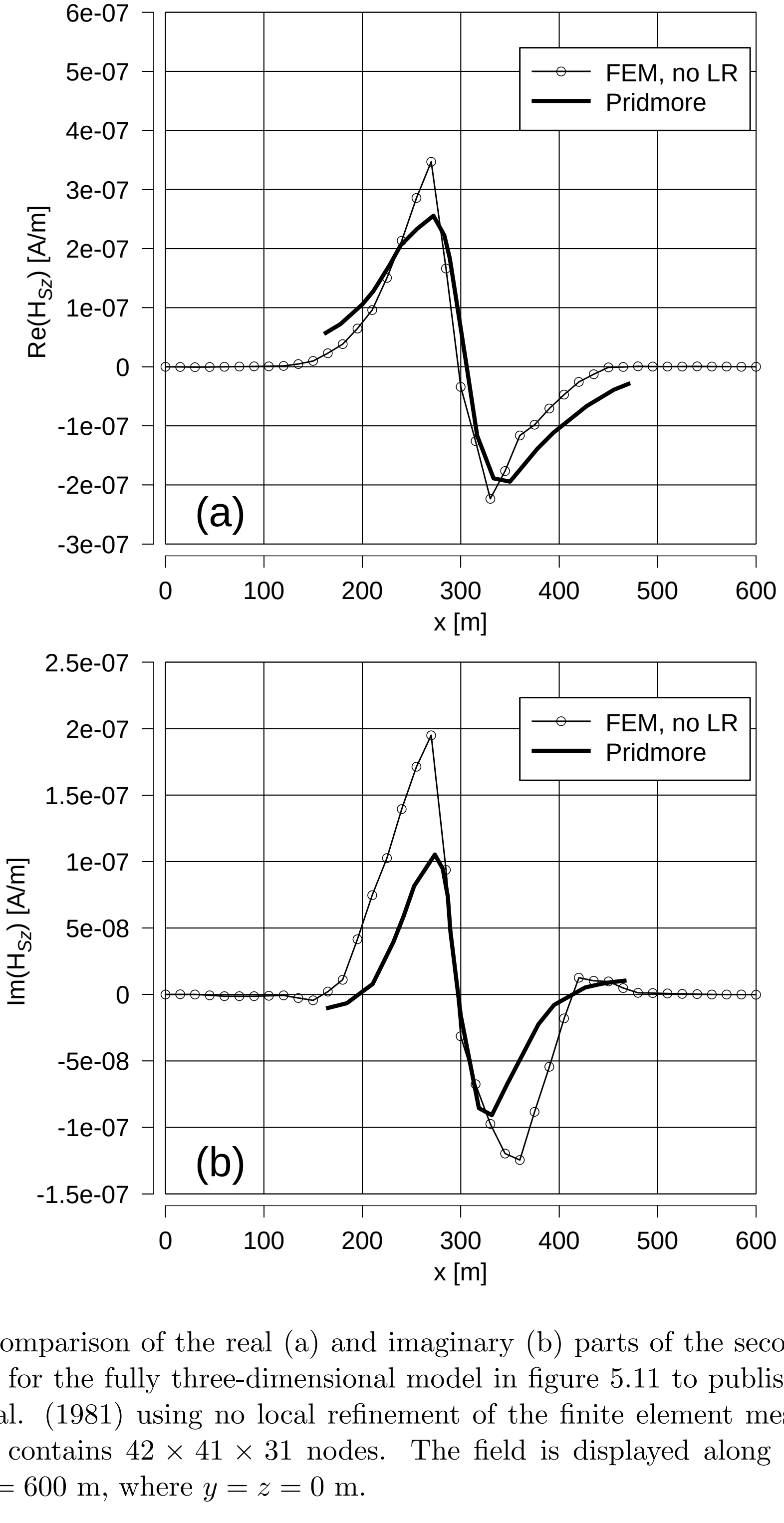

Fig. 5.12. A comparison of the real (a) and imaginary (b) parts of the secondary vertical magnetic field for the fully three-dimensional model in figure 5.11 to published results by Pridmore, et al. (1981) using no local refinement of the finite element mesh. The finite element mesh contains 42 × 41 × 31 nodes. The field is displayed along a profile from $x = 0$ m to $x = 600$ m, where $y = z = 0$ m.

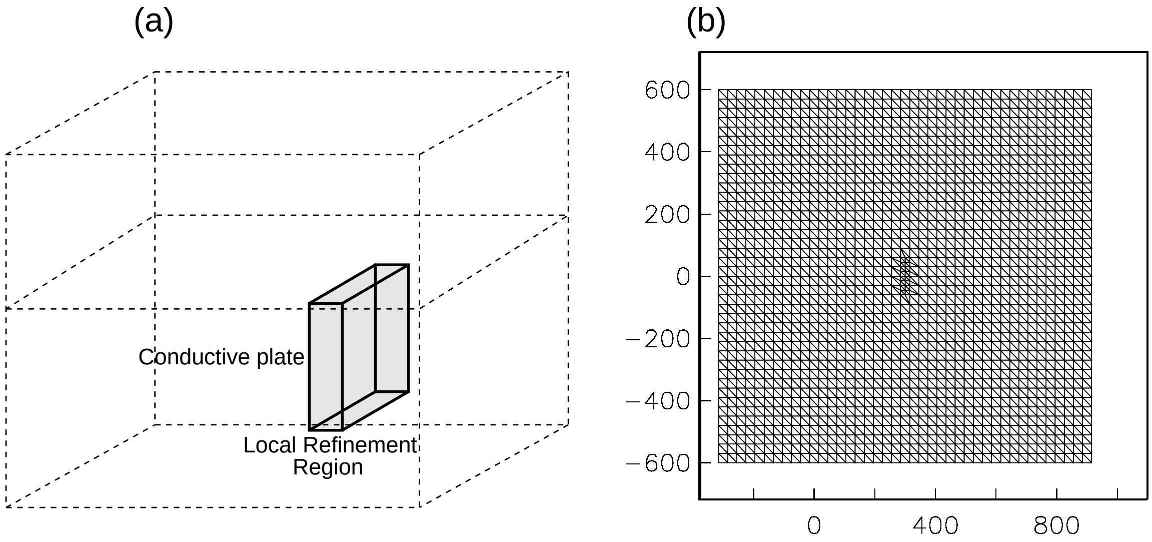

Fig. 5.13. The first local refinement of the initial 42 × 41 × 31 node mesh (a), and a horizontal slice (b) through the finite element mesh at $z = 60$ m. The refined portion of the mesh is simply the region of the buried slab.

An aberrant spike has also appeared in the finite element results over the center of the slab. This appears to be an MLSI error. The MLSI algorithm seeks the N nodes closest to the point at which the spatial derivatives are desired. At locations near a region of local refinement, a larger number of nodes from the refined region are used in the spatial derivative calculation than nodes from the unrefined regions, simply because the refined nodes are more closely spaced, generating misleading derivative values.

A second level of local refinement is illustrated in figure 5.15. Although the electromagnetic potentials of the lower halfspace containing the conductive slab have been relegated to the primary model, these potentials enter the finite element calculation as the driving function on the right hand side of the equation. Only the values of the primary potentials at the nodes are used in the formulation of the right hand side. Thus, a mesh that is not sufficiently fine may not represent small-scale changes in the primary potentials, leading to inaccurate modeling results. With this in mind, the mesh is further refined in a region where the majority of these small-scale variations occur. In particular, a secondary current that is a image of the transmitter current arises in the halfspace beneath the transmitter in an attempt to neutralize the flux of the transmitter though the host medium, according to

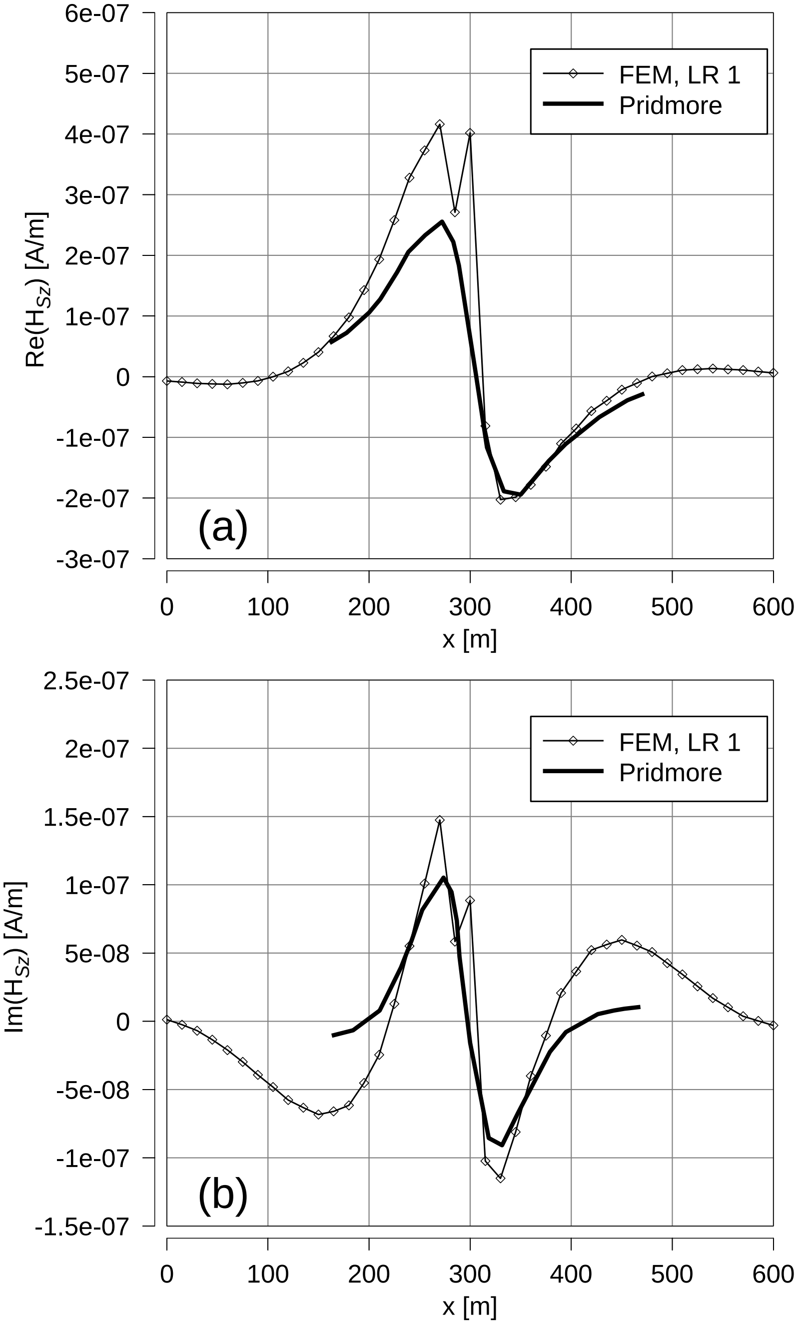

Fig. 5.14. A comparison of the real (a) and imaginary (b) parts of the secondary vertical magnetic field for the fully three-dimensional model in figure 5.11 to published results by Pridmore, et al. (1981), where the finite element mesh has been locally refined using the refinement region illustrated in figure 5.13.

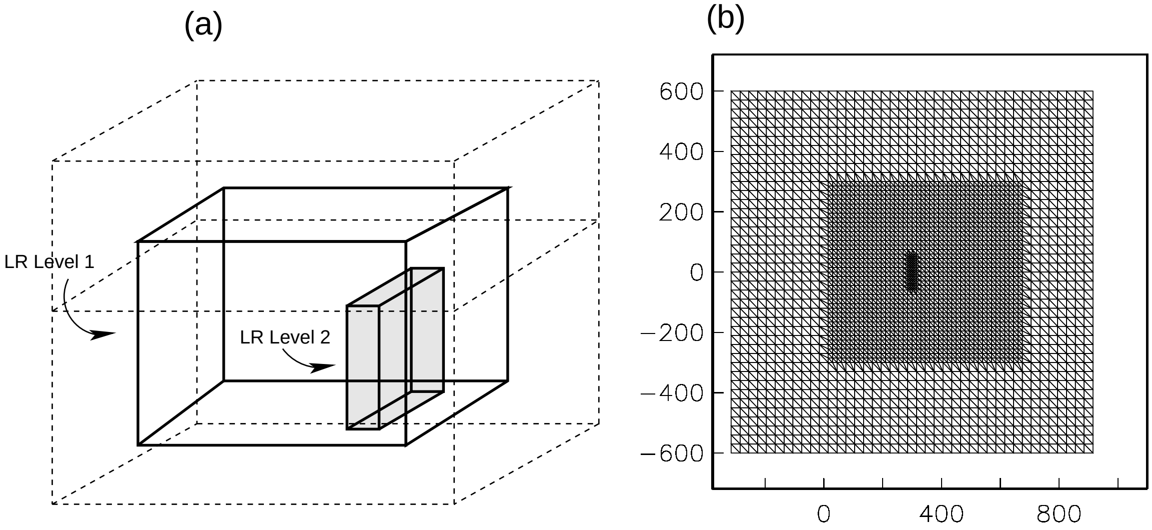

Fig. 5.15. The second local refinement (a) of the mesh for the model in figure 5.11, and a plan view of a horizontal slice (b) through the FE mesh at $z = 60$ m. Two nested local refinements are defined in order to better resolve the behavior of the driving potential $\mathbf{A}_P$.

Lenz's Law. A region is refined from one mesh spacing above the transmitter ($z = -30$ m), extending to one mesh spacing below the conductive slab ($z = 150$ m), and extending from $x = 0$ m to $x = 700$ m, and from $y = -300$ m to $y = 300$ m. Although conceptually this mesh refinement best conforms to the governing physics, the results, shown in figure 5.16, are not quite in agreement with Pridmore, et al.

The imaginary portion of the previous results (figure 5.16(b)) suggests that the mesh boundaries are not sufficiently distant from the slab. A magnetic field decays more slowly in free space than in a conductive medium, and the secondary conductivity model is that of a slab of conductivity $\Delta\sigma = \sigma_{SLAB} - \sigma_{HOST}$ suspended in free space. Therefore, a mesh with boundaries much farther from the slab is defined, as illustrated in figure 5.17. The mesh dimensions are extended to 2400 meters in x, y, and z. The initial (unrefined) node spacing for this mesh is 120 m. Three nested refinements are applied. The first of these refinements covers the region from $-75 \leq x \leq 645$, $-360 \leq y \leq 360$, and $-240 \leq z \leq 480$ meters. The second refinement is of the region demarcated by $165 \leq x \leq 405$, $-120 \leq y \leq 120$, and $-60 \leq z \leq 300$ meters. The final refinement is of the region $255 \leq x \leq 345$, $-90 \leq y \leq 90$, and $30 \leq z \leq 120$ meters. Figure 5.18 shows the model results. An improved agreement

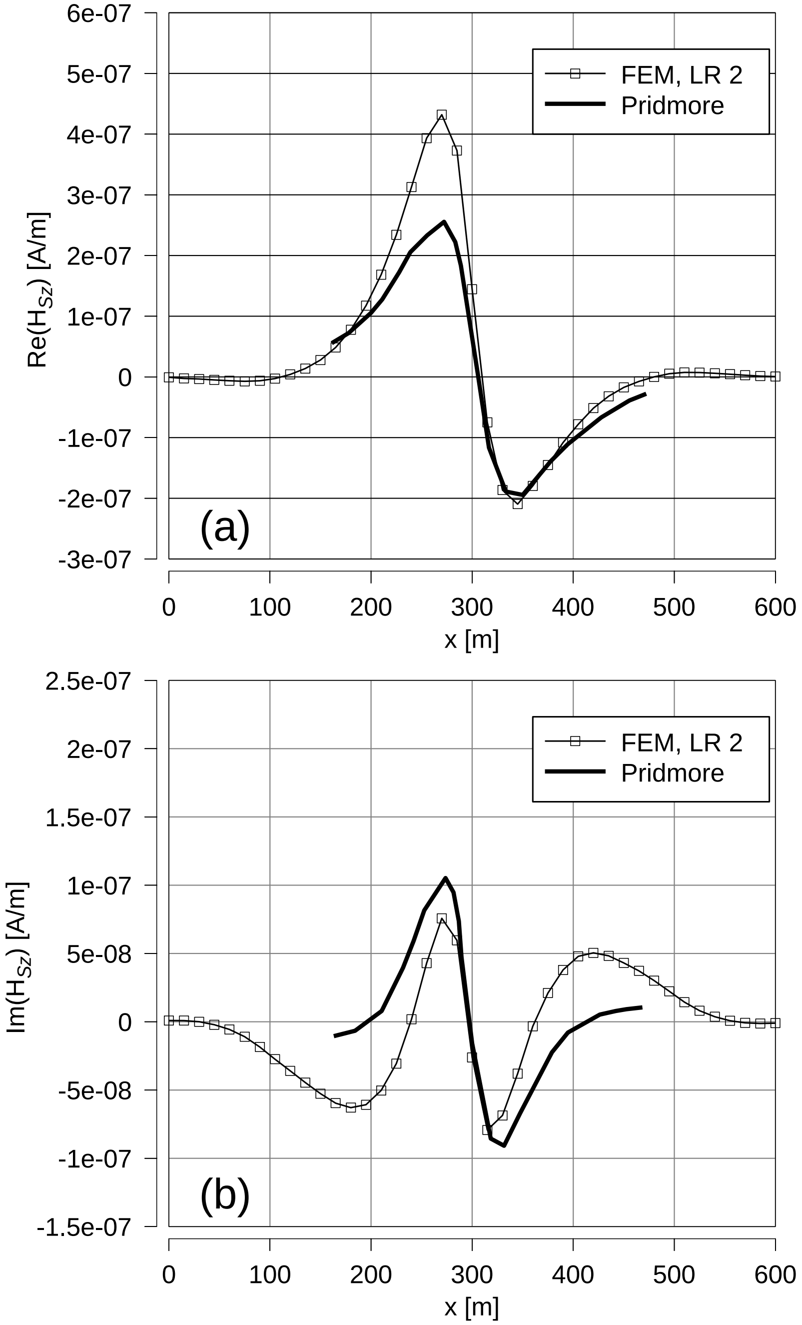

Fig. 5.16. A comparison of the real (a) and imaginary (b) parts of the secondary vertical magnetic field for the model in figure 5.11 to the published results of Pridmore, et al., where the FE mesh has been locally refined as shown in figure 5.15.

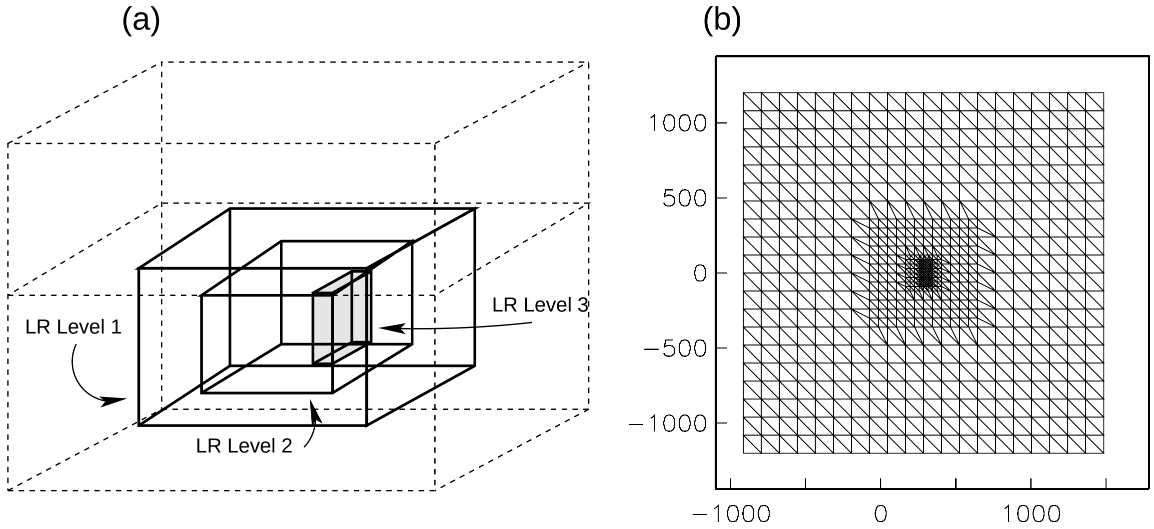

Fig. 5.17. New mesh boundaries and local refinements (a) for the model in figure 5.11, and a horizontal slice (b) through the finite element mesh at $z = 60$ m.

at distance from the buried slab is observed. However, the agreement near the plate again leaves something to be desired. A satisfactory agreement would most likely be achieved using a large mesh that is refined similar to figure 5.15. Such a mesh is beyond the memory limitations of the computer used in this study. Nonetheless, I believe that the data presented above represent a satisfactory agreement with the results published by Pridmore, et al. (1981).

The agreement may be further polished by optimizing the MLSI parameters N and c, described above. The second model (figure 5.15) is chosen for this exercise because, despite mediocre agreement with the published data, the mesh refinement in this model is the most physically valid. The results for several values of N and c are displayed en masse in figures 5.19 and 5.20. It is immediately observed that the adjustment of the MLSI parameters can have a significant effect on the magnetic field calculation. It may also be observed that the parameters that yield the best agreement for the real part of the magnetic field are not the same parameters that yield the best agreement for the imaginary part. This is due to a difference in the spatial morphology of the real and imaginary parts of the vector potential **A**. The best qualitative agreement with the published results by Pridmore, et al. for both

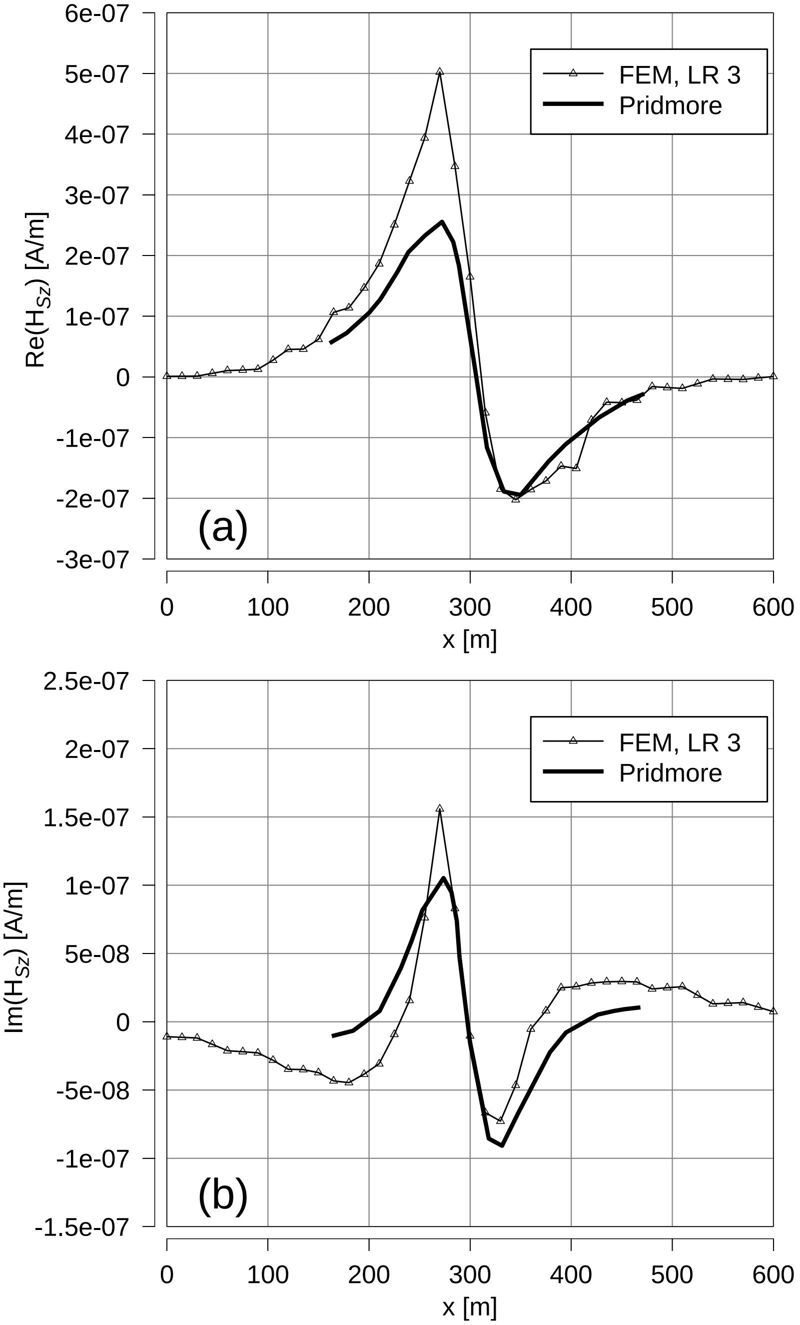

Fig. 5.18. A comparison of the real (a) and imaginary (b) parts of the secondary vertical magnetic field for the model in figure 5.11 to the published results of Pridmore, et al, where the FE mesh has been extended in size and locally refined as shown in figure 5.17.

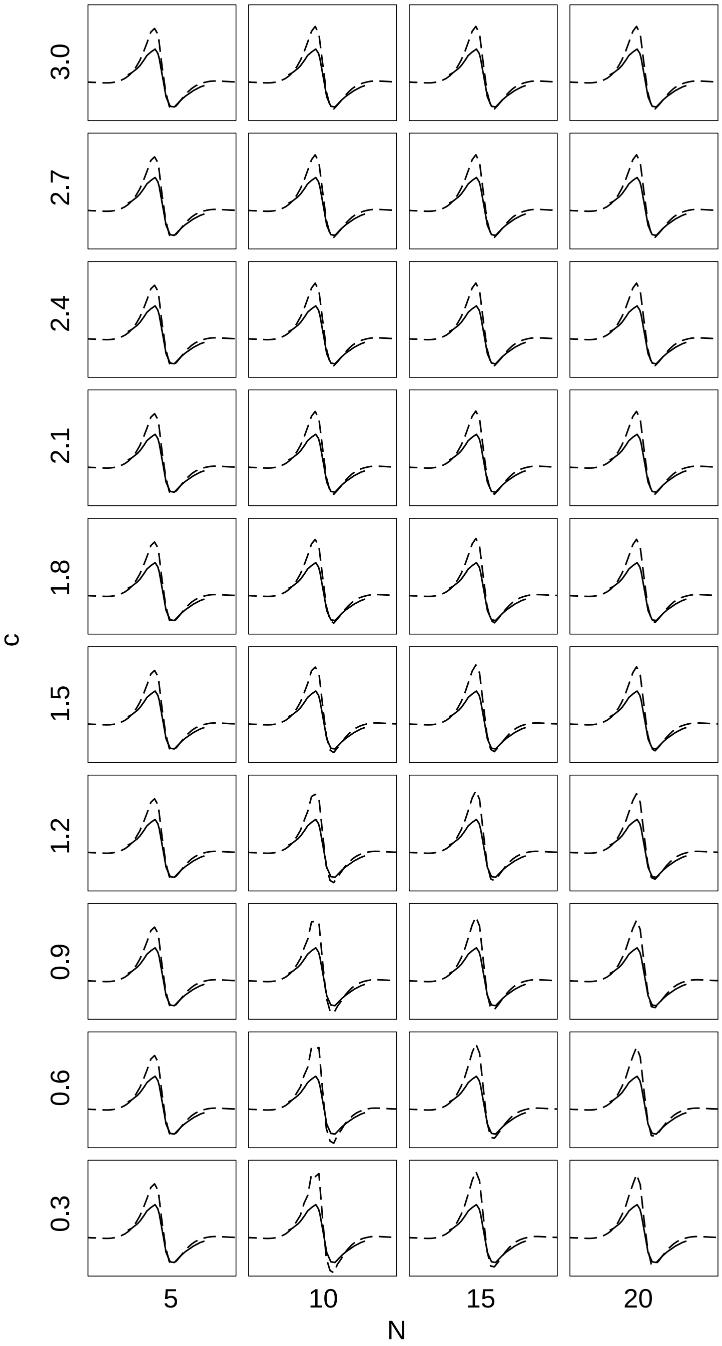

Fig. 5.19. The effect of altering the MLSI parameters N and c on the comparison of the real part of the secondary vertical magnetic field of the model in figure 5.11 (dashed line), using the local refinement illustrated in figure 5.15 with the published results (solid line) of Pridmore et al.

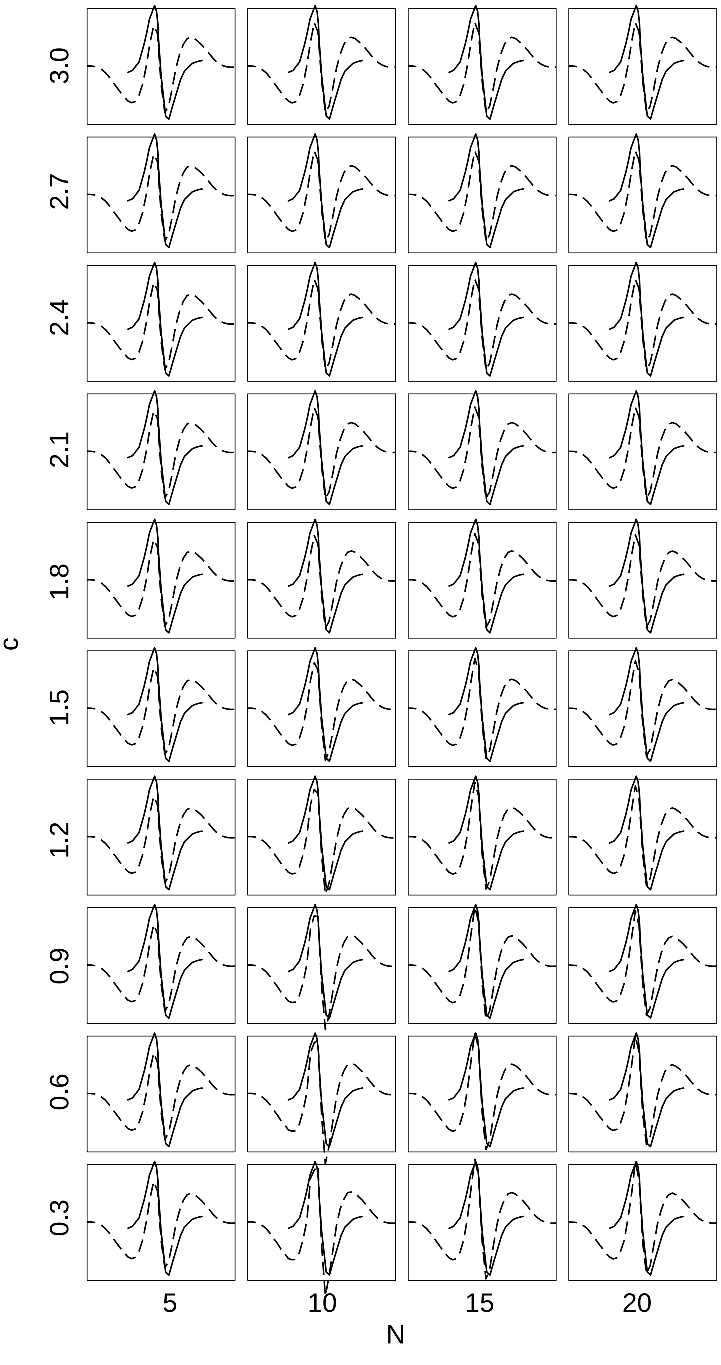

Fig. 5.20. The effect of altering the MLSI parameters N and c on the comparison of the imaginary part of the secondary vertical magnetic field of the model in figure 5.11 (dashed line), using the local refinement illustrated in figure 5.15 with the published results (solid line) of Pridmore et al.

real and imaginary parts occurs at large values of N (N= 15–20), and small values of c (c= 0.3–0.6), or when the largest amount of data has the most influence on the calculation of the spatial derivatives of **A**.

Finally, the problem of mesh truncation has been explored by other authors. A review of the techniques developed to overcome the difficulties of mesh truncation can be found in Chen and Konrad (1997).

CHAPTER VI

VALIDATION OF METHOD: TIME DOMAIN CSEM MODELING

Time domain, or transient, controlled-source EM model responses may be synthesized from frequency domain responses using a Fourier transform (Newman et al., 1986):

$$F(\omega) \underset{FT}{\Longrightarrow} f(t).$$

The response of a model to an instantaneous switch-on of source energy is described by the Fourier transform

$$f(t) = \frac{1}{2\pi} \int_{-\infty}^{\infty} \frac{F(\omega)}{i\omega} \exp(-i\omega t)\; d\omega \tag{6.1}$$

(Bracewell, 2000), where $F(\omega)$ is the response of the model to a sinusoidal source of energy of frequency ω. In terms of the CSEM problem, the electric and magnetic field response of a conductivity model to an instantaneous switch-on of current in a transmitter can be calculated from a suite of frequency domain responses. Time domain field data collection is performed using a rapid switch-off of transmitter current. Modeling the response of a model to a switch-off of transmitter current is achieved by subtracting the step-on response from the response of the model to an unchanging, or direct, current (DC), as illustrated schematically in figure 6.1.

Equation 6.1 can be simplified by considering that the time domain response has no

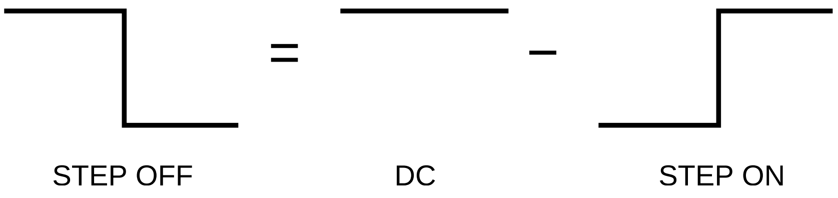

Fig. 6.1. The step-off response of the model is calculated by subtracting the step-on response from the the DC response.

imaginary component. Equation 6.1 is expanded into real and imaginary parts,

$$f(t) = \frac{1}{2\pi}\int_{-\infty}^{\infty}\left[-\frac{iF_{\Re}}{\omega} + \frac{F_{\Im}}{\omega}\right]\left[\cos(\omega t) - i\sin(\omega t)\right]\, d\omega, \tag{6.2}$$

where $F(\omega) = F_{\Re}(\omega) + iF_{\Im}(\omega)$. The imaginary parts are required to vanish,

$$\mathrm{Im}\{f(t)\} = \frac{1}{2\pi}\int_{-\infty}^{\infty}\left[-\frac{F_{\Re}}{\omega}\cos(\omega t) - \frac{F_{\Im}}{\omega}\sin(\omega t)\right]\, d\omega = 0, \tag{6.3}$$

leaving:

$$f(t) = \frac{1}{2\pi}\int_{-\infty}^{\infty}\left[-\frac{F_{\Re}}{\omega}\sin(\omega t) + \frac{F_{\Im}}{\omega}\cos(\omega t)\right]\, d\omega. \tag{6.4}$$

The time domain response is also causal, yielding no response before the transmitter switch-off, so that

$$f(-t) = 0 = \frac{1}{2\pi}\int_{-\infty}^{\infty}\left[\frac{F_{\Re}}{\omega}\sin(\omega t) + \frac{F_{\Im}}{\omega}\cos(\omega t)\right]\, d\omega. \tag{6.5}$$

This leads to the equality

$$\int_{-\infty}^{\infty}\frac{F_{\Re}}{\omega}\sin(\omega t)\, d\omega = -\int_{-\infty}^{\infty}\frac{F_{\Im}}{\omega}\cos(\omega t)\, d\omega, \tag{6.6}$$

allowing the further simplification of equation 6.4:

$$f(t) = -\frac{1}{\pi}\int_{-\infty}^{\infty}\frac{F_{\Re}}{\omega}\sin(\omega t)\, d\omega$$

OR

$$f(t) = \frac{1}{\pi}\int_{-\infty}^{\infty}\frac{F_{\Im}}{\omega}\cos(\omega t)\, d\omega \tag{6.7}$$

It may also be shown that $F(-\omega) = F^*(\omega)$, or that

$$\mathrm{Re}\{F(-\omega)\} + i\mathrm{Im}\{F(-\omega)\} = \mathrm{Re}\{F(\omega)\} - i\mathrm{Im}\{F(\omega)\},$$

implying that the real part of $F(\omega)$ is even, and the imaginary part is odd. Thus, equation 6.7 becomes:

$$f(t) = -\frac{2}{\pi}\int_0^\infty \frac{F_\Re}{\omega}\sin(\omega t)\; d\omega$$

$$\text{OR}$$

$$f(t) = \frac{2}{\pi}\int_0^\infty \frac{F_\Im}{\omega}\cos(\omega t)\; d\omega, \tag{6.8}$$

acknowledging that $\sin(\omega t)$ is an odd function of ω, $\cos(\omega t)$ is even, and $1/\omega$ is odd.

The cosine and sine transforms required in equation 6.8 are accomplished with the drop-in subroutine `COSAUT`, written by Alan Chave. The frequency domain EM fields are calculated using the finite element and MLSI algorithms at a series of log spaced frequencies. The discrete frequency domain responses are then splined using the cubic spline subroutines `SPLINE` and `SPLINT` from *Numerical Recipes in FORTRAN* (Press et al., 1992). The range of frequencies calculated is determined by the subroutine `COSAUT`, dependent upon the range of time over which the time domain response is to be calculated. The number of frequencies calculated per decade is determined by plotting the splined frequency spectrum and insuring (by eye) that there are no aberrant oscillations or Gibb's phenomena present.

It should also be noted that the runtimes associated with the linear solver `ILUSPARSE` are prohibitively expensive for the calculation of the multiple frequency domain responses required for the inverse Fourier transform in equation 6.1. Therefore, the quasi-minimal residual algorithm, described by Freund, et al. (1992), is implemented. This procedure has been successfully used in CSEM modeling by Newman and Alumbaugh (1995), and is not detailed here. Incorporation of this procedure into the finite element algorithm results in a dramatic decrease in CPU time per frequency domain calculation.

Three Dimensional EM Modeling

The time domain CSEM responses of several simple, fully three-dimensional conductivity models are presented here without quantitative verification against analytical or

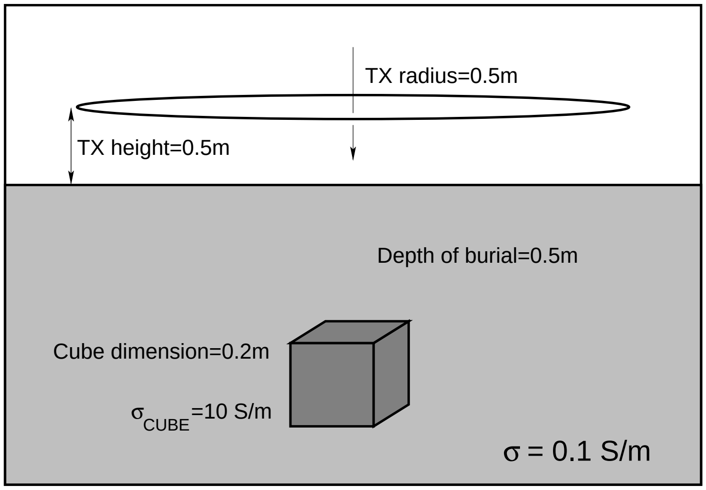

Fig. 6.2. A cube buried in a conductive halfspace.

published numerical modeling results. However, the calculated electric and magnetic fields are monitored for features characteristic of the conductivity model and the transmitter and receiver geometry.

Buried Cube Model—A 0.2 m cube is buried at 0.5 m below the surface of a conductive halfspace. The cube is assigned a conductivity of 10 S/m, and the halfspace a conductivity of 0.1 S/m. The transmitter is located directly above the cube at a height of 0.5 m above the surface of the halfspace, and has a radius of 0.5 m, and a current (before shut-off) of 6 A. The model is illustrated in figure 6.2.

The modeling results are presented in figures 6.3–6.5 for a profile from $x = -2$ meters to $x = +2$ meters, where $y = 0$ m, and $z = -0.5$ m. In each figure, both the total and secondary magnetic fields are provided, for a selected sample of times instances. The real and imaginary splined spectral secondary responses at $x = y = 0$ m, and $z = -0.5$ m are displayed in figure 6.6.

Several observations may be made regarding the modeling results. The total field is dominated by a magnetic field that indicates a secondary current that is an image of the transmitter current, that diffuses down and outward into the medium. This is the expected response of a conductive halfspace (Nabighian, 1979). Also as expected, the halfspace primary conductivity model contributes nothing to the y-component of the magnetic field

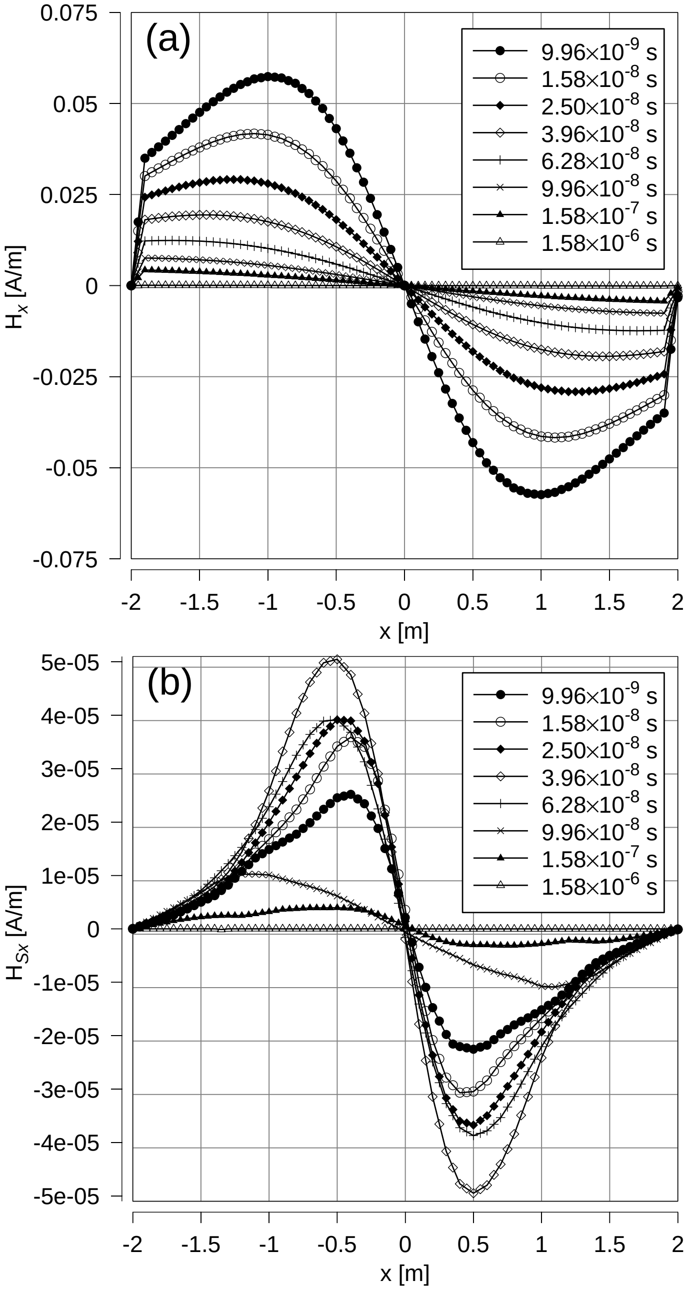

Fig. 6.3. Total (a) and secondary (b) x-directed time domain magnetic field for the cube model in figure 6.2, calculated along a profile from $-2 \leq x \leq 2$ m, where $y = 0$ m and $z = -0.5$ m.

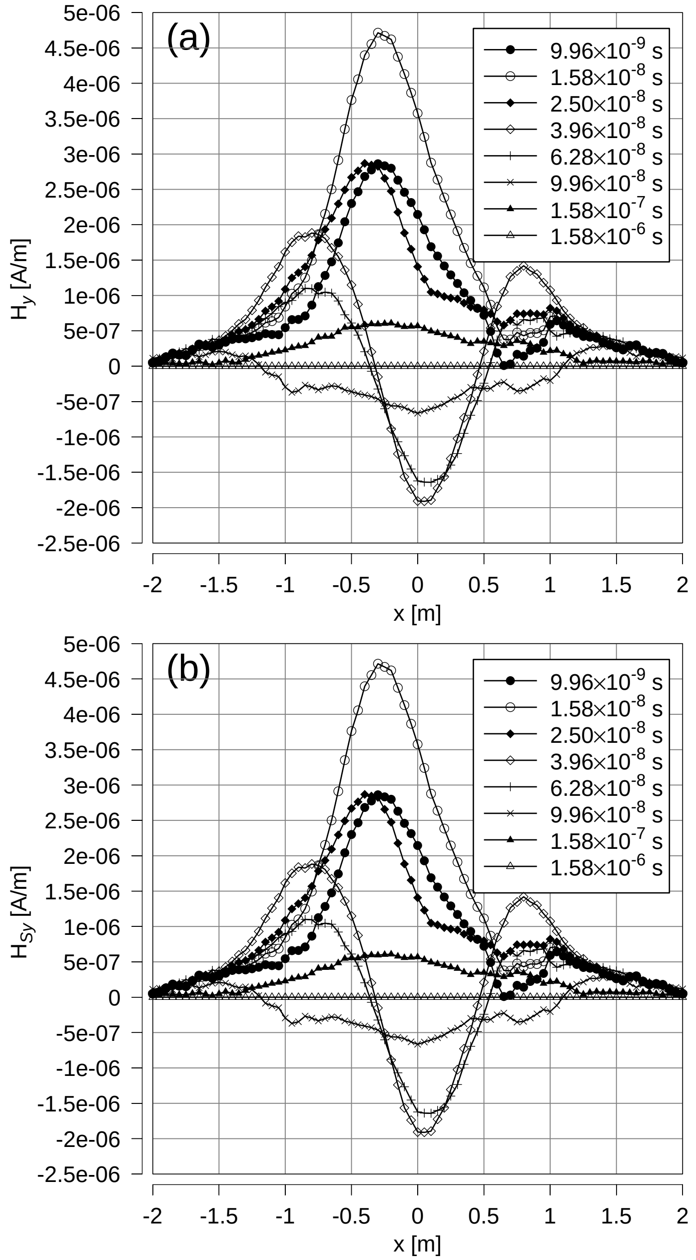

Fig. 6.4. Total (a) and secondary (b) y-directed time domain magnetic field for the cube model in figure 6.2, calculated along a profile from $-2 \leq x \leq 2$ m, where $y = 0$ m and $z = -0.5$ m.

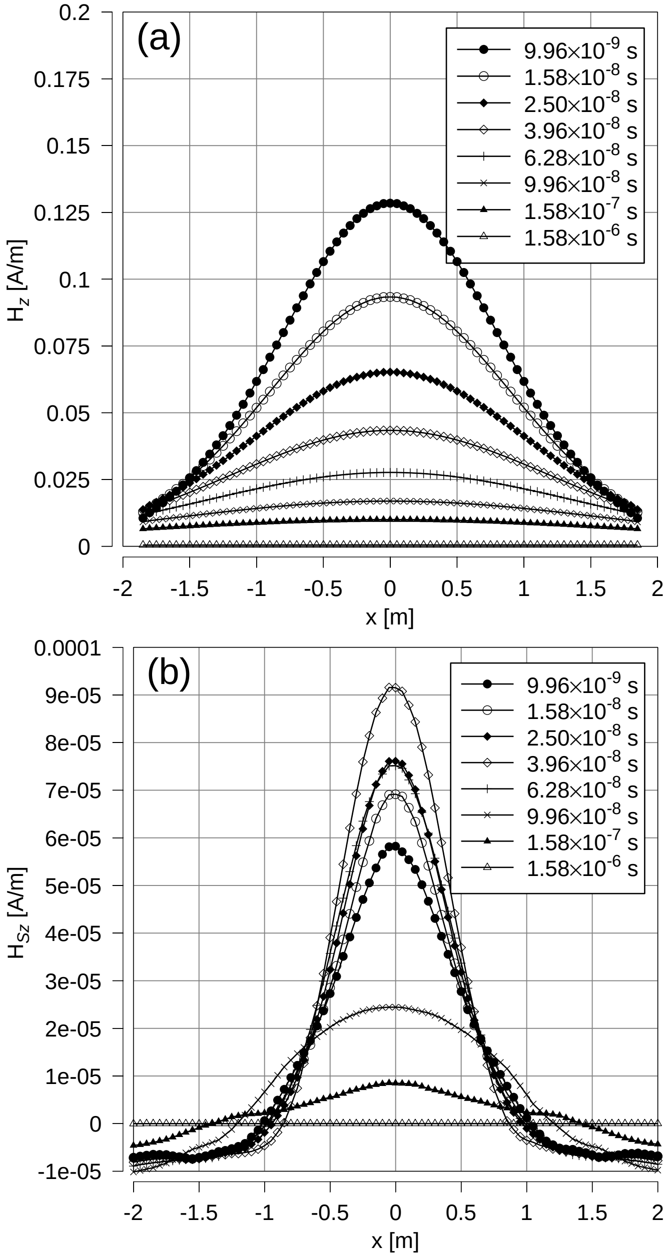

Fig. 6.5. Total (a) and secondary (b) z-directed time domain magnetic field for the cube model in figure 6.2, calculated along a profile from $-2 \leq x \leq 2$ m, where $y = 0$ m and $z = -0.5$ m.

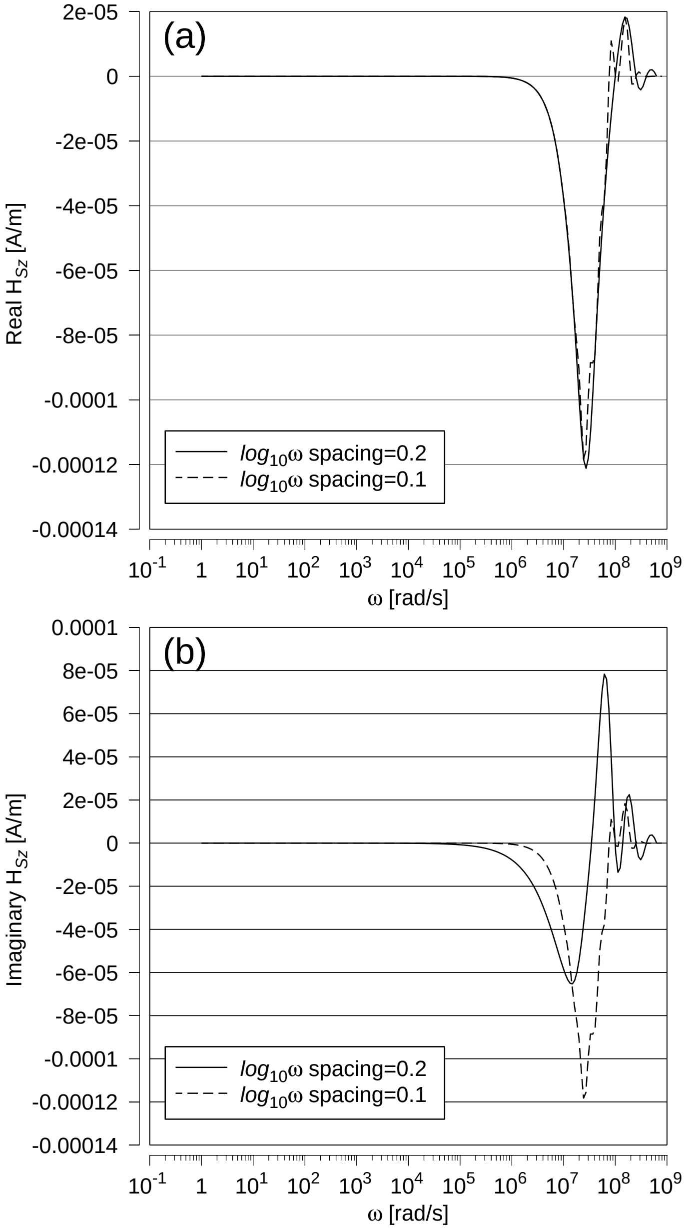

Fig. 6.6. The real (a) and imaginary (b) splined spectral response of the cube model in figure 6.2 at $x = y = 0$ m, and $z = -0.5$ m. Two different frequency sampling densities are displayed.

for $y = 0$ meters. It may also be noted that, by and large, the secondary response indicates that the current induced in the cube also forms a vertical dipole. The presence of a y component in the secondary response can be attributed to several factors, including the geometry of the cube, and the interaction of the cube with the conductive host (galvanic current flow).

The splined spectral responses exhibit distinct Gibb's phenomena at roughly $f = 5 \times 10^7$ Hz, and measures may need to be taken to correct this. Doubling the number of frequencies used to create the splined response (see figure 6.6 decreases the magnitude of the Gibb's oscillations, but has little effect on the calculated magnetic fields. There are also indicators that the finite element mesh may warrant improvement, including distinctive shoulders in the H_{Sx} response at $x = \pm 1$ m, and the asymmetry of the H_{Sy} response.

The response of the cube model for the transmitter and receiver setup illustrated in figure 6.7 is also presented here. This transmitter and receiver layout is identical to a prototype currently being constructed as part of an ongoing project to develop a device capable of detecting and discriminating unexploded ordnance (UXO). Receivers 6 and 7 are sensitive to the x-component of the magnetic field, and the total and secondary fields measured by these fields are displayed in figure 6.8. Similarly, receivers 8 and 9 are designed to measure the y-component of the magnetic field, as shown in figure 6.9. The remainder of the receivers measure the vertical component of the magnetic field, plotted in figure 6.10.

The calculated responses, total and secondary, exhibit the expected geometry. Equal and opposite responses are found for opposed receivers in both the secondary and total responses, and the receivers sensitive to the x and y components of the magnetic field show the same response, again indicating that the secondary currents in the cube are acting as a vertically directed dipole. The inflection in the vertical magnetic field at receivers 2-5 shows the induced eddy currents decaying into the cube due to ohmic losses (West and Macnae, 1991).

Quarter Space Model— A quarter space of conductivity $\sigma = 0.3$ S/m is placed in a halfspace of conductivity 0.1 S/m, extending from $z = 0$ m to $z = +\infty$, from $x = -0.2$ m

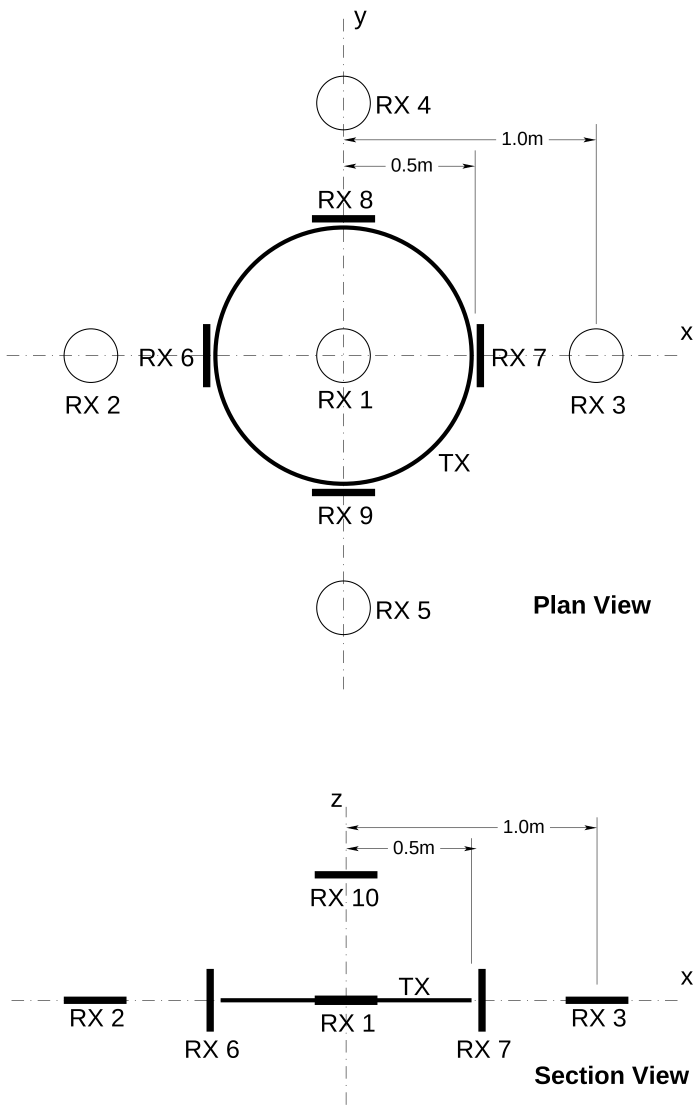

Fig. 6.7. Transmitter and receiver specifications modeled after the prototype UXO detection and discrimination device designed at Texas A&M University.

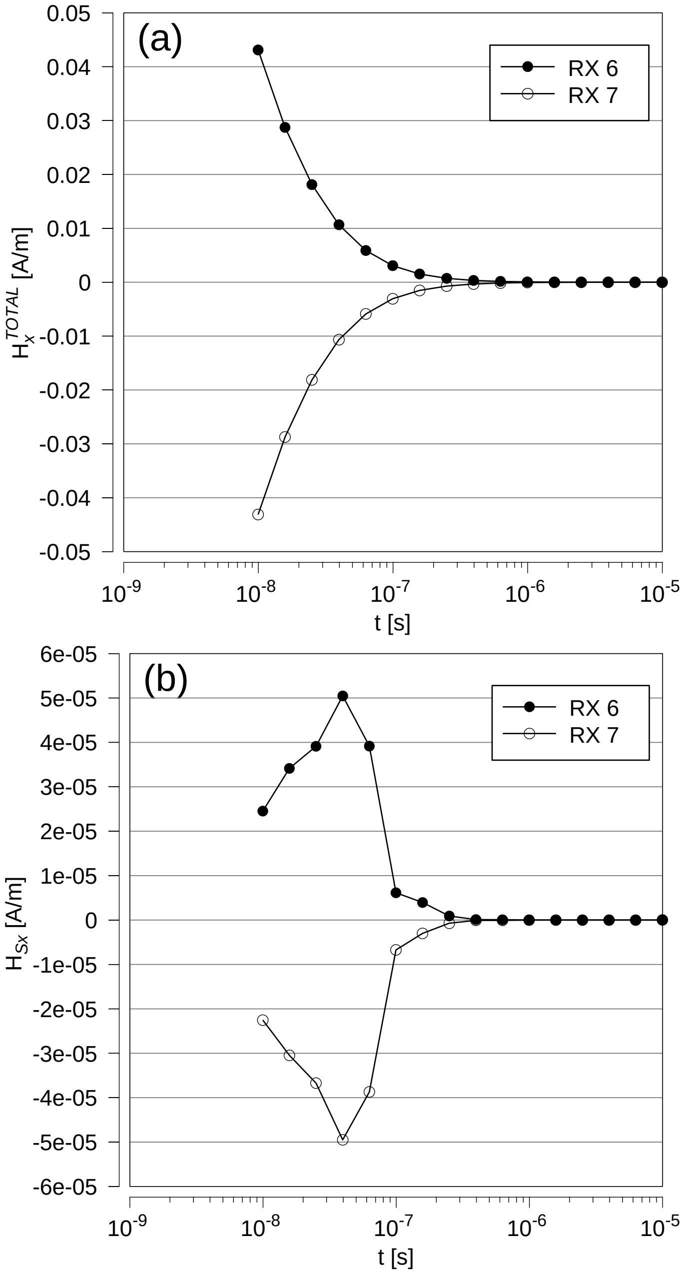

Fig. 6.8. Total (a) and secondary (b) x-directed time domain magnetic field for the cube model in figure 6.2, calculated at receiver locations 6 and 7 in figure 6.7.

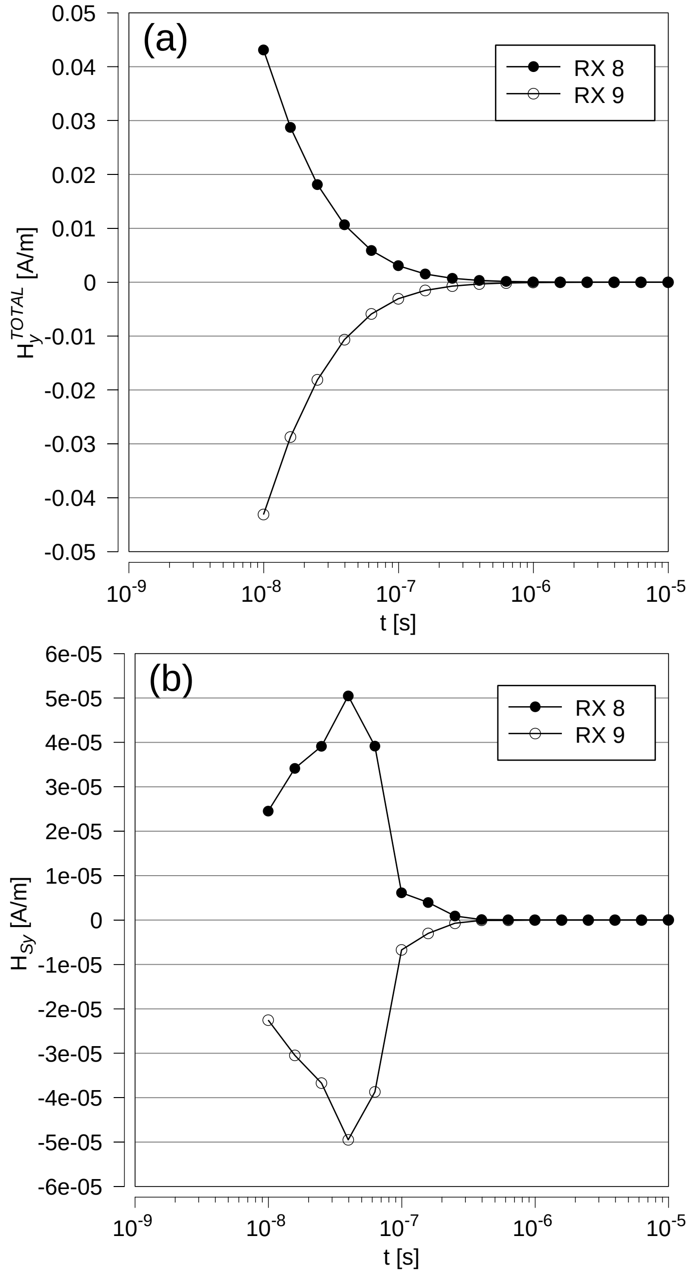

Fig. 6.9. Total (a) and secondary (b) y-directed time domain magnetic field for the cube model in figure 6.2, calculated at receiver locations 8 and 9 in figure 6.7.

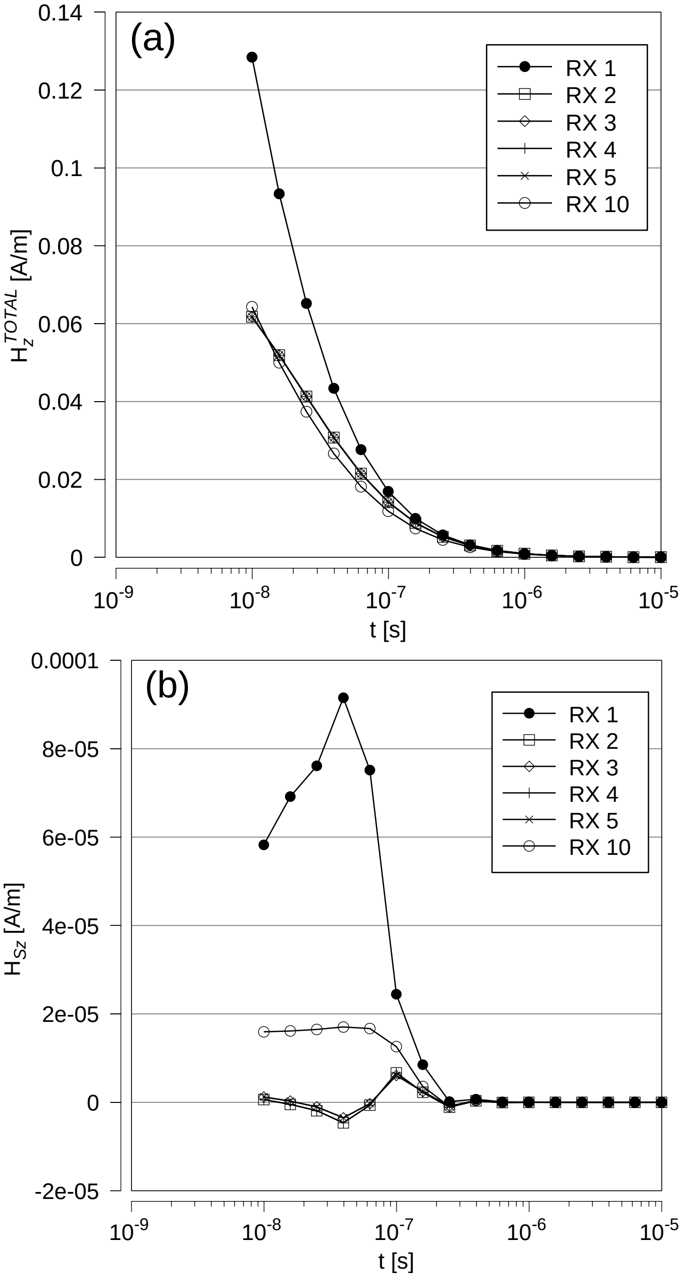

Fig. 6.10. Total (a) and secondary (b) z-directed time domain magnetic field for the cube model in figure 6.2, calculated at receiver locations 1, 2, 3, 4, 5, and 10 in figure 6.7.

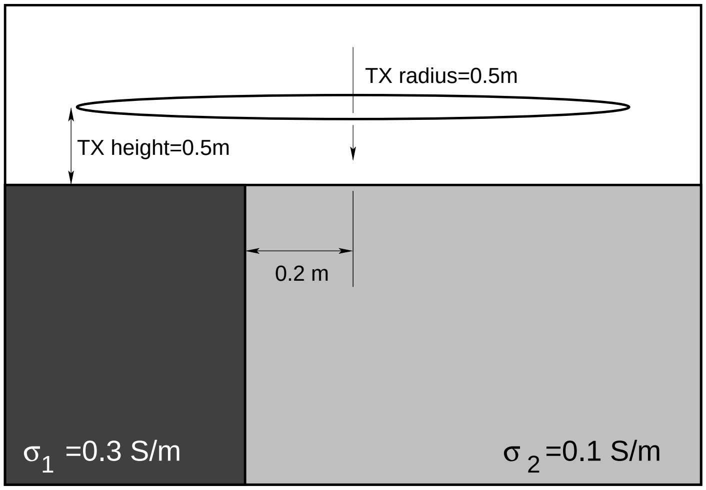

Fig. 6.11. A quarter space conductivity model.

to $x = -\infty$, and from $y = -\infty$ to $y = +\infty$, as illustrated in figure 6.11. The transmitter specifications remain unchanged from the cube model above. The receivers are specified according to the UXO detection device model in figure 6.7. The results are displayed in figures 6.12—6.14.

The finite element algorithm again appears to perform as expected. The secondary and total y-components exhibit excellent symmetry, imparted by the symmetry of the model in the y direction. The remaining receivers show a secondary field that falls off with distance from the quarter space. By and large, the total field is dominated by the response of the image current in the halfspace, as before. The secondary field of the quarter space is two to three orders of magnitudes larger than the secondary field of the cube, despite the fact that the conductivity of the quarter space is 1/33rd that of the cube. A greater amount of primary magnetic field fluxes through the larger quarter space, generating a much larger EMF therein upon shut-off of the transmitter current.

Cube and Quarter Space Model— As another check of the fully three-dimensional time domain finite element code, the previous two models are combined, as illustrated in figure 6.15. The results are presented in figures 6.16—6.18.

Despite the fact that the secondary response of the quarter space is much stronger than the response of the cube, the cube clearly has an effect on the magnetic field. The effect

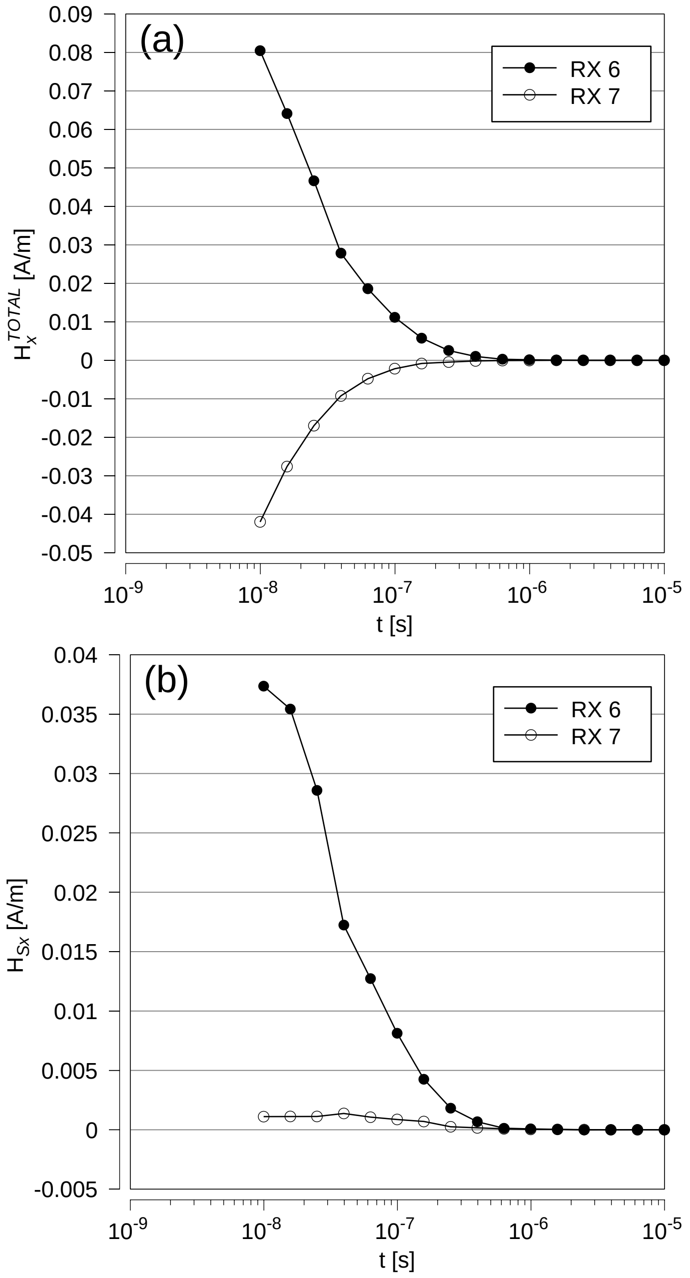

Fig. 6.12. Total (a) and secondary (b) x-directed time domain magnetic field for the quarter space model in figure 6.11, calculated at receiver locations 6 and 7 in figure 6.7.

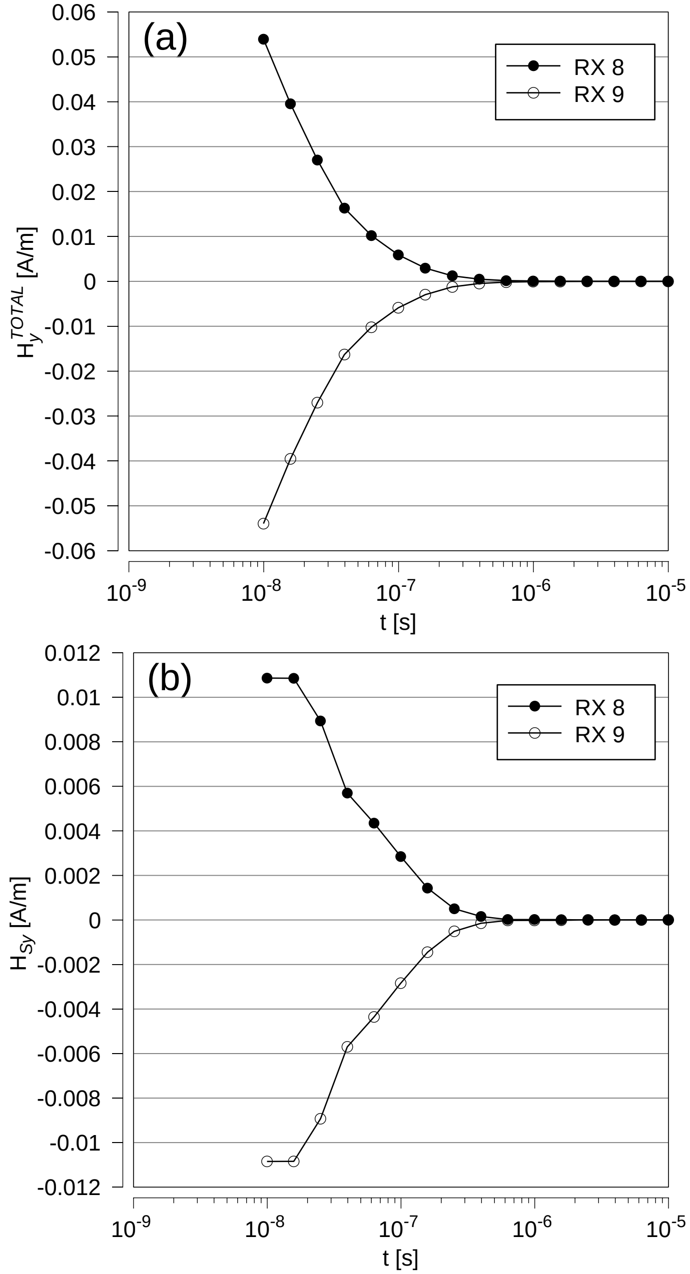

Fig. 6.13. Total (a) and secondary (b) y-directed time domain magnetic field for the quarter space model in figure 6.11, calculated at receiver locations 8 and 9 in figure 6.7.

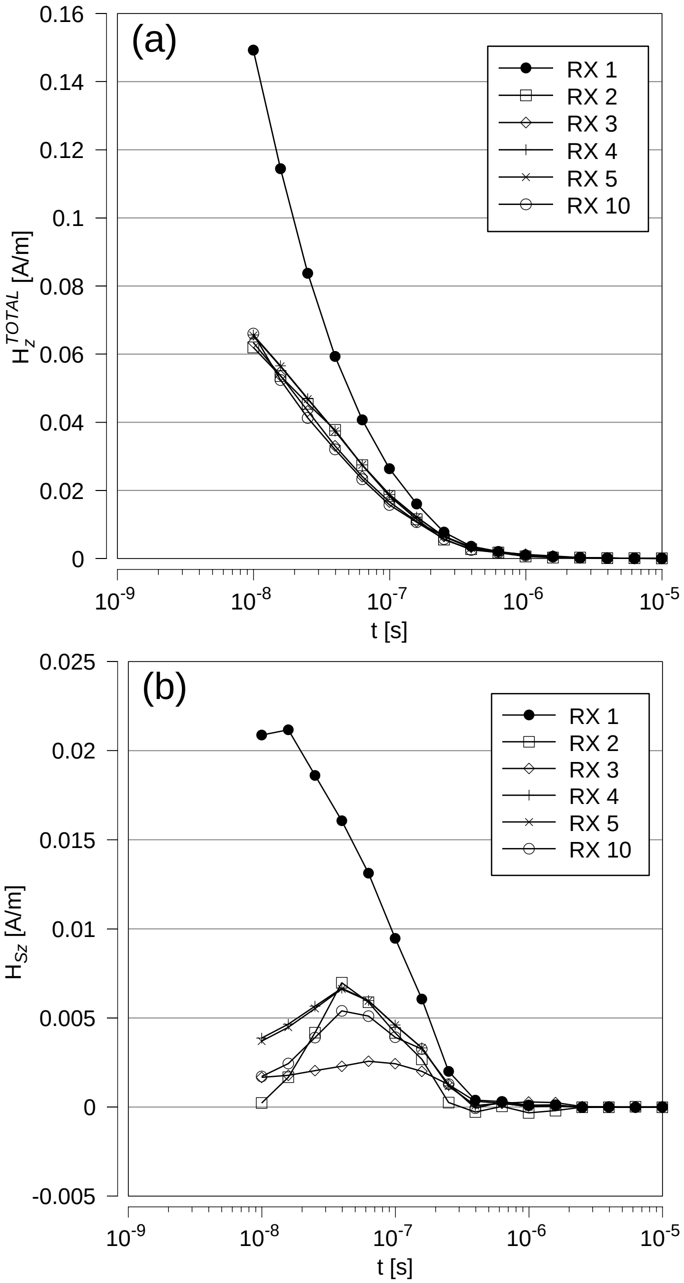

Fig. 6.14. Total (a) and secondary (b) z-directed time domain magnetic field for the quarter space model in figure 6.11, calculated at receiver locations 1, 2, 3, 4, 5, and 10 in figure 6.7.

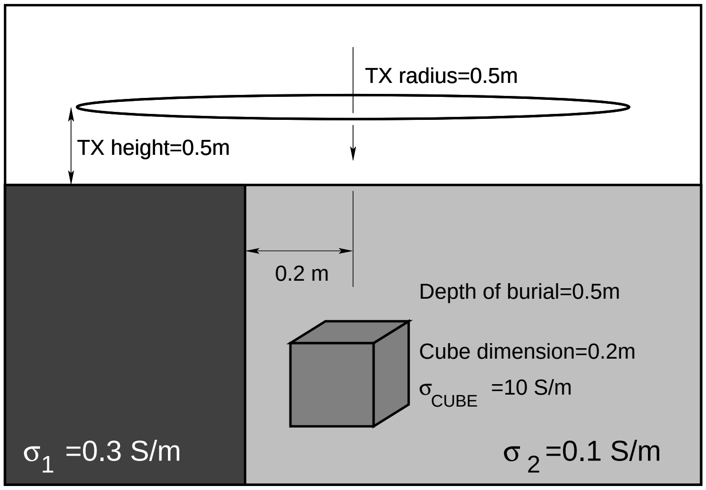

Fig. 6.15. A combination of the cube and quarter space conductivity models.

is more pronounced than it would be if responses the cube and the quarter space were modeled separately and added together, because the two secondary targets are interacting via the process of mutual induction and galvanic current flow through the conductive host.

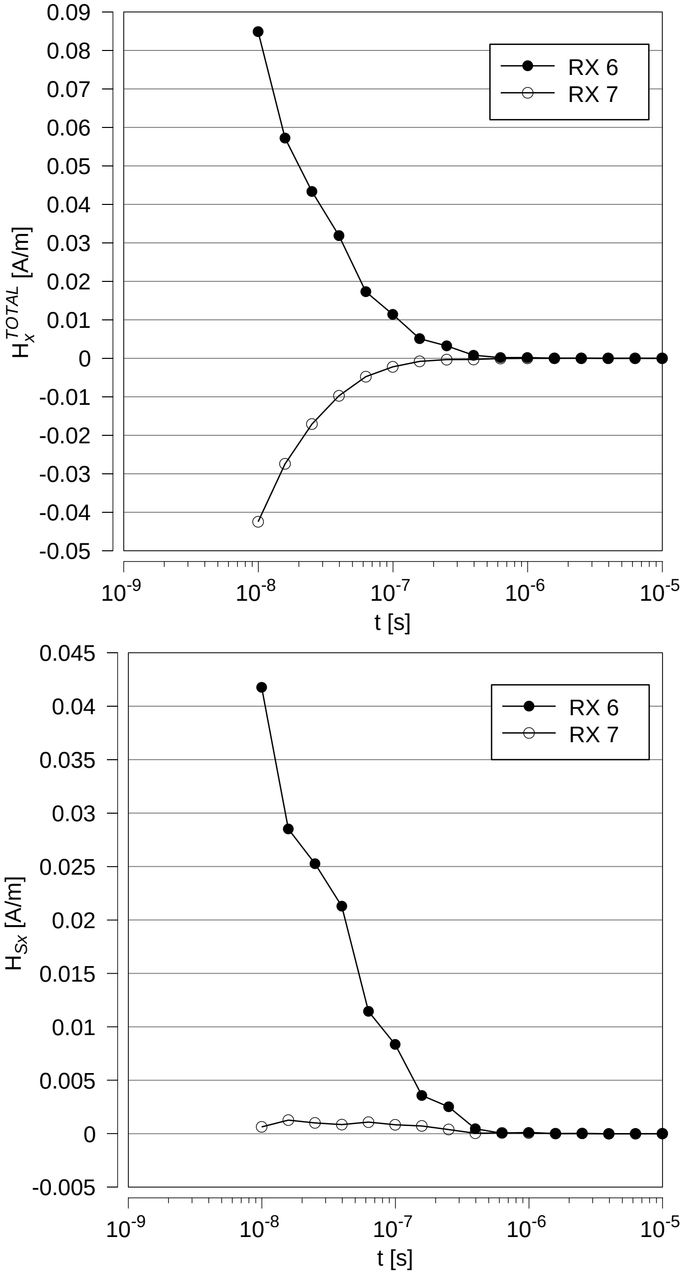

Fig. 6.16. Total (a) and secondary (b) x-directed time domain magnetic field for the quarter space + cube model in figure 6.15, calculated at receiver locations 6 and 7 in figure 6.7.

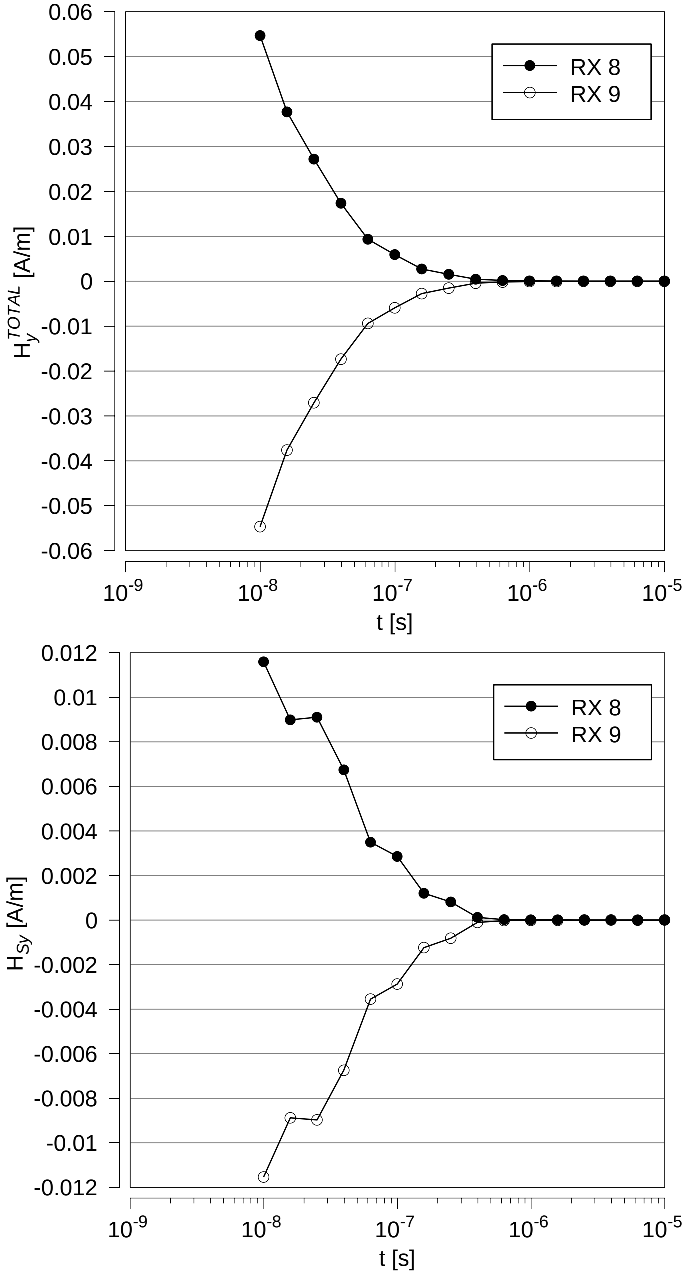

Fig. 6.17. Total (a) and secondary (b) y-directed time domain magnetic field for the quarter space + cube model in figure 6.15, calculated at receiver locations 8 and 9 in figure 6.7.

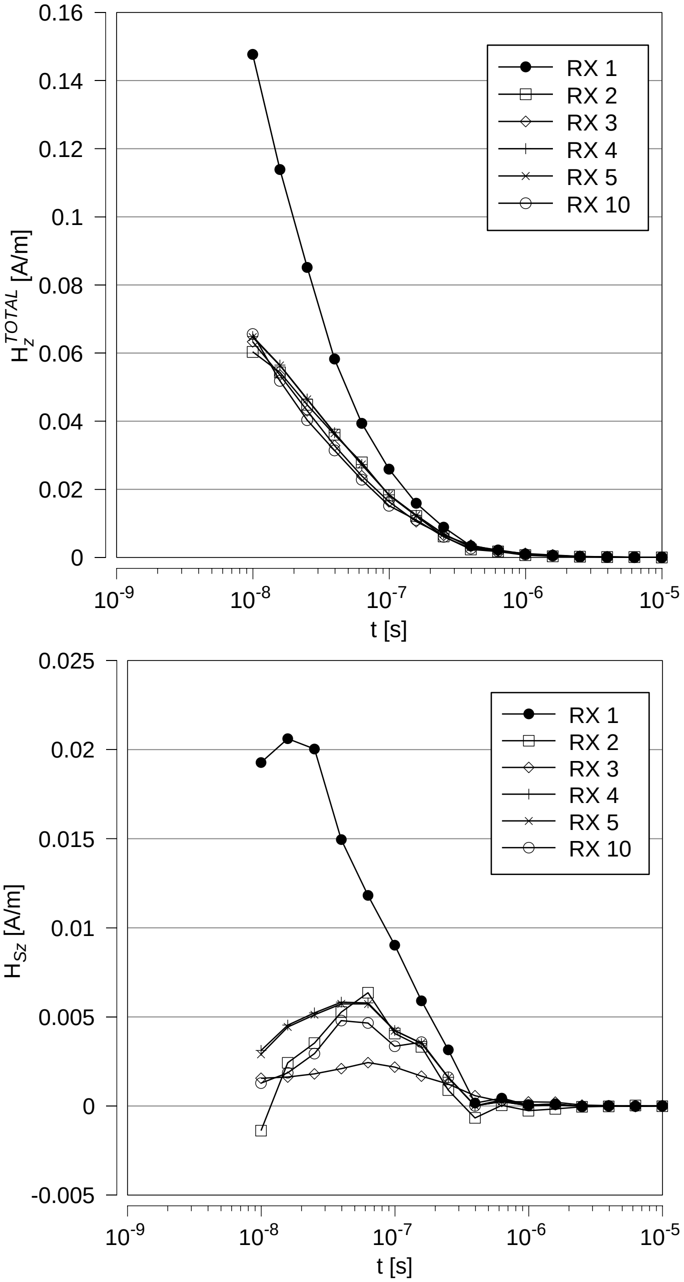

Fig. 6.18. Total (a) and secondary (b) z-directed time domain magnetic field for the quarter space + cube model in figure 6.15, calculated at receiver locations 1, 2, 3, 4, 5, and 10 in figure 6.7.

CHAPTER VII

MUTUAL INTERACTION BETWEEN TWO BURIED PLATES

The CSEM response of multiple conductive targets is determined to some degree by the mutual interaction of the eddy currents induced within the targets. For targets in free space, this interaction is limited to mutual induction wherein each pair of targets is linked by the magnetic flux of the current vortices induced in the targets by the transmitter. In the presence of a conductive host, the charge accumulation at material interfaces can dissipate, and cause an additional current flow between the plates.

The effect of the mutual interaction of multiple targets on the controlled-source response has been only lightly represented in the literature, and the extant publications deal largely with the mutual induction between the buried targets, or the targets and the CSEM transmitter and receiver, ignoring the effect of a conductive host medium. For example, calculation of the mutual induction of conductive wire loops over a homogeneous earth are found in Wait (1954), Wait (1955), and (1956). The effect of mutual induction on the CSEM response of closely spaced steeply dipping tabular conductors in a resistive host is explored in Duckworth and Clement (2001).

The concept of mutual induction is easiest to illustrate by considering two current carrying loops of wire (figure 7.1). According to Ampere's law, equation 2.4, a steady current I_1 flowing in loop 1 will create a magnetic field $\mathbf{H}_1$ curling around the wire. If the two wire loops are positioned as they are in figure 7.1, then a portion of the magnetic field $\mathbf{H}_1$ will pass though loop 2. The magnetic flux B_1 is described by the Biot-Savart law,

$$\mathbf{B}_1 = \frac{\mu_0}{4\pi} I_1 \oint \frac{d\mathbf{l}_1 \times \hat{\mathbf{R}}}{\mathrm{R}^2}, \tag{7.1}$$

and it is therefore proportional to the current I_1. The flux through the second loop is due entirely to the magnetic field (or magnetic flux) of the first loop, as described by

$$\Phi_2 = \int \mathbf{B}_1 \cdot d\mathbf{a}_2 \tag{7.2}$$

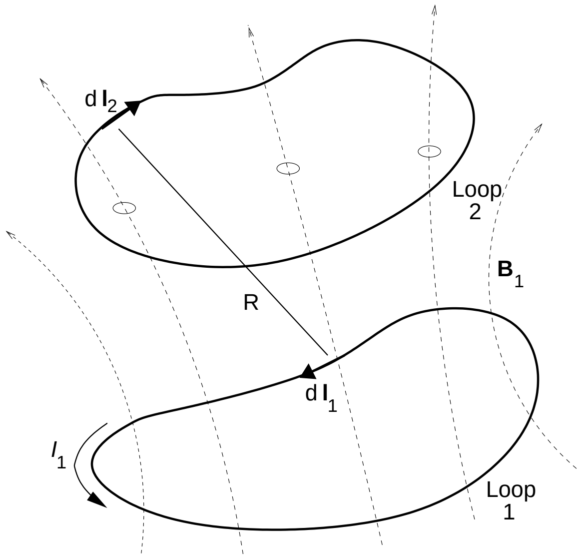

Fig. 7.1. Mutual induction illustrated with two loops of wire. Modified from Griffiths (1999).

where $d\mathbf{a}_2$ is a portion of the area encompassed by loop 2. Because the magnetic flux $\mathbf{B}_1$ is proportional to the current in loop 1, I_1, the flux through loop 2 is also proportional to I_1:

$$\Phi_2 = M_{21} I_1. \tag{7.3}$$

The constant of proportionality M_{21} is called the mutual inductance. (Griffiths, 1999)

A steady flux of magnetic field through loop 2 will have no affect on the current (or lack of current) flowing therein. However, if the current (and thus, the magnetic field) of loop 1 is allowed to vary with time, an EMF will be induced in loop 2 according to Faraday's law:

$$\epsilon_2 = -\frac{d\Phi_2}{dt} = -M_{21}\frac{dI_1}{dt}, \tag{7.4}$$

assuming the current in loop 1 varies slowly enough for the quasistatic approximation to hold. The EMF will either impede or enforce the current flowing in loop 2, depending on the direction of the original current (if any), I_2.

Several conclusions can be drawn that are useful for interpretation of CSEM responses. It can be shown that the mutual induction M is a purely geometric quantity, dependent upon the sizes, shapes, and relative positions of loop 1 and 2. Also, the mutual induction is symmetric. That is, $M_{21} = M_{12}$. The presence of additional targets warrants the introduction of additional mutual inductions terms, describing the interaction between each current loop.

A conductor in free space may be subjected to a time-varying magnetic field. According to Maxwell's equations, a secondary current vortex will be induced in the conductor. If a second conductor is placed in the same primary magnetic field, an additional current vortex will be induced in that conductor. The current vorticies will interact in a fashion similar to the filamentary current loops described above. The interaction of the two conductors will likewise be determined by the geometry of the conductors, including the relative conductor sizes, shapes, orientations, and positions. The problem is complicated because the currents are not finite filaments, but rather diffuse current densities, the geometry and strength of which are determined by the target conductivity and geometry relative to the transmitter.

The mutual interaction of multiple conductors is further obfuscated by the introduction of a conductive host medium. A current density is induced in the host medium that interacts via mutual induction with the currents in the target conductors. Additionally, a conductivity contrast between the target and the host gives rise to an accumulation on the interface (West and Macnae, 1991). If only one target is present, this charge accumulation creates a secondary current flow, dubbed a galvanic current, wherein the charges flow through the host in attempt to neutralize the buildup. In the presence of a second conductor, however, charges may also flow through the host from one conductor to another, altering the galvanic current flow, and the subsequent secondary EM fields generated thereby. Charge accumulation, and therefore galvanic current flow and mutual interaction are determined by target conductivity and geometry of the conductor relative to the eddy currents flowing in the host medium. In turn the magnitude of interaction between the conductors is affected by the relative positioning and orientation of the multiple buried conductors.

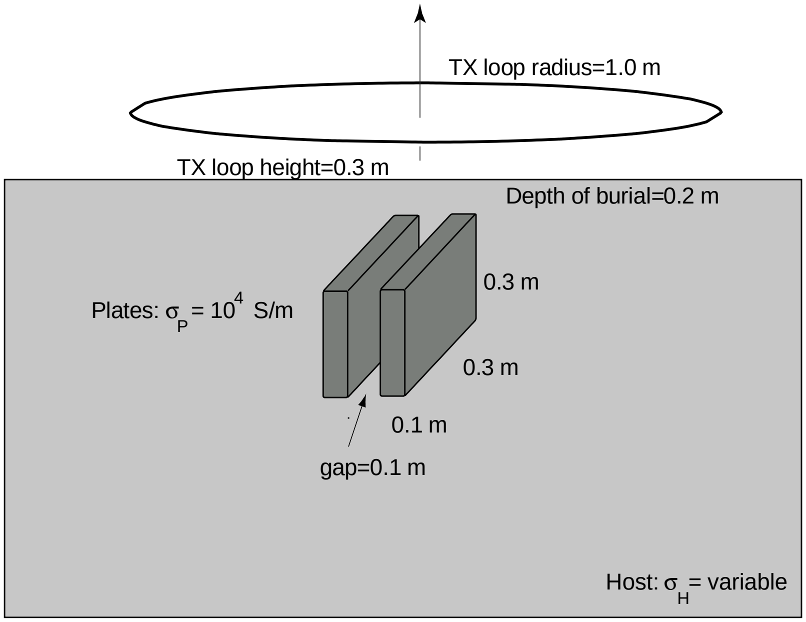

Fig. 7.2. The vertical-vertical plate (VVP) model.

The “UXO” Models

Collectively, mutual induction and interaction via current flow in the host medium are dubbed “mutual coupling”. It is the goal of this study to quantify and interpret mutual coupling for three different conductivity models. The models are intended to very roughly mimic the properties of buried unexploded ordnance, or UXO, in that the plates represent localized, collocated, metallic targets. As such, the conductors are assigned a very high conductivity, as most UXO are metallic, and the host medium is assigned a conductivity similar to common soil materials. The models will be hereafter referred to as the vertical-vertical plate model, or VVP, illustrated in figure 7.2, the horizontal-vertical plate model, or HVP, illustrated in figure 7.3, and the horizontal-horizontal plate model, or HHP, illustrated in figure 7.4.

The orientation of the target conductors in the VVP model is intended to maximize mutual coupling, as shown in figure 7.5. Vortex currents generated within the conductor flow in a direction determined by the conductor geometry. Any component of current flow normal to the target boundary is neutralized by charge buildup arising from the large

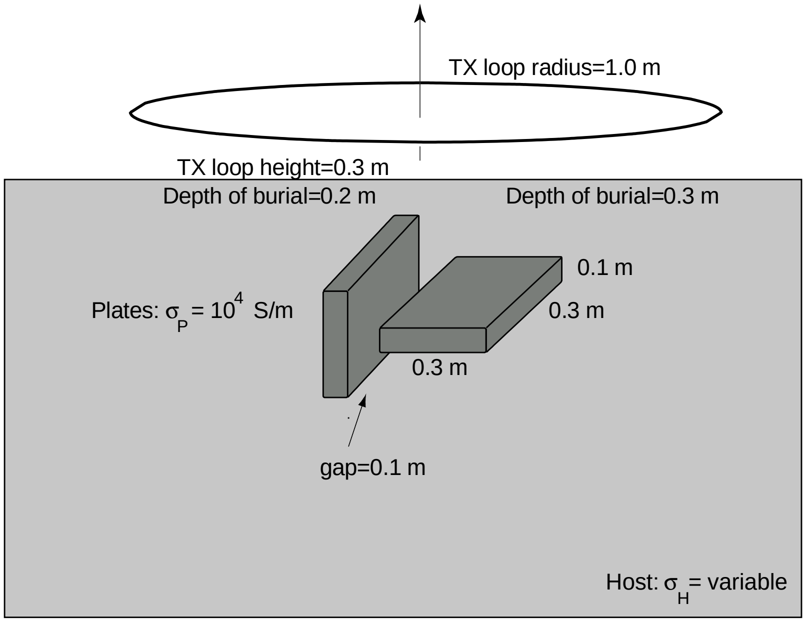

Fig. 7.3. The horizontal-vertical plate (HVP) model.

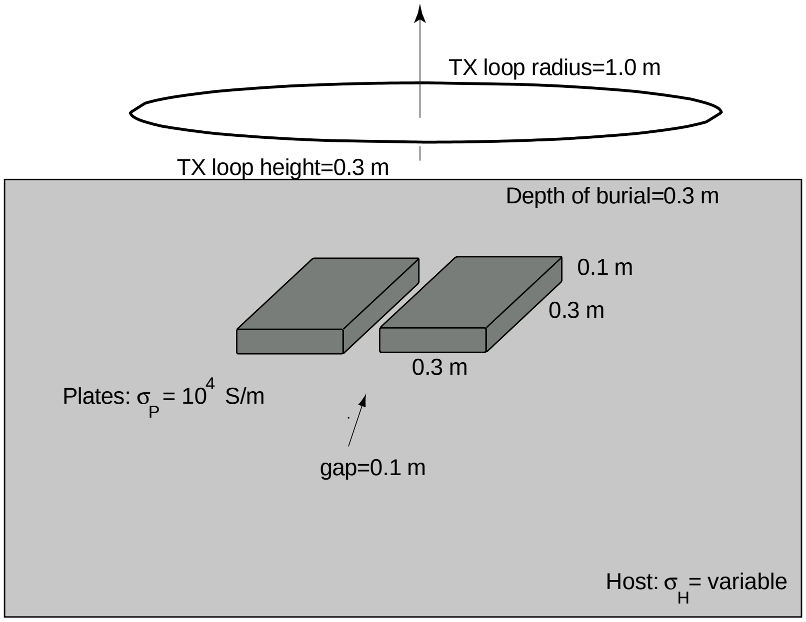

Fig. 7.4. The horizontal-horizontal plate (HHP) model.

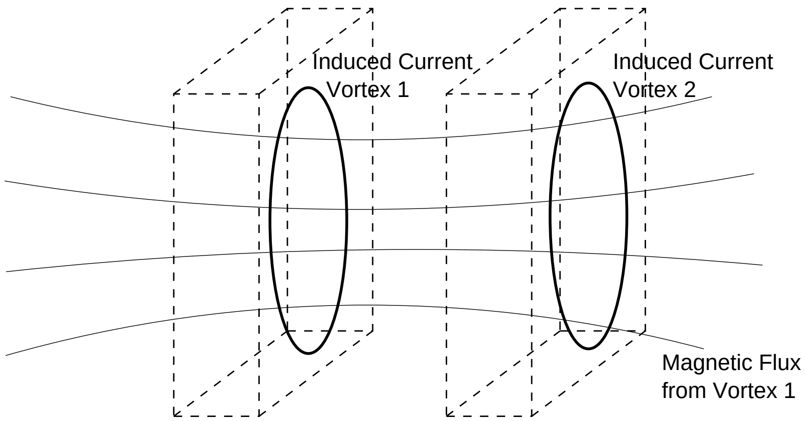

"Well−Coupled" Model (VVP)

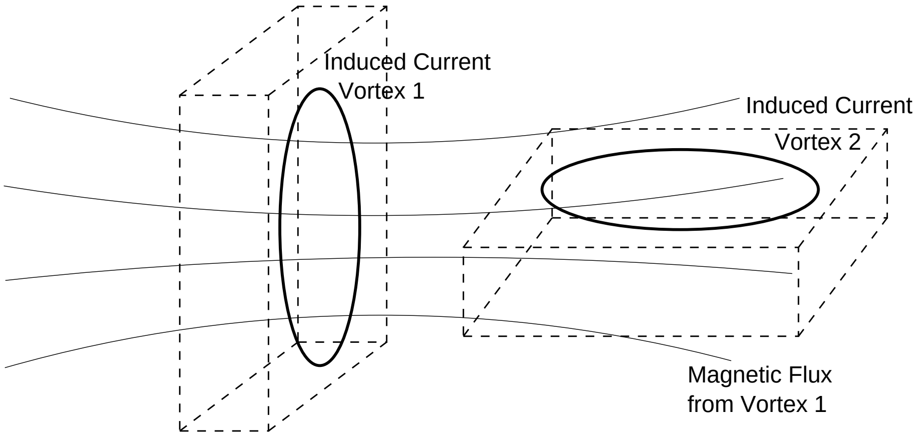

"Null−Coupled" Model (HVP)

Fig. 7.5. A well-coupled and null-coupled model configuration. The well-coupled model is intended to maximize magnetic flux linkage amongst the targets, while the null-coupled model is intended to minimize flux linkage.

contrast in material properties at the interface (West and Macnae, 1991). The thickness of the plates relative to model skin depth, and the dipole nature of the primary magnetic field render figure 7.5 an oversimplification (i.e. the current vorticies will not in reality be oriented perfectly horizontal). However, the targets in the VVP model should be well flux-linked.

Alternatively, the HVP model is designed to minimize mutual coupling. The horizontal plate resides in the cusp of the secondary magnetic field generated by the vertical plate, minimizing the flux passing through the horizontal eddy current. However, flux from the horizontal eddy current will continue to flux though the vertical plate, albeit at a lower magnitude than the VVP model. The HHP model should fall somewhere in between, as the magnetic field of each plate fluxes through the other, to a lesser degree than the flux experienced by the plates in the VVP model.

The Mutual Coupling Factor, M

In order to contrast the effect of mutual coupling on the magnetic field of the UXO models, the effect must be quantified. In the absence of mutual coupling, the magnetic field of the full model is equal to the sum of the magnetic field of each target modeled separately. If the total magnetic field is considered, the magnetic field of the full model is equivalent to sum of the secondary magnetic field of each target modeled separately plus the primary field. The effect of mutual coupling is then the difference between the summed responses of each target modeled separately, and the complete model in which all targets are present. The mutual coupling factor, M is therefore introduced:

$$\mathbf{M}_S(\mathbf{r}) \equiv |\mathbf{H}_S^C(\mathbf{r}) - \sum_{i=1}^{N_T} \mathbf{H}_S^i(\mathbf{r})| \tag{7.5}$$

$$\mathbf{M}_T(\mathbf{r}) \equiv |\mathbf{H}_T^C(\mathbf{r}) - [\mathbf{H}_P(\mathbf{r}) + \sum_{i=1}^{N_T} \mathbf{H}_S^i(\mathbf{r})]|, \tag{7.6}$$

where $\mathbf{H}^C$ is the magnetic field of the complete model representing all conductive targets, and $\mathbf{H}^i$ is the magnetic field of the i-th target modeled in isolation. The subscripts P, S, and T indicate primary, secondary, and total fields, respectively.

The effect of the variation of host conductivity and transmitter frequency is studied for each of the UXO model configurations. Two host conductivities, 0.01 S/m and 0.3 S/m, are initially chosen that bracket the range of real-world values for typical soils and alluvium (Palacky, 1987). The imaginary part of the total magnetic field at four frequencies (30 Hz, 300 Hz, 3 kHz, and 30 kHz) is given in figures 7.6, 7.7, and 7.8. Both the magnetic field of the complete model and the sum of the responses of the individual targets are shown for comparison.

Clearly, the conductivity of the host is an important contributor to the overall CSEM response of buried metal targets, despite the large conductivity contrast between the host and the targets. At all four frequencies, the response for $\sigma_H = 0.03$ S/m is distinct from the response at $\sigma_H = 0.01$ S/m. In this case, therefore, modeling the response of the plates using a method that assumes the targets are suspended in free space (Huang and Won, 2003; Geng et al., 1999; Shubitdze and O'Neill, 2002, e.g.) would produce misleading results.

At low frequencies near the resistive limit (that is, the limit at which frequency, and thus $\partial\mathbf{B}/\partial t$ is low enough that it cannot overcome the resistance of the target to current flow), the CSEM response of the complete model is nearly indistinguishable from the summed response of the individual plates, indicating that there is very little mutual coupling between the plates (figures 7.6*a*—7.8*a*). Nevertheless, it should also be noted that the magnitude of the response is quite low. In an idealized model with a perfectly homogeneous host, this presents little difficulty. However, field studies have indicated (Benavides and Everett, 2003) that, as the host becomes increasingly variegated, background noise generated by geological heterogeneities (Everett and Weiss, 2002) increase, and the signals characteristic of the plates become very difficult to identify.

The amplitude of the CSEM response increases with frequency, and at 3 kHz, the effect of mutual coupling becomes quite significant (figures 7.6*c*—7.8*c*). At 30 kHz, the difference between the full model response and the summed plate response (figures 7.6*d*—7.8*d*) is

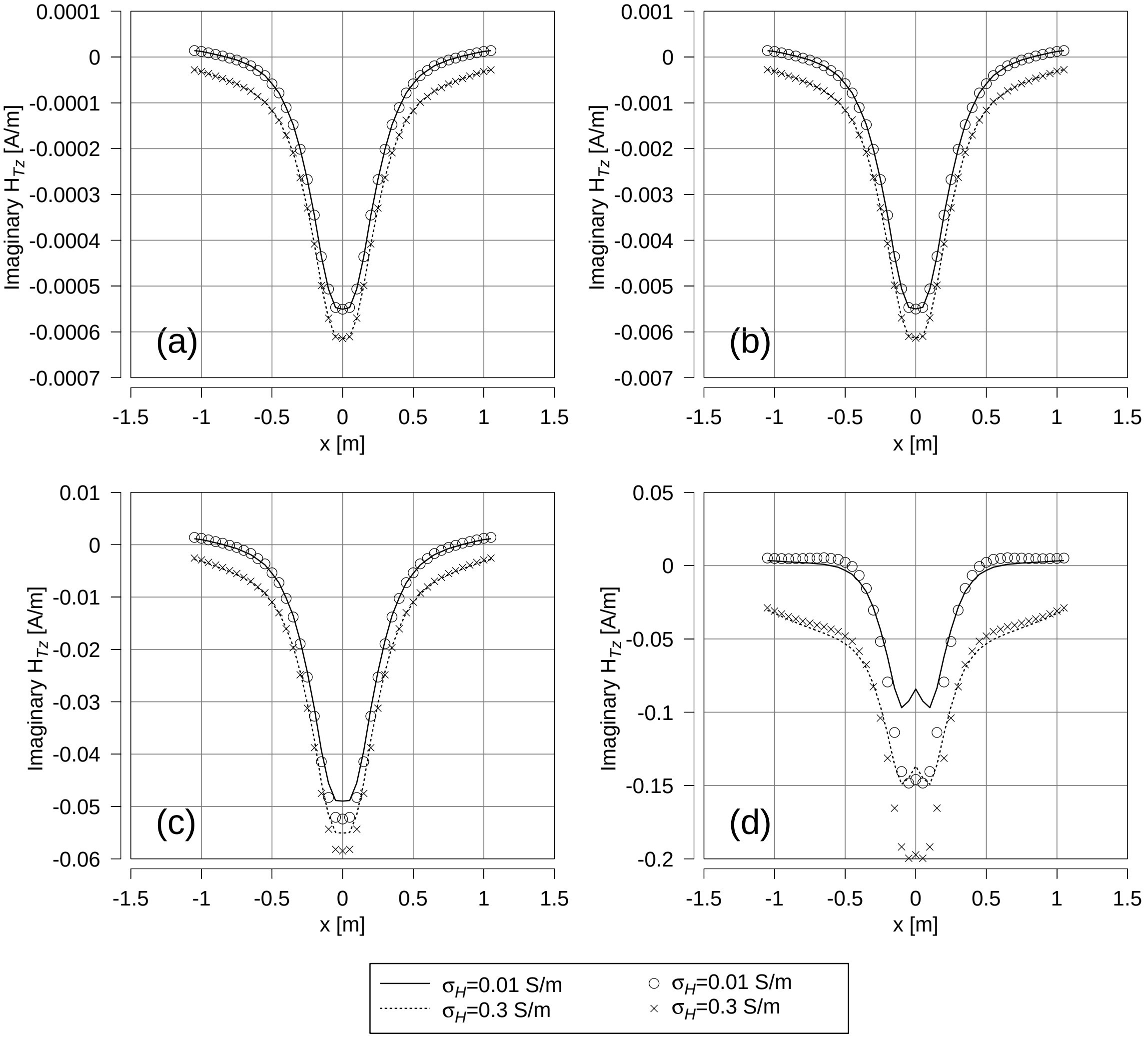

Fig. 7.6. The imaginary part of the vertical component of the total magnetic field measured at y=z=0 m for the VVP model (illustrated in figure 7.2). Solid and dashed curves indicate the magnetic field of the full model, and the symbols indicate the sum of the magnetic fields of each plate modeled individually. Four transmitter frequencies are modeled: (a) 30 Hz, (b) 300 Hz, (c) 3 kHz, and (d) 30 kHz.

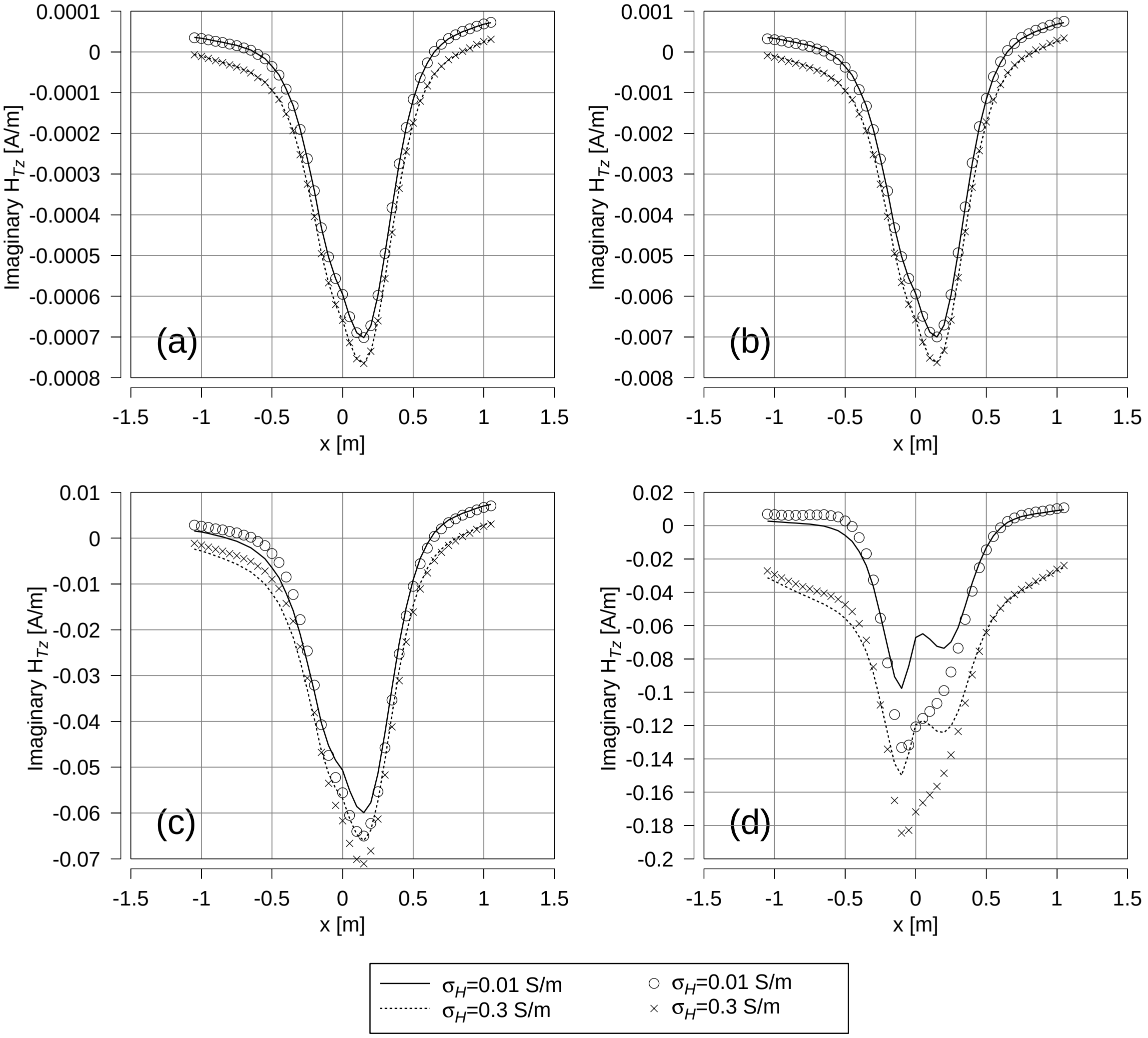

Fig. 7.7. The imaginary part of the vertical component of the total magnetic field measured at y=z=0 m for the HVP model (illustrated in figure 7.3). Solid and dashed curves indicate the magnetic field of the full model, and the symbols indicate the sum of the magnetic fields of each plate modeled individually. Four transmitter frequencies are modeled: (a) 30 Hz, (b) 300 Hz, (c) 3 kHz, and (d) 30 kHz.

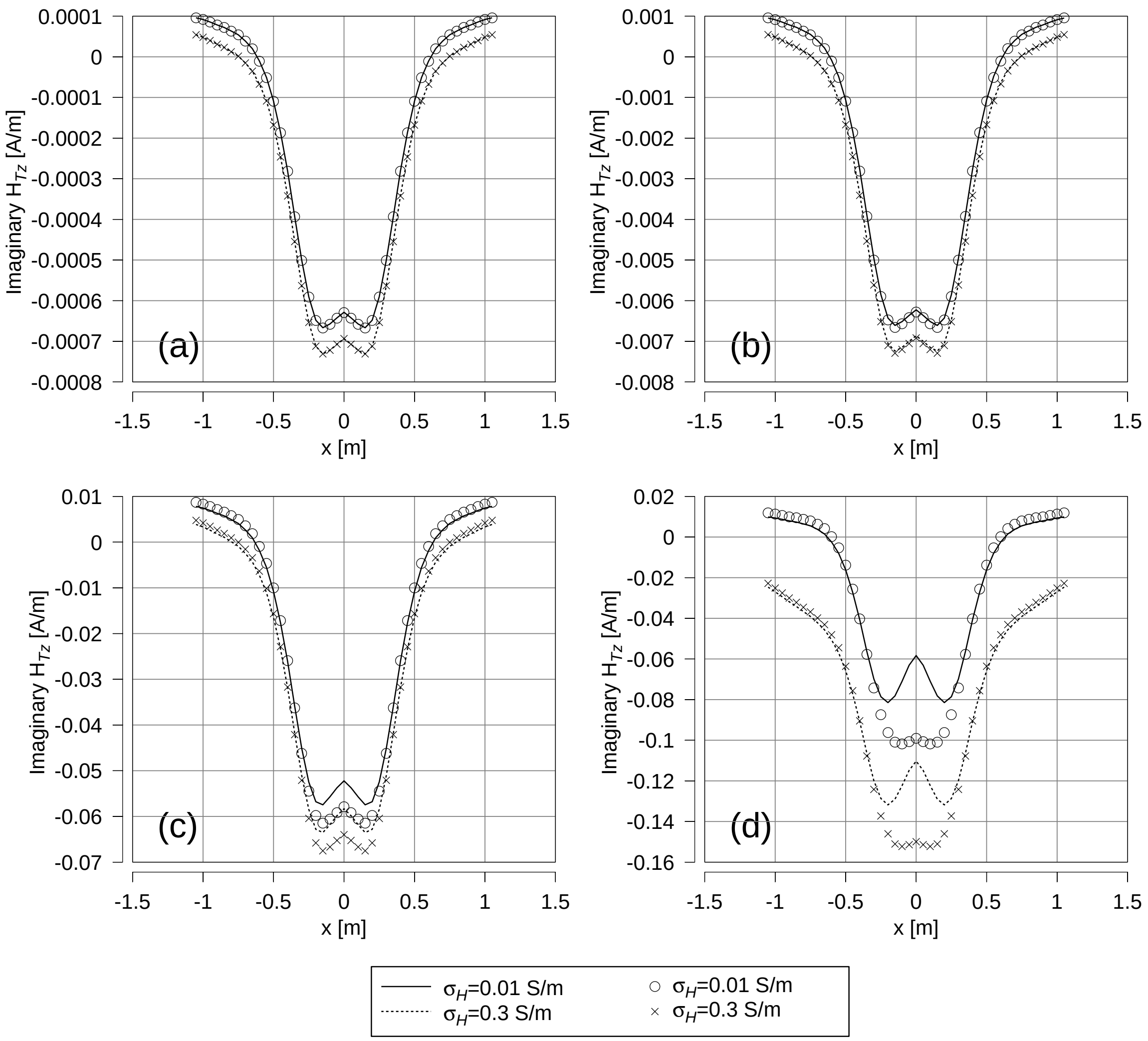

Fig. 7.8. The imaginary part of the vertical component of the total magnetic field measured at y=z=0 m for the HHP model (illustrated in figure 7.4). Solid and dashed curves indicate the magnetic field of the full model, and the symbols indicate the sum of the magnetic fields of each plate modeled individually. Four transmitter frequencies are modeled: (a) 30 Hz, (b) 300 Hz, (c) 3 kHz, and (d) 30 kHz.

large.

The interpretation of the responses of the VVP and HHP models are largely the same. The HVP model response is asymmetric, as expected. Interestingly, the horizontal plate has a stronger signal than the vertical plate at low frequencies, but at higher frequencies, the situation is reversed.

The z-component of the total mutual coupling factor $\mathbf{M}$ for all models at all four frequencies is displayed in figure 7.9. It is immediately evident that the conductivity of the host has little effect on the mutual coupling at high frequencies, regardless of model geometry. Additionally, the plates are strongly coupled at high frequencies for all model configurations. However, as frequency drops, the mutual coupling drops as well, and the conductivity of the host begins to play a more significant role. At 30 Hz, the effect of host conductivity is pronounced, although the magnitude of $M_z(x)$ is small.

At low frequencies, the flux through the plates in all target configurations is low because $\partial \mathbf{B}/\partial t$ is low. Therefore, the primary means of interaction between the buried targets is via galvanic current flow. Galvanic currents flow through the host, and are therefore strongly influenced by host conductivity.

The model configuration that exhibits the largest amplitude of mutual coupling varies with frequency. At high frequency, the VVP model appears to be the most strongly coupled configuration. However, at lower frequencies, the HHP and HVP configurations become the most strongly coupled. As illustrated in figure 7.10, at high frequencies, induced currents flow in closed horizontal loops around the outside of the plates, regardless of model configuration, in accordance with Lenz's law. The skin depth of the plates is approximately $\delta_{plate} = 0.03$ m at 30 kHz. The majority of the current is constrained to flow in the outer portion of the plate, and the high contrast in conductivity with the host medium causes any normal component of current flow to be canceled out, resulting in the high frequency current flow displayed in the top row of figure 7.10. As the frequency decreases, the skin depth increases, and the currents migrate into the plate. By the mechanism described above, the currents flow in a pattern dictated by the geometry of the conductor. The vor-

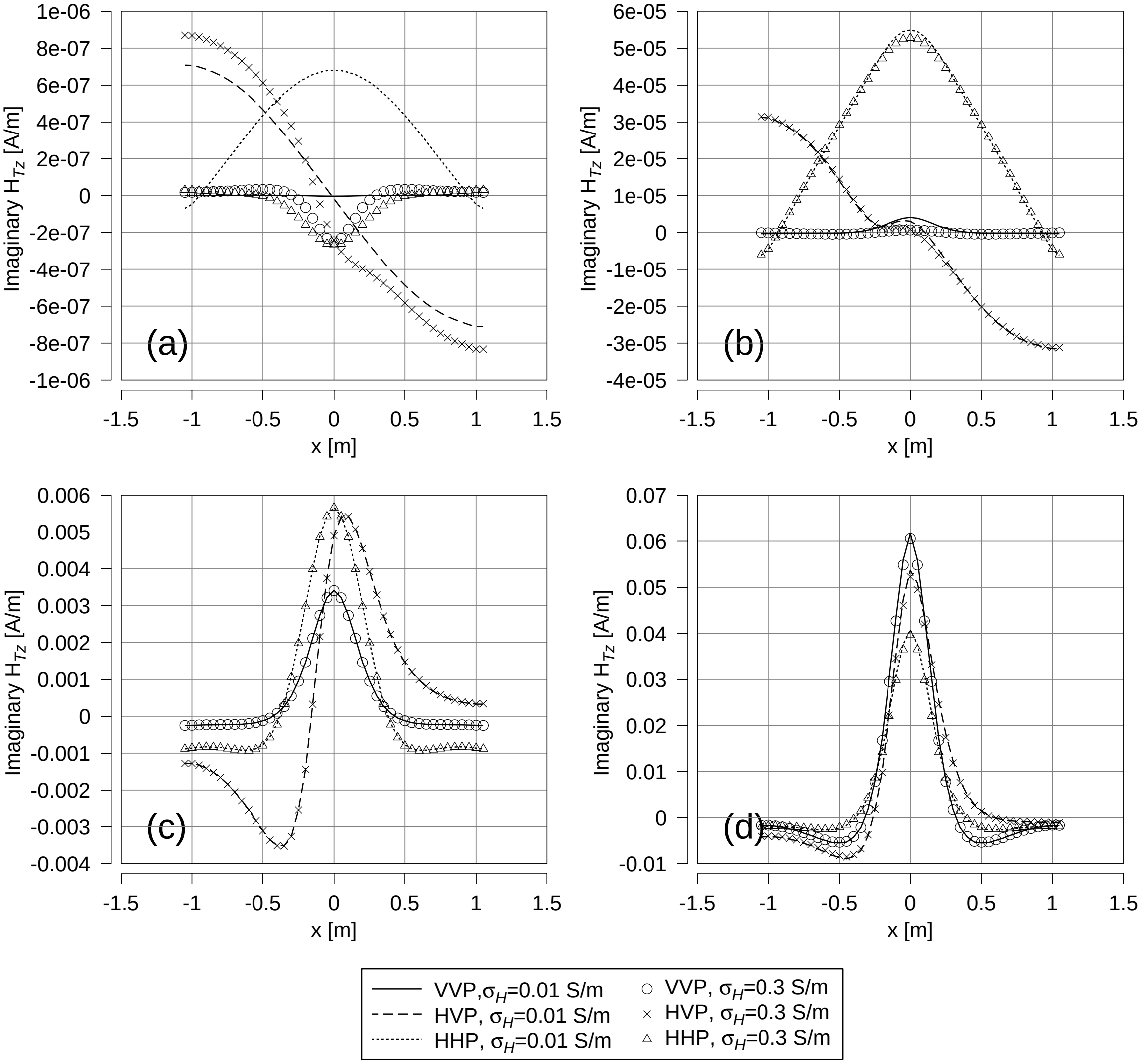

Fig. 7.9. The imaginary part of the total mutual coupling $M_z(x)$ for the VVP, HVP, and HHP models (figures 7.2, 7.3, and 7.4). Four transmitter frequencies are modeled: (a) 30 Hz, (b) 300 Hz, (c) 3 kHz, and (d) 30 kHz.

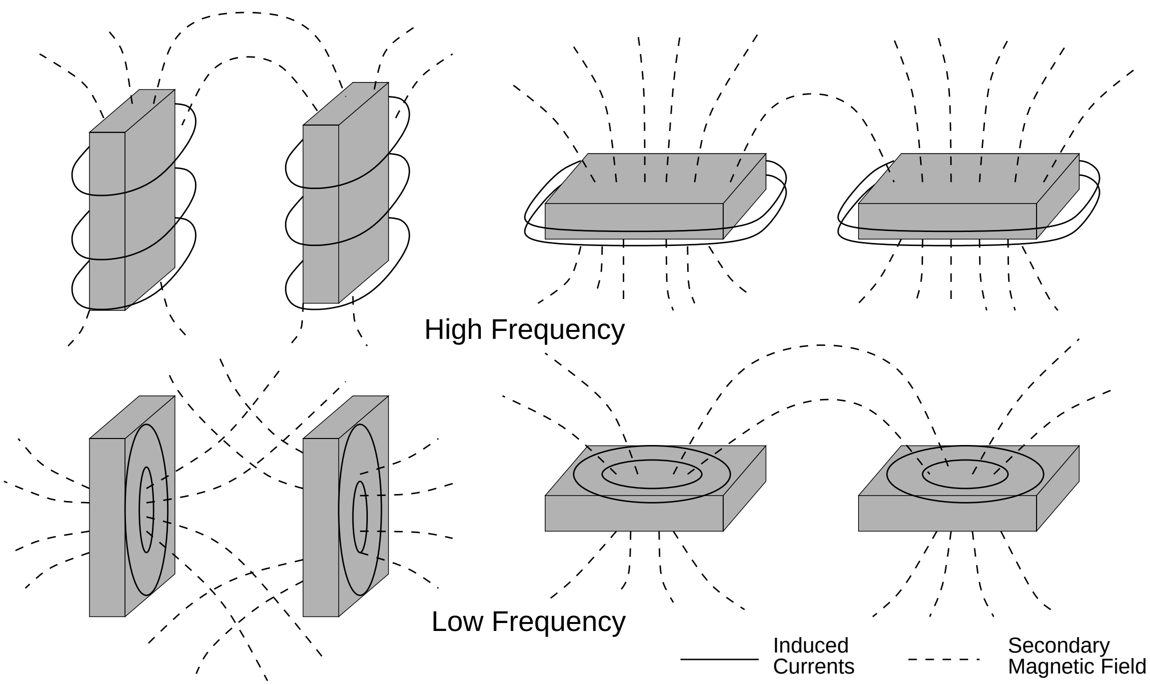

Fig. 7.10. As frequency decreases, the induced currents migrate into the center of the conductor, and flow in a manner dictated by the geometry of the conductor. Thus for vertical plates, the dipole moment of the induced currents shifts from vertical to horizontal.

ticity, or curl vector, of the induced current for the vertical plates (in the VVP and HVP models) thus shifts from vertical towards horizontal as frequency decreases. A frequency dependent vorticity also renders invalid (or incomplete) the hypothesis of the null-coupled and well-coupled models illustrated in figure 7.5.

As frequency decreases and the currents begin to migrate into the targets, the greatest mutual coupling is observed in the HHP and HVP models. Although the currents induced in the VVP model begin to approach the currents described in the so-called well-coupled model, the horizontal plates are illuminated by a greater amount of flux from the transmitter. At low frequencies, the mutual coupling, determined primarily by current flow through the host, is governed in part by the conductivity contrast of the targets and the orientation of the targets with respect to the induced current flowing in the host (West and Macnae, 1991).

The concept of a current vorticity that rotates with changing frequency can also explain

Fig. 7.11. Two aluminum plates buried in the VVP configuration in Brazos County, Texas.

Fig. 7.12. The modified EM63 system.

the change in asymmetry observed in the response of the HVP configuration. At high frequencies, the vertical plate is strongly flux-linked to the vertical magnetic field receiver at the earth's surface. As the vorticity of the induced current becomes horizontal, the contribution of the horizontal plate to the response dominates, because the vertical plate is no longer strongly coupled with the receiver.

The above interpretation is supported by time domain field measurements taken in Brazos County, Texas. Two square aluminum plates of thickness 0.6 cm measuring 0.3 m on a side were buried to a depth of 0.2 m (figure 7.11), and data were collected using a modified Geonics EM63 configuration, as shown in figure 7.12. The transmitter

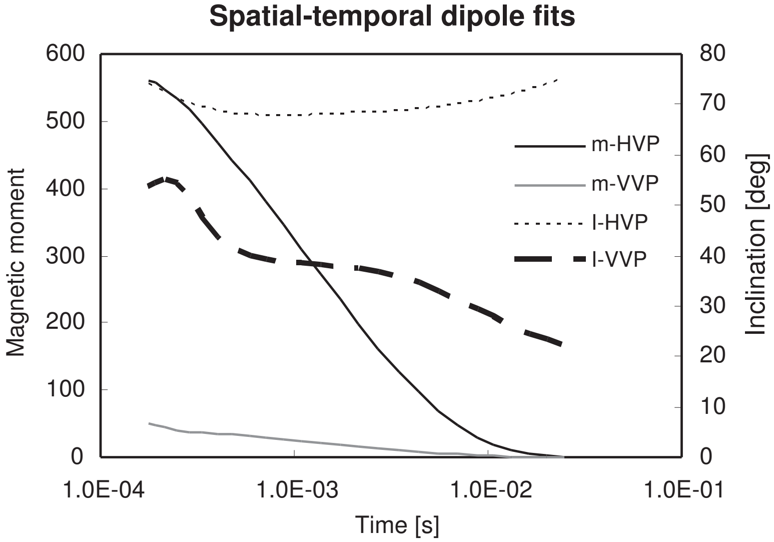

Fig. 7.13. The best-fitting decaying magnetic dipole parameters, as a function of Geonics EM63 time gate, for the VVP and HVP target configurations.

was centered on the plates, and the receiver was placed at 0.1 m intervals on a 2 × 2 m grid in order to simulate a multi-receiver array (Pierce et al., 2003). The HVP and VVP plate configurations were evaluated. The horizontal plates were buried to the depth of the midpoint of the vertical plate, and the gap between the plates was 0.1 m.

The measured EM63 responses were fit to a model of a magnetic dipole decaying exponentially in time after transmitter switch-off. The best-fitting dipole moment and inclination I at various time gates is shown in figure 7.13 for both HVP and VVP targets. At early times after shut-off (roughly equivalent to high frequencies in the frequency domain), the observed transient responses are best fit by a vertical trending dipole, where $I > 70^\circ$ for HVP, and $I > 55^\circ$ for VVP. The best fit at later times (i.e. low frequencies) for the VVP model is achieved with a a dipole oriented near horizontal, where $I \sim 20^\circ$. For the HVP model, the best-fitting dipole inclination remains greater than 70° for all times after transmitter switch-off. In short, the inclination of the best-fitting dipole for the HVP and VVP targets reproduces qualitatively the basic behavior drawn in figure 7.10.

Recalculation of M(x) on a locally refined mesh— The mutual coupling of the

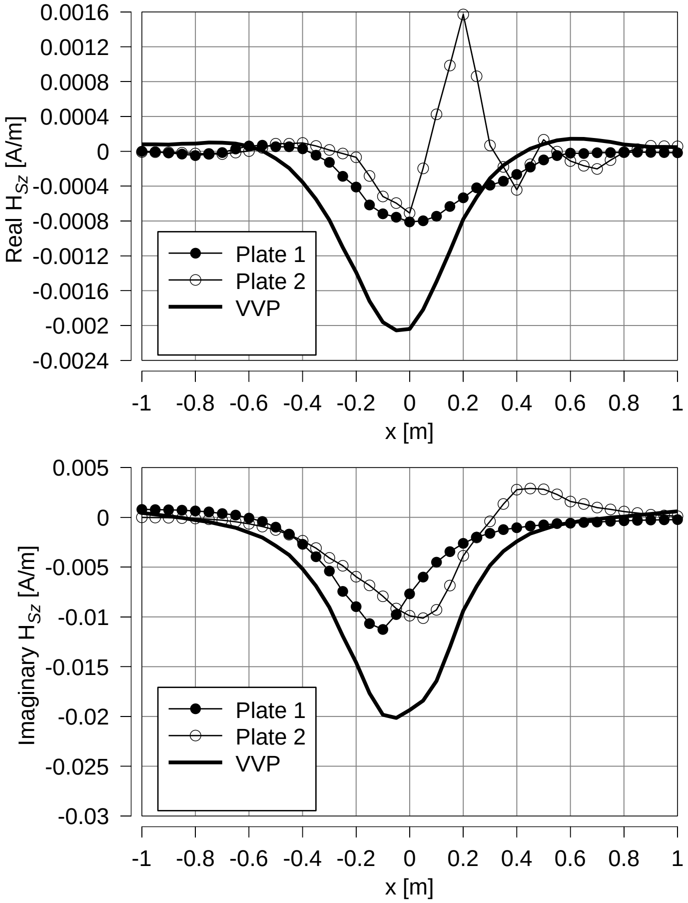

Fig. 7.14. The real and imaginary vertical secondary magnetic fields for the unrefined VVP model, where the transmitter frequency is 1 kHz. Results are given for each plate in isolation and the full VVP model.

UXO models, displayed in figure 7.9, was derived using the total magnetic field calculated on an unrefined finite element mesh. Greater accuracy and resolution, and an improved interpretation of results may be discovered by locally refining the mesh as dictated by the physics of the problem.

The efficacy of the local refinement subroutine is demonstrated by comparing the vertical secondary magnetic field of the VVP model calculated at 1 kHz using three different local refinement specifications with the magnetic field calculated using no local refinement (figure 7.14). The first, figure 7.15, is a region spanning from $z = -0.1$ to $z = 0.1$ m and the entire extent of the mesh in x and y, designed to capture subtle variations in the

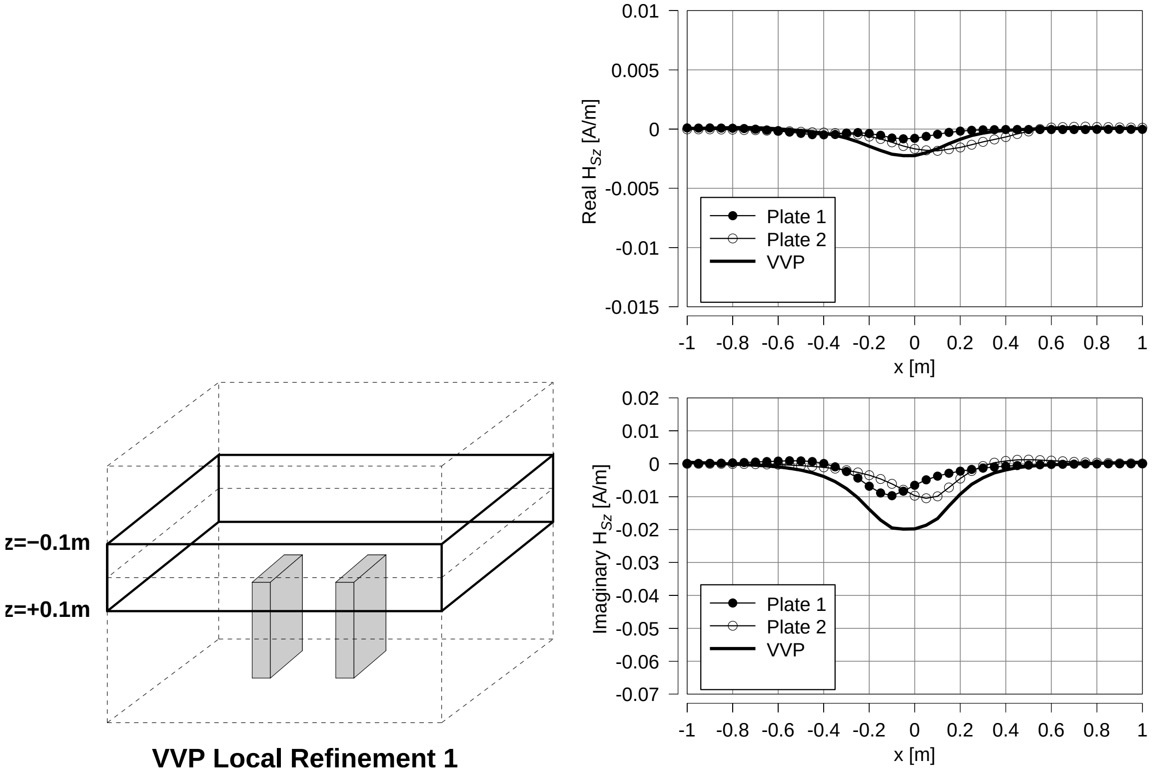

Fig. 7.15. A local refinement to the VVP model finite element mesh, intended to capture small details in the primary potentials. The resultant real and imaginary vertical secondary magnetic fields are shown where the transmitter frequency is 1 kHz.

primary potentials that are used in the construction of the right hand side of the finite element matrix. A second local refinement, figure 7.16, extends over the vertical plates, and the region there between, purposing to capture the minute details of the secondary potentials in the plates. The third refinement, figure 7.17, is the combination of the second refinement and a second nested refinement that covers the plate region alone. The third refinement is intended to further resolve the subtleties of the secondary potentials in the plates.

While the unrefined model performs reasonably well for the imaginary part of H_{Sz}, there is a large, unrealistic spike in the real part of the response of the second plate. Both the real and quadrature parts exhibit an asymmetry that is unexpected, given the symmetry of the VVP model. Adding the first local refinement grants a much more symmetric

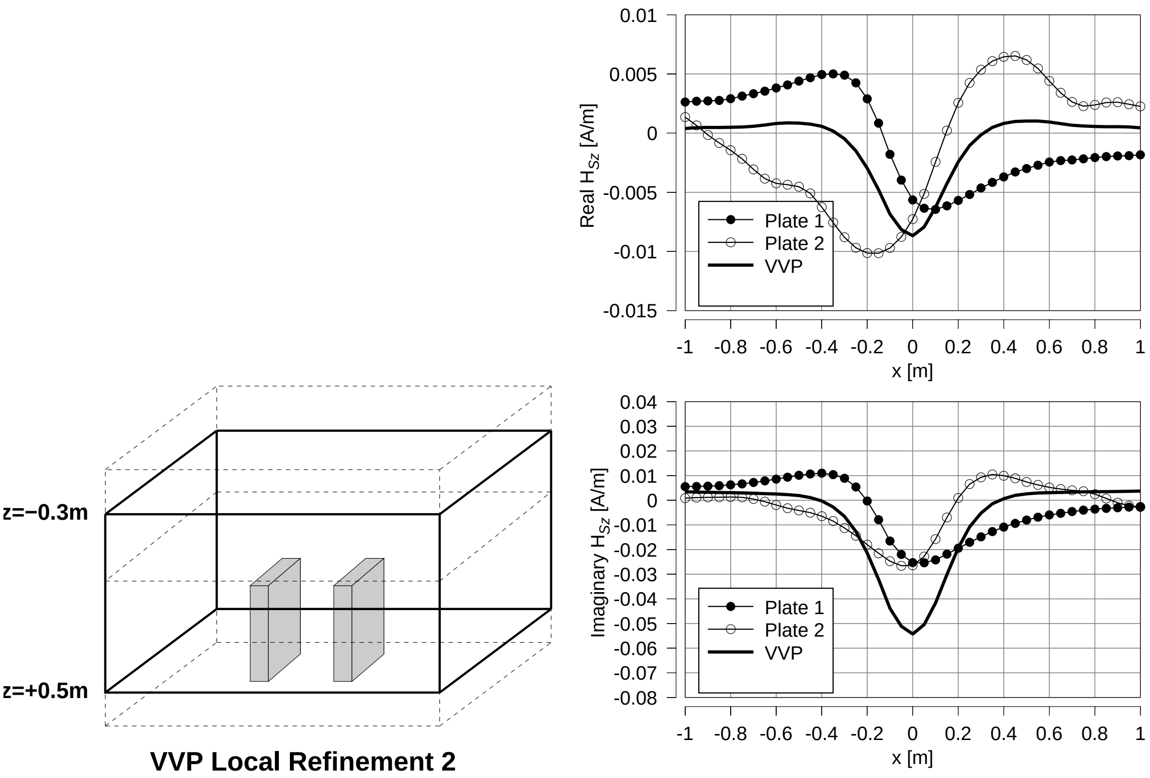

Fig. 7.16. A second local refinement to the VVP model finite element mesh, intended to capture small details in the primary potentials and the secondary potentials generated in the plates. The resultant real and imaginary vertical secondary magnetic fields are shown where the transmitter frequency is 1 kHz.

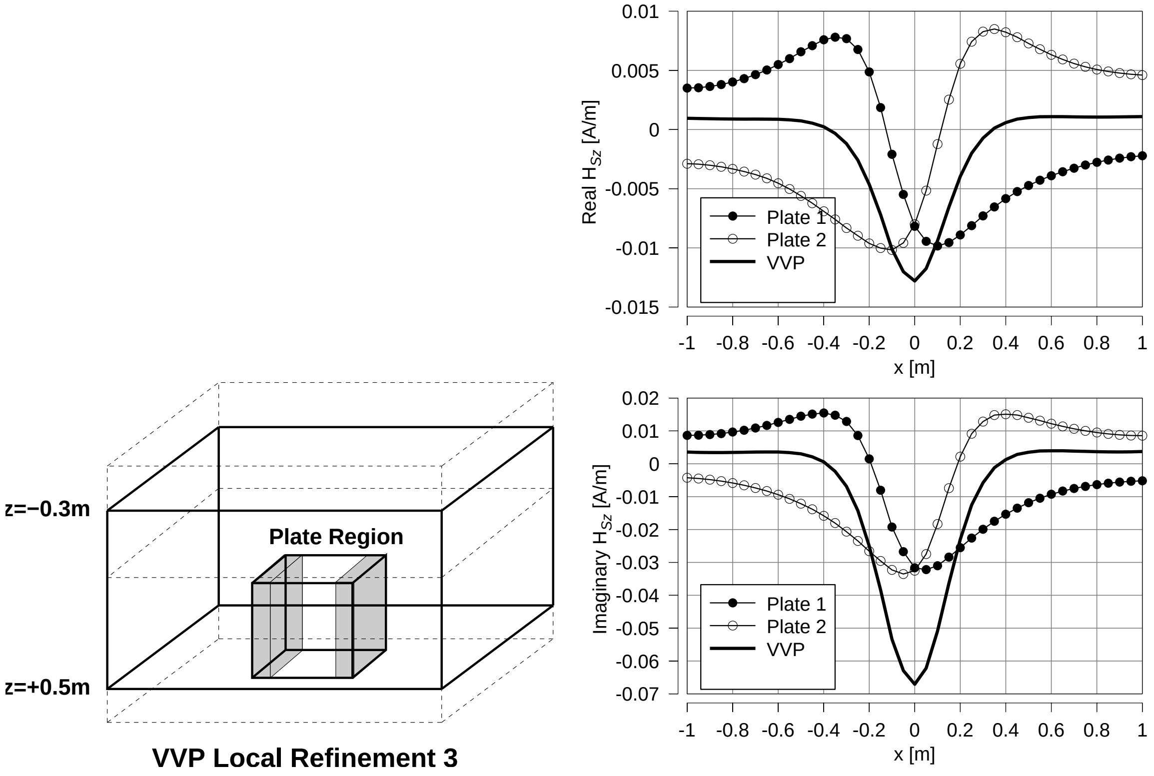

Fig. 7.17. A third local refinement to the VVP model finite element mesh, intended to capture small details in the primary potentials and the secondary potentials generated in the plates. Additional resolution has been added to the plates and the intervening region. The resultant real and imaginary vertical secondary magnetic fields are shown where the transmitter frequency is 1 kHz.

result. The second refinement increases the amplitude of the plate responses, but again introduces a slight asymmetry to the results. The best results are achieved when the third local refinement is applied. The results exhibit the expected symmetry, and an increased amplitude. There are no analytic or numerical data to verify the results against, but the third local refinement best suits the governing physics of the VVP model.

The mutual coupling factor is recalculated on a refined mesh, using the mesh refinement illustrated in figure 7.17, suitably adjusted for the plate region of each UXO model. The imaginary vertical mutual coupling is presented in figure 7.18. Although the introduction of local refinement has altered the morphology of the mutual coupling curves, the conclusions remain largely the same: 1) mutual coupling has a significant, quantifiable effect on the magnetic field response of a multiple-target model, 2) the conductivity of the host medium plays an important role in the magnitude of the mutual coupling 3) the induced dipole moment in the plates exhibits a rotation from vertical to horizontal as frequency decreases.

The largest host effect is now seen for the highest transmitter frequency, in stark contrast with the observations made using an unrefined finite element mesh. There are several possible explanations. The primary electric field, E_P^{ϕ}, is proportional to the transmitter frequency (West and Macnae, 1991). The currents generated in the halfspace, responsible for accumulating charge at conductivity interfaces, are in turn proportional to the primary electric field. Thus at low frequencies, the coupling of the plates due to charge dissipation is reduced. Alternatively, the larger host effect may be attributed to skin effect. The bulk of induced current in the halfspace host exists within the top skin depth. The skin depth of the halfspace at the four modeled transmitter frequencies are compared in table 7.1. Therefore, at higher frequencies, the plates are subject to a greater amount of current, and a greater amount of charge accumulation and galvanic current flow.

The application of local refinement also makes clearer the alteration of the induced current vorticity vector with frequency change, described above. The three Cartesian components of the real secondary magnetic fields are shown in figure 7.19 for the vertical plate

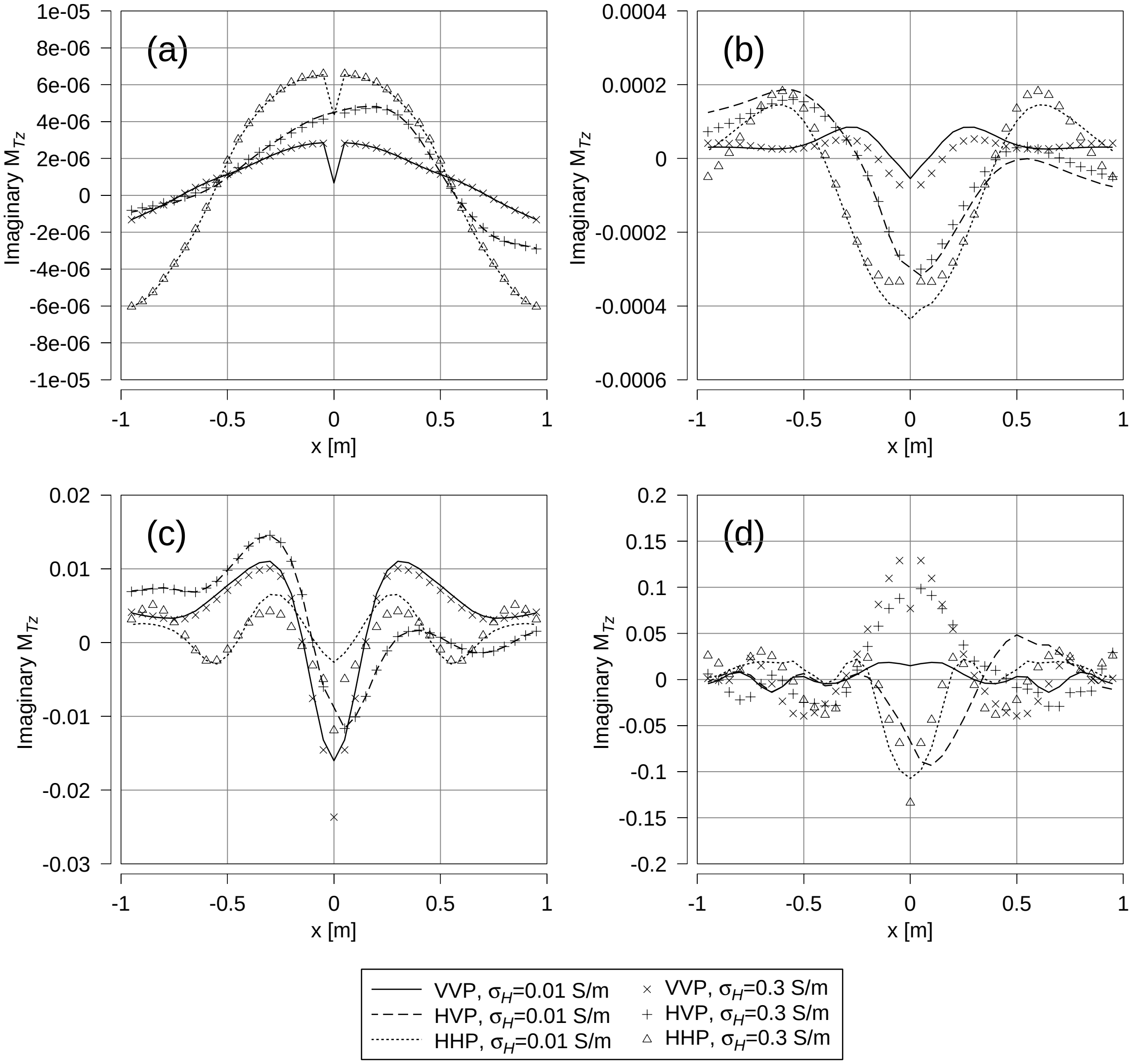

Fig. 7.18. The imaginary part of the total mutual coupling $M_z(x)$ for the VVP, HVP and HHP models (figures 7.2, 7.3, and 7.4) calculated using the finite element mesh local refinement illustrated in figure 7.17. Four transmitter frequencies are modeled: (a) 30 Hz, (b) 300 Hz, (c) 3 kHz, and (d) 30 kHz.

Table 7.1. UXO model halfspace skin depths.

Host Conductivity	Transmitter Frequency	Skin Depth (δ)
0.01 S/m	30 Hz	940.3 m
	300 Hz	297.4 m
	3 kHz	94.03 m
	30 kHz	29.74 m
0.3 S/m	30 Hz	171.7 m
	300 Hz	54.29 m
	3 kHz	17.17 m
	30 kHz	5.429 m

located to the right of the transmitter in figure 7.2, modeled in isolation. Similarly, the secondary magnetic field of the rightmost horizontal plate (from figure 7.4 is shown in figure 7.20. At 30 and 300 Hz, the magnetic field of the vertical plate clearly indicates a horizontal current vorticity vector. At 3 kHz, the vertical component of the magnetic field becomes asymmetric; the current curl vector begins to shift towards vertical. Finally, at 30 kHz, the asymmetry of the x and z components of the magnetic field suggests that the current moment has attained an even greater vertical component, although not quite as pronounced as indicated in figure 7.10.

Surprisingly, the horizontal plate secondary magnetic field requires a similar explanation. In fact, at 30 Hz, 300 Hz, and 3 kHz, the current flow in the horizontal plate appears to have a near-perfect horizontal curl vector, describing the current flow illustrated in figure 7.21. Only at 30 kHz does the magnetic field of the horizontal plate indicate a shift in vorticity toward vertical.

The currents induced in the horizontal plates are counterintuitive. As per the argument presented above, in conjunction with figure 7.10, the currents should flow such that the vorticity is vertical at all frequencies. However, it should be noted that the primary magnetic field varies with distance ρ from the center of the transmitter loop. The plates are therefore unevenly illuminated by this field, inducing additional modes of current flow in

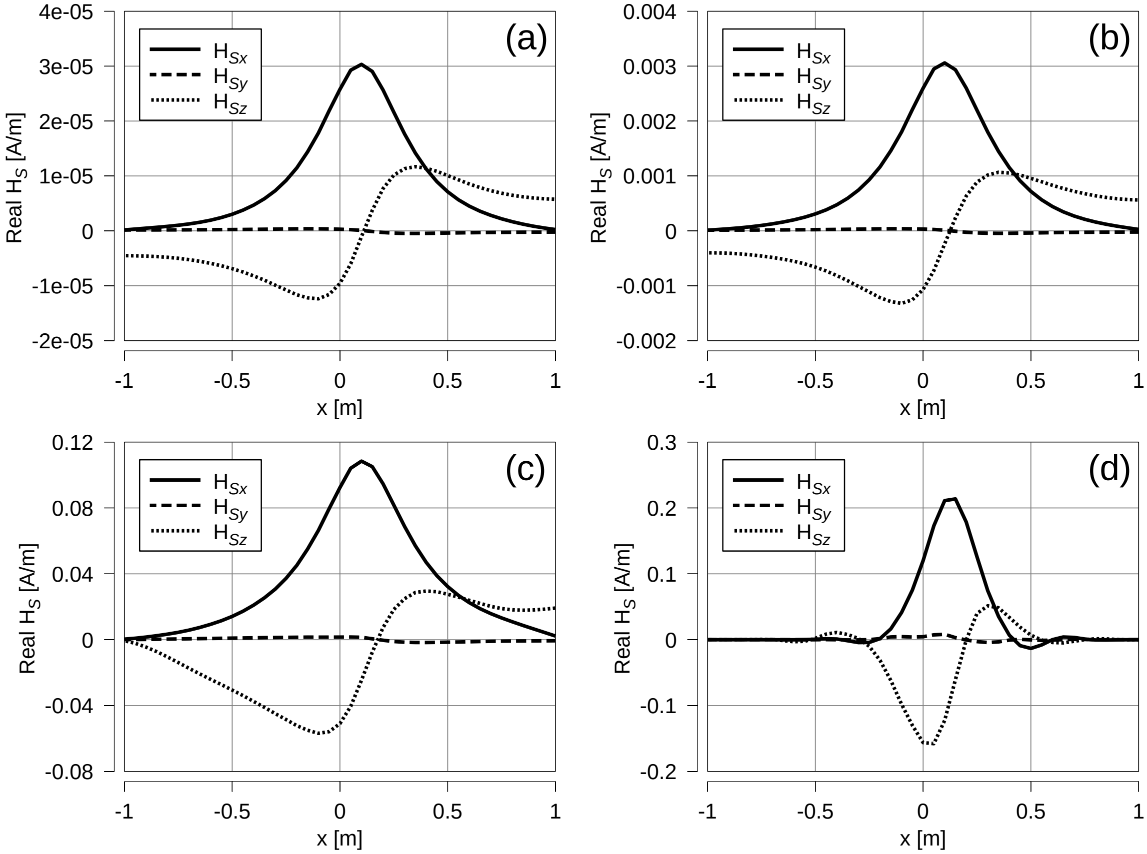

Fig. 7.19. The secondary real magnetic field of the rightmost vertical plate in figure 7.2, modeled in isolation at (a) 30 Hz, (b) 300 Hz, (c) 3 kHz, and (d) 30 kHz.

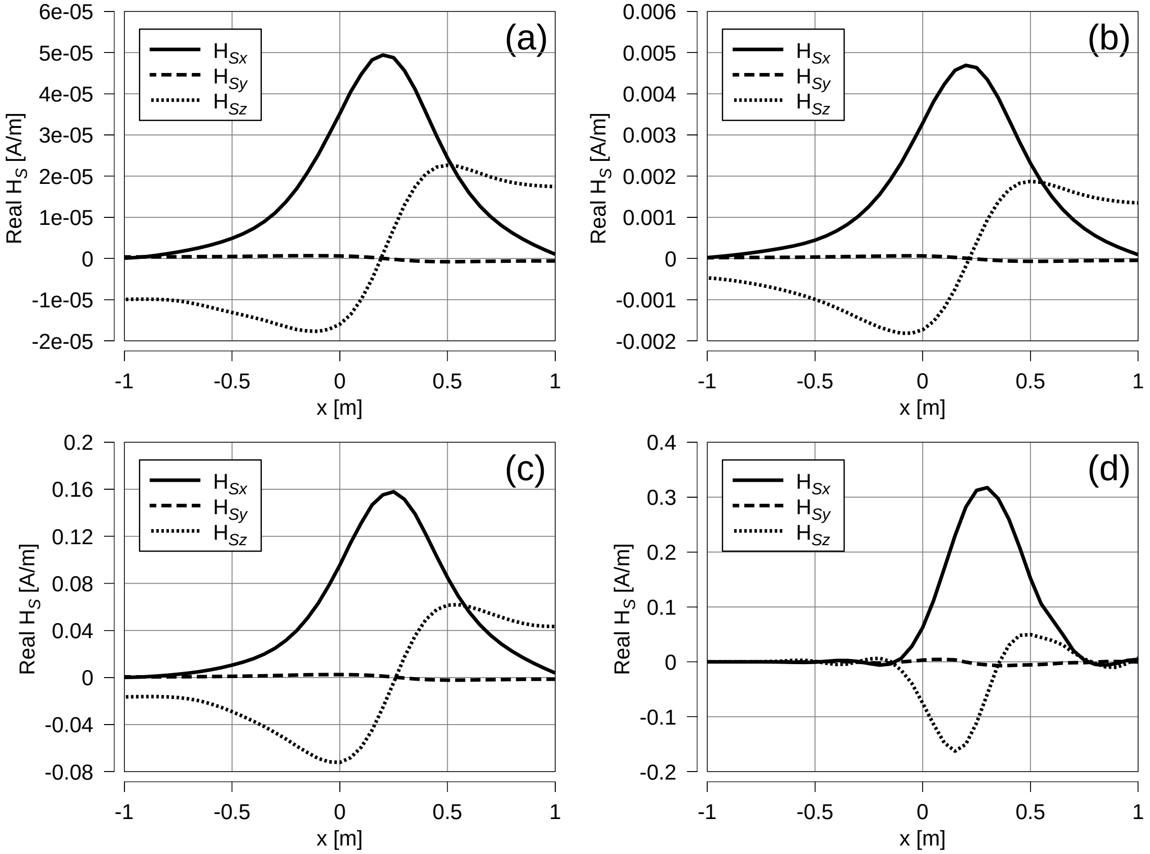

Fig. 7.20. The secondary real magnetic field of the rightmost horizontal plate in figure 7.4, modeled in isolation at (a) 30 Hz, (b) 300 Hz, (c) 3 kHz, and (d) 30 kHz.

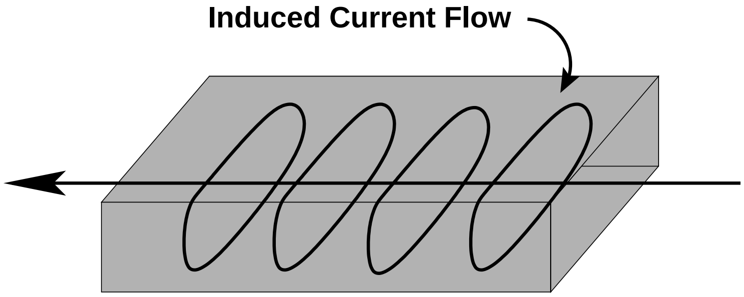

Fig. 7.21. Current flow induced in the rightmost horizontal plate, specified in figure 7.4, at low frequencies, as indicated by the magnetic fields displayed in figure 7.20.

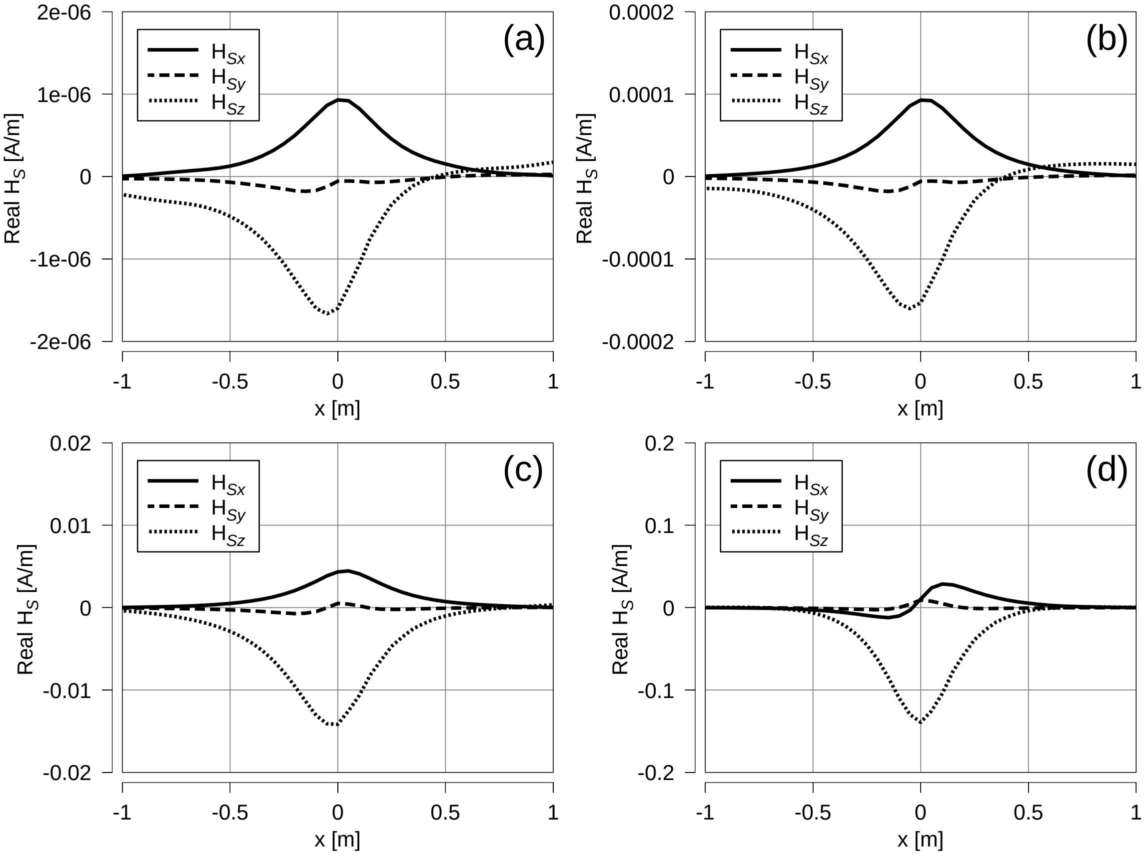

Fig. 7.22. The secondary real magnetic field of a single vertical plate (as specified in figure 7.2), centered beneath a transmitter operating at (a) 30 Hz, (b) 300 Hz, (c) 3 kHz, and (d) 30 kHz.

the plates. This hypothesis is easily tested by relocating the plates symmetrically beneath the transmitter. The resulting real secondary magnetic fields are presented in figure 7.22 for a single vertical plate, and in figure 7.23 for a single horizontal plate.

The vertical plate, as expected, has a strongly vertical current vorticity at high frequency (figure 7.22*d*). As frequency decreases, the curl vector begins to rotate toward horizontal. The vorticity of the currents flowing in the horizontal plate, on the other hand, remains vertical at all frequencies as expected.

The model that exhibits the greatest amount of mutual coupling again varies with frequency. At low frequencies (30 Hz and 300 Hz) the HHP and HVP models appear to be the most well coupled. At 3 kHz, the VVP model displays the greatest mutual coupling. At

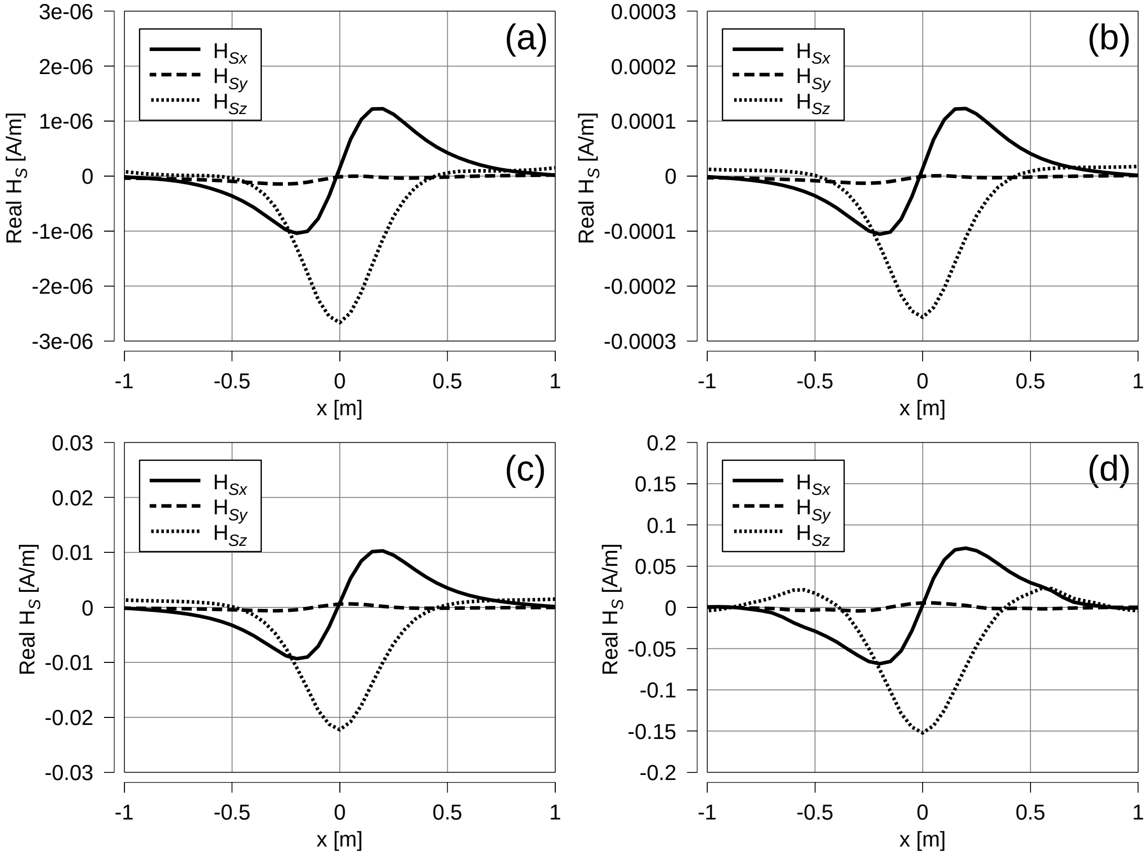

Fig. 7.23. The secondary real magnetic field of a single horizontal plate (as specified in figure 7.4), centered beneath a transmitter operating at (a) 30 Hz, (b) 300 Hz, (c) 3 kHz, and (d) 30 kHz.

30 kHz, the effect of host conductivity is pronounced, and the model exhibiting the largest magnitude of mutual coupling becomes dependent on the host conductivity.

A comparison between the mutual coupling curves is made clearer by normalizing **M** by the total vertical magnetic field. The results are displayed in figure 7.24. In figure 7.24, the effect of host conductivity at all frequencies can be better detected. Mutual coupling is also shown to increase with frequency, becoming as high as 20 times the total magnetic field for the HHP and VVP models at 30 khz, where the host conductivity is 0.3 S/m. The HHP configuration in particular shows a large effect of host conductivity in regions away from the transmitter. This can be attributed to the uneven illumination of the horizontal plate by the high frequency transmitter, as discussed above.

Time Domain Mutual Coupling

The mutual coupling factor **M** may also be calculated in the time domain. Figure 7.25 shows the time domain mutual coupling calculated at $x = y = z = 0$ m, for host conductivities of 0.01 and 0.3 S/m. The effect of host conductivity is clearly visible in the time domain, particularly at early times, which are roughly equivalent to high frequencies in the frequency domain. It is also interesting to note that the VVP model shows a distinct change in mutual coupling at about 3×10^{-7} s, which may be indicative of a change in current vorticity from vertical at early times, to horizontal as time increases. It may also be noted that the there is little difference between the mutual coupling of the three UXO models at early times when the host conductivity is 0.3 S/m, suggesting again that the host conductivity has a strong influence on the mutual coupling, overwhelming the effect of mutual coupling between the plates.

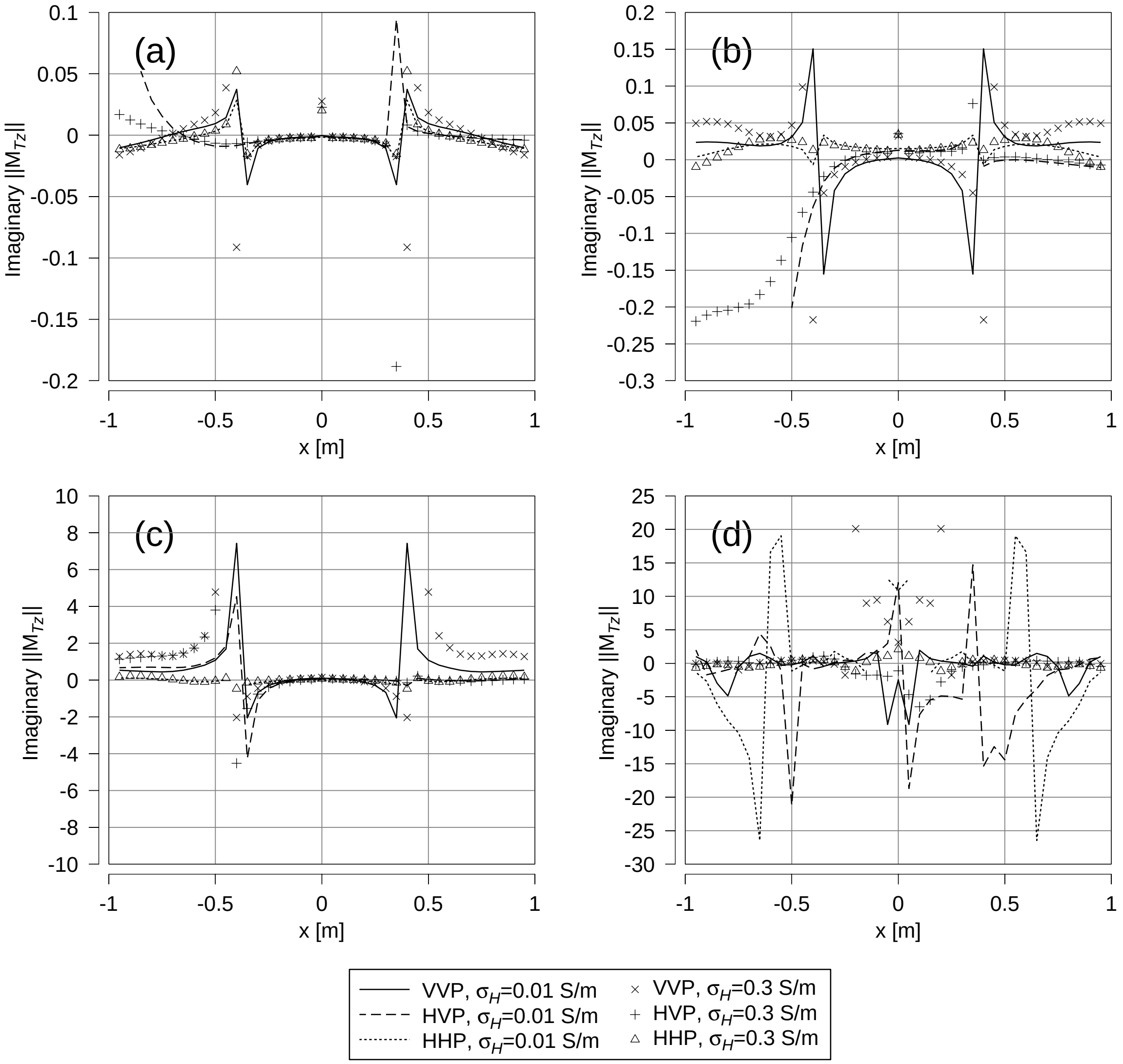

Fig. 7.24. The imaginary part of the total mutual coupling $M_z(x)$ for the VVP, HVP, and HHP models (figures 7.2, 7.3, and 7.4), normalized by the imaginary total magnetic field. Four transmitter frequencies are modeled: (a) 30 Hz, (b) 300 Hz, (c) 3 kHz, and (d) 30 kHz.

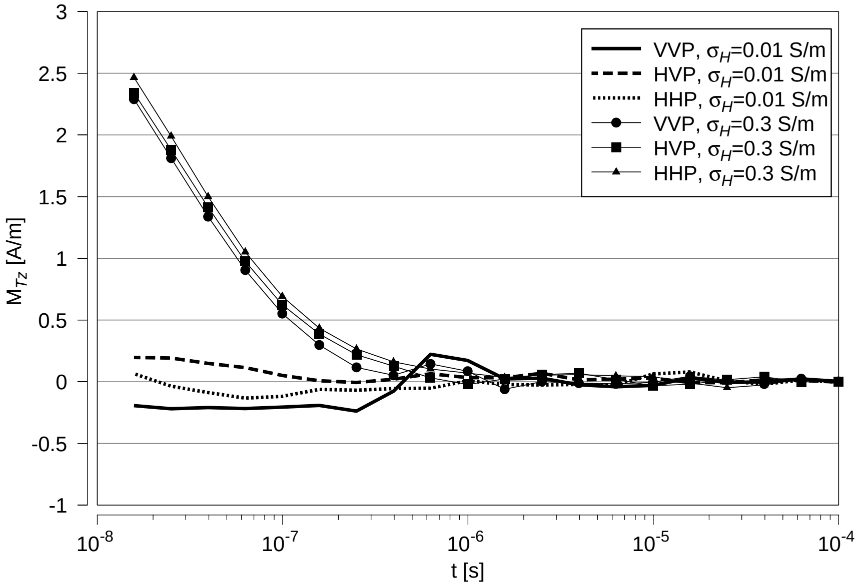

Fig. 7.25. Time domain mutual coupling factor M_{Tz} for the UXO models. The receiver is located at $x = y = z = 0$ m.

CHAPTER VIII

THE EFFECT OF TOPOGRAPHY ON THE CSEM RESPONSE

The finite element method allows for the specification of a completely unstructured mesh, provided that the quality factor of the mesh tetrahedra is sufficient. Practically, this means that the CSEM modeler may determine the response of an conductor of arbitrary shape, including realistic topographic undulations in the surface of the modeled Earth.

An understanding of the effects of topography on the CSEM response is important because the large majority of real world surveys are not conducted on a flat surface. Topographic highs act as an additional conductor above the surface of the Earth. Lows also affect the signal because no subsurface current may be induced in a topographic low, altering the host current geometry. Thus, survey data may be incorrectly interpreted if the effect of topography is ignored. However, in practice, interpretation of real world field data is regularly carried out under the assumption that the surface of the earth is flat.

Other attempts to correctly model and understand the effect of topography on the electromagnetic response can be found in the literature. A 2D finite element foward modeling algorithm is presented with topographic modeling results for LOTEM and CSMT systems in Mitsuhata (2000). Corrections for misalignment of transmitter and receiver coils due to the presence of topographic features are described in Sinha (1980), Fullagar (1981), and Fullagar and Oldenburg (1984). Simple correction formulas for the presence of a simple slope are found in Anderson et al. (1983).

The results presented in this dissertation represent only preliminary steps into the understanding of the effects of topography on the CSEM response. Although interesting conclusions have been drawn, these hypotheses may not be applicable to models other than the ones presented here.

Parametric Study: A Simple Horst Model

A simple model of a horst is illustrated in figure 8.1*a*. Although a scarp may be more conceptually simplistic, the horst model overcomes the difficulties associated with

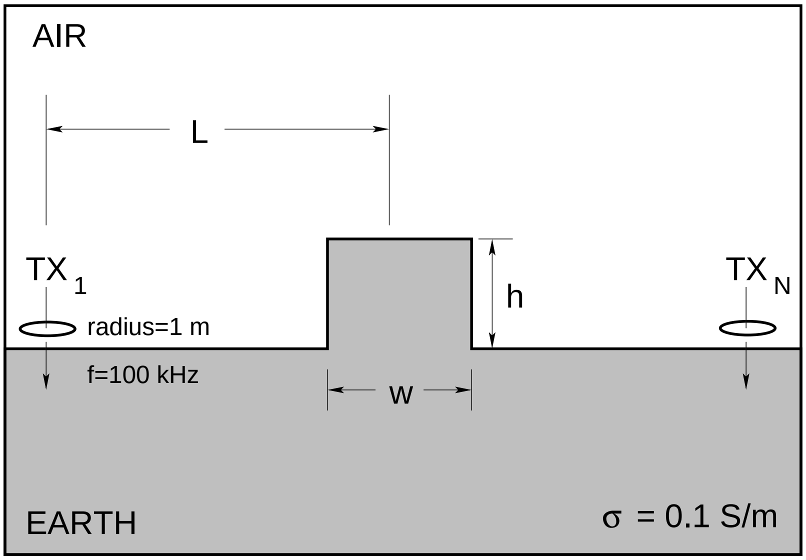

(a) "Horst" Model

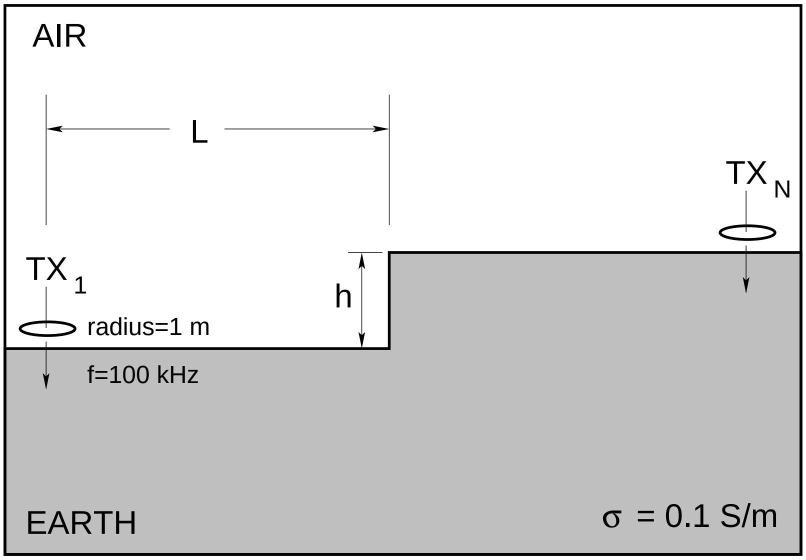

(b) "Scarp" Model

Fig. 8.1. Horst (a) and scarp (b) topography models.

mesh truncation, as the transmitter is required to move in the cross-strike direction for this study. A double halfspace primary conductivity model is defined, yielding a secondary conductivity model that contains only the topographic high. It is desirable to maintain an identical mesh for each transmitter location for the sake of consistency. Creating a mesh large enough to prevent mesh truncation at the rightmost transmitter location in figure 8.1*b*, and to properly mesh the source region for the leftmost transmitter location would be beyond the memory limits of the computer used for this study. Choosing a horst model is not without its caveats, however. An additional degree of difficulty is introduced into the interpretation of the modeled response, and an additional model parameter—the width of the horst—is also introduced.

The horst model (figure 8.1*b*) has a skin depth in the earth of

$$\delta = \sqrt{\frac{2}{\sigma \mu_0 \omega}} \approx 5 \text{ m}. \tag{8.1}$$

The distance from the transmitter to the center of the horst, L, varies between $-3\delta$and $+3\delta$, and the height of the horst varies from 0δ to 1δ. The 28 calculated topographic models are displayed for reference in table 8.1. The transmitter and receiver are located directly on the surface of the earth. Thus, as in a real-world CSEM data collection exercise, the transmitter and receiver move vertically in response to changes in surface altitude. The receivers are located between $x = -20$ m and $x = 20$ m, with a spacing of 0.5 m.

The effect of the topographic feature on the total magnetic field is the total field less the transmitter primary field and the halfspace secondary response:

$$\mathbf{T}(\mathbf{r}) = \mathbf{H}_T(\mathbf{r}) - [\mathbf{H}_P(\mathbf{r}) + \mathbf{H}_S^{Halfspace}(\mathbf{r})], \tag{8.2}$$

which is simply the secondary response of the topographic feature.

In order to begin to understand the full impact of the presense of the topographic feature, the three Cartesian components of the secondary magnetic field of the horst are

Table 8.1. Topographic model reference.

Model No.	Horst Height (h)	Transmitter-Horst Center Separation (L)
1	0.1 δ (0.5 m)	-3 δ (-15 m)
2		-2 δ (-10 m)
3		-1 δ (-5 m)
4		0 δ (0 m)
5		1 δ (5 m)
6		2 δ (10 m)
7		3 δ (15 m)
8	0.2 δ (1.0 m)	-3 δ (-15 m)
9		-2 δ (-10 m)
10		-1 δ (-5 m)
11		0 δ (0 m)
12		1 δ (5 m)
13		2 δ (10 m)
14		3 δ (15 m)
15	0.5 δ (2.5 m)	-3 δ (-15 m)
16		-2 δ (-10 m)
17		-1 δ (-5 m)
18		0 δ (0 m)
19		1 δ (5 m)
20		2 δ (10 m)
21		3 δ (15 m)
22	1.0 δ (5.0 m)	-3 δ (-15 m)
23		-2 δ (-10 m)
24		-1 δ (-5 m)
25		0 δ (0 m)
26		1 δ (5 m)
27		2 δ (10 m)
28		3 δ (15 m)

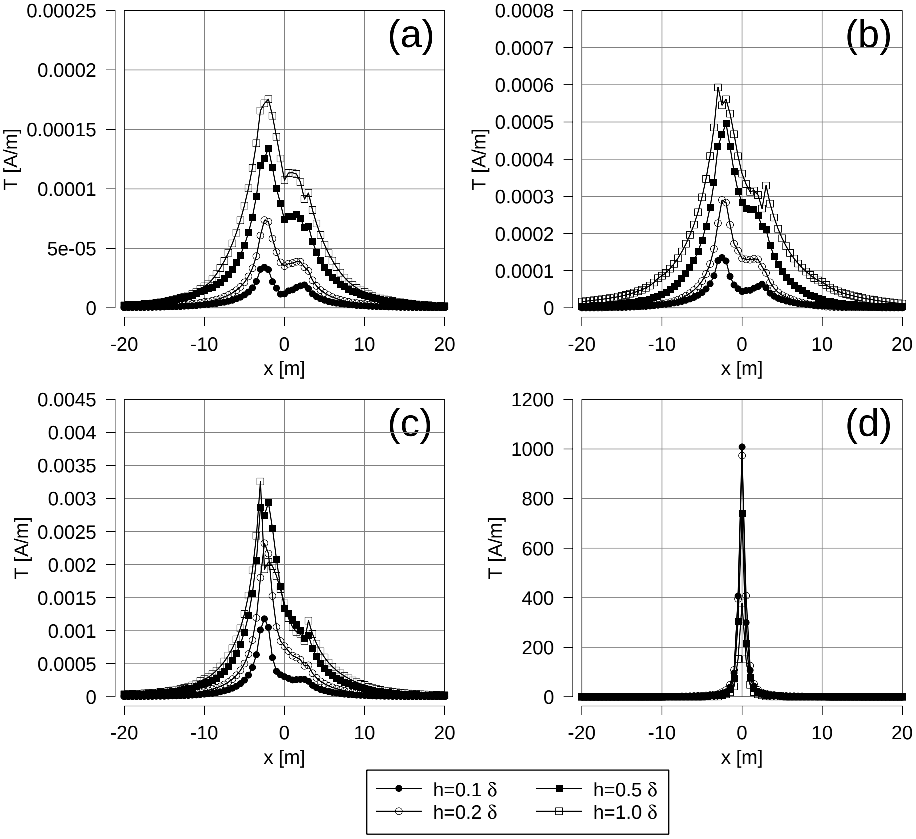

Fig. 8.2. The effect of a horst of varying height h on the calculated total magnetic field of the model illustrated in figure 8.1*b*, where the transmitter-horst center separation is (a) $L = -3\delta$, (b) $L = -2\delta$, (c) $L = -1\delta$, and (d) $L = 0\delta$.

combined into a single quantity:

$$T(\mathbf{r}) = H_{Sx}^{Horst}(\mathbf{r}) + H_{Sy}^{Horst}(\mathbf{r}) + H_{Sz}^{Horst}(\mathbf{r}). \tag{8.3}$$

This sum is modulated to further reduce the amount of data by combining the real and imaginary portions into a single quantity.

The results are displayed in figure 8.2. The results for models 5–7, 12–14, 19–21, and 26–28 are not shown because as expected, these results are symmetric with the corresponding negative value of L.

Several conclusions may be drawn from this figure. The effect of the topographic feature on the total response increases as L decreases, as expected. The curves are asymmetric for $L \neq 0$, which may be attributed to at least two factors. The high frequency of the transmitter implies that the current density induced in the horst will fall off quite rapidly as distance from the transmitter increases, so that the largest amount of current density resides in the leftmost part of the horst for $L < 0$ m. Also, the current density induced in the horst does not have a perfectly vertical vorticity, imparting an x-component to the secondary magnetic field.

Increasing the height of the horst increases the topographic effect T. Furthermore, the morphology of the T curves at various horst heights is similar, indicating that the topographic effect scales with h—a feature that may prove useful in improving the accuracy of the inversion of real data.

When $L = 0$ m, the T curves become symmetric, as dictated by the symmetry of the model, and quite large. The magnitude of the T curve indicates that the bulk of the image current density beneath the transmitter is localized within the horst.

A more quantitative comparison between the models may be acheived by normalizing the quantity T by the total magnetic field,

$$\|T(\mathbf{r})\| = \frac{T(\mathbf{r})}{(|H_{Tx}(\mathbf{r})| + |H_{Ty}(\mathbf{r})| + |H_{Tz}(\mathbf{r})|)}. \tag{8.4}$$

That is, the normalized topographic effect T describes the effect of the horst as a fraction of the total magnetic field, which is the quantity measured by most frequency domain CSEM systems. The results are displayed in figure 8.3 for $L \leq 0$ m.

The normalized curves are remarkably similar for transmitter locations to the left of the horst. The maximum contribution of the topographic feature to the total magnetic field increases slowly as the separation distance L decreases, ranging from roughly 50 percent of the total magnetic field when $L = -15$ m, to approximately 63 percent when $L = -5m$ for a horst of height $h = 5.0$ m. As distance from the transmitter increases, the models show an increase in the horst contribution to the total field, because the primary field decreases monotonically away from the transmitter location. The secondary field falls off in a similar

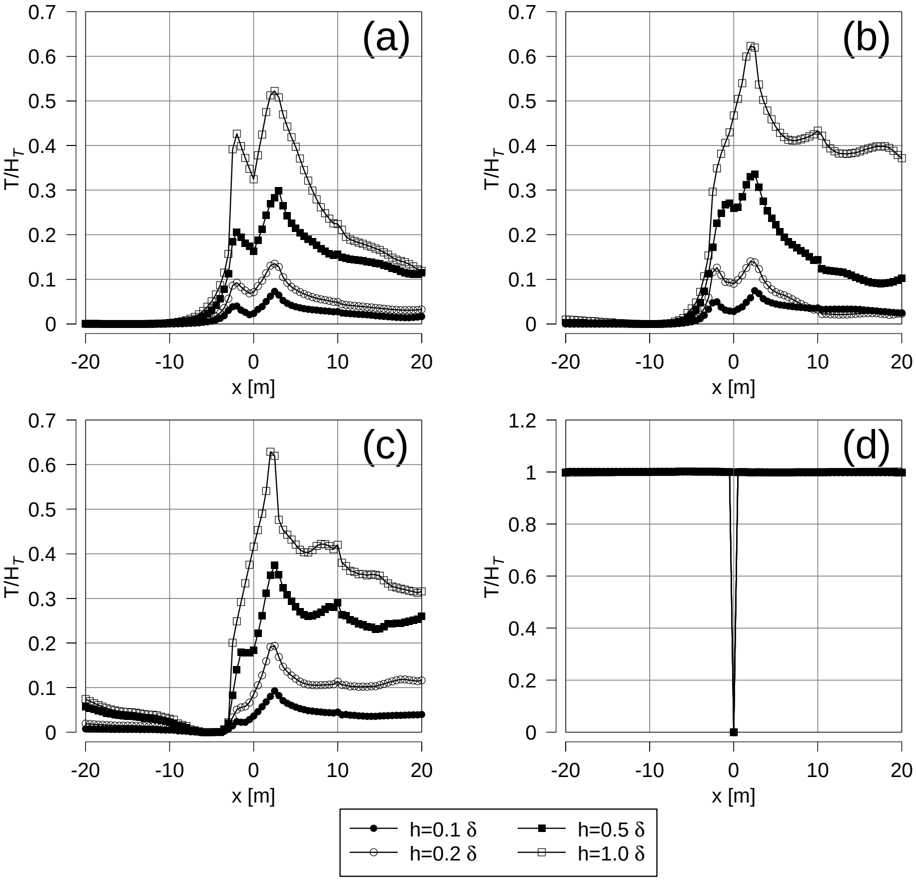

Fig. 8.3. The effect of a horst of varying height h on the calculated total magnetic field of the model illustrated in figure 8.1b, normalized by the total magnetic field. The transmitter-horst center separation is (a) $L = -3\delta$, (b) $L = -2\delta$, (c) $L = -1\delta$, and (d) $L = 0\delta$.

fashion, but is sourced by the current density in the horst. Similarly, increasing L causes the normalized T curve to fall off more rapidly at receiver locations to the right of the horst.

For a transmitter located directly over the center of the horst ($L = 0$ m), the topographic feature is shown (figure 8.3) to contribute nearly 100 percent of the total magnetic field for all receiver locations except the center of the transmitter loop. The apparent lack of a contribution at $x = 0$ is due to the singularity in the primary magnetic field at that location.

CHAPTER IX

CONCLUSION

The accurate interpretation of controlled-source electromagnetic field data relies upon an understanding of the response of a fully three-dimensional conductivity structure. Furthermore, the correct inversion of field data depends upon the availability of a reliable three-dimensional forward modeling algorithm. To this end, a numerical solution of the governing Maxwell's equations has been implemented, following work by Biro and Preis (1989) and Badea et al. (2001), among others. This solution uses the Galerkin finite element method, which allows the model to be discretized into an unstructured mesh—an important feature that permits the mesh elements to be adjusted to accurately represent irregular conductor geometries. In addition, the finite element method allows the mesh to be refined locally, increasing resolution only where needed.

The governing equations have been reformulated in terms of a magnetic vector and an electric scalar potential, overcoming difficulties related to numerical errors and constraints on the fields at mesh boundaries, and reducing the number of unknown quantities sought in the numerical solution. The governing equations have also been separated into a known primary and an unknown secondary portion, thereby removing the singularity associated with a CSEM magnetic dipole source from the solution, The magnetic and electric field components have been recovered from the potentials using the moving least squares interpolation algorithm (Tabarra et al., 1994) to perform the required numerical differentiation of the scalar and vector potentials.

In order to ensure the quality and accuracy of the fully three-dimensional numerical solution, the algorithm was developed by solving a series of differential equations with known, analytic solutions. The test problems ranged in complexity from simple one-dimensional scalar differential equations, to three-dimensional coupled vector equations. The finite element algorithm successfully passed these tests, generating only minor error.

A one-dimensional CSEM modeling code was also created, capable of modeling the magnetic and electric field response of a model consisting of an arbitrary number of conductive layers. The one-dimensional solution was verified successfully against a semi-analytic solution from Ward and Hohmann (1987).

The three-dimensional finite element CSEM code was also verified against a one-dimensional analytic halfspace solution. Although the test was successful, it illustrated that inaccuracies may be encountered if the model mesh is truncated too close to the transmitter. These difficulties were partially overcome by including the known halfspace response in the primary potentials.

The performance of the code was verified against published model results from a three-dimensional finite element solution by Pridmore, et al. (1981) for a conductive slab buried in a conductive host medium. The result was a good qualitative match with the published results. The exercise did indicate, however, the necessity and efficiency of the local refinement algorithm. The best match resulted when local refinement was applied to both the region occupied by the slab, and the region occupied by the transmitter, and the large image current density that is generated directly beneath it. Although relegated to the primary portion of the model calculation, these components of the model do appear in the right hand side of the finite element equation. Thus, improper representation of the subtle nuances therein can result in improper model calculation. Further, the target region must be well meshed in order to model small scale induction phenomena in the target. Also, it was demonstrated that altering the user-specified parameters of the moving least squares algorithm can have a significant impact on the calculated EM fields.

Although the algorithm was formulated in the frequency domain, the evaluation of the time domain response was conducted by performing an inverse Fourier transform of a splined set of discrete frequency domain model results, after the fashion of Newman, et al. (1986). The results for several three-dimensional models were evaluated qualitatively, and it was determined that the data exhibited many of the expected features, considering the governing physics, and the model.

A functioning three-dimensional modeling code provides an important tool for the study of CSEM phenomena that are poorly understood, or that plague the interpretation of three-dimensional field data. In this study, the effects of mutual coupling in a conductive host, and the effect of surface topography were explored.

Mutual coupling—the combination of mutual induction and current flow via charge dissipation through a conductive host—was shown to be a significant contributor to the calculated total magnetic of models containing multiple high conductivity targets. The magnitude of the mutual coupling factor **M** ranged as high as 20 times the magnitude of the total field at high model frequencies. It was also demonstrated that the effect of mutual coupling is dependent upon source frequency, target geometry and respective orientation (with other targets and with the host), and host conductivity.

Furthermore, the need for the local mesh refinement algorithm was again demonstrated. The calculated magnetic fields were altered significantly with the application of local refinement, approaching a form dictated by the governing physics. In consequence, the mutual coupling were also changed, leading to new conclusions.

Interestingly, it was noted that the vorticity of the current density induced in the vertically oriented plate-like high conductivity targets moved from a vertical orientation at high frequencies, to a horizontal orientation at low frequencies—an observation upheld qualitatively by time-domain field experimentation. Investigation of this phenomenon revealed a similar, counterintuitive pattern for a horizontal target orientation. Further modeling confirmed that this was due to uneven illumination of the horizontal plate by the transmitter, indicating that location of the target relative to the transmitter is important in determining mutual coupling.

Mutual coupling was shown to increase with transmitter frequency, and with host conductivity. Also, it was demonstrated that as frequency increases, the effect of host conductivity increases as well. In short, varying the host conductivity can significantly alter the mutual coupling among buried conductors, and therefore, modeling methods that assume the conductors exist in free space may yield inaccurate results. Barring the contribution of the host to mutual coupling, modeling methods that compose the response of the full conductivity model from the responses of the individual targets do not take into account the effect of mutual induction, and may also return inaccurate results.

The effect of topography is often ignored in the interpretation of field data. However, the effect of a simple horst has been shown to be quite significant, even for horst elevations that are small with respect to skin depth. This is particularly true if the transmitter is located directly over the horst, in which case, the topographic feature contributes nearly 100 percent of the total magnetic field. The effect of the horst remains more than 10 percent of the total magnetic field when the transmitter is three skin depths from the center of a horst that is only half a skin depth in height.

An understanding of the effects of mutual target interaction, host conductivity, and topography can be approached with the use of rigorous forward CSEM modeling. A fully three-dimensional modeling algorithm, such as the finite element approach presented in this study, is required to accurately model the response of a complex conductivity model. This complexity, however, is not unusual in field sites. Applications of CSEM to environmental issues, such as the detection and discrimination of unexploded ordnance, require the correct interpretation of field data in the presence of multiple buried targets collocated with metallic fragments, variable soil conductivity, and microtopography.

REFERENCES

Anderson, W., Frischknecht, F., Raab, P., Bradley, J., and Turnross, J., 1983, Results and preliminary inversion of loop-loop of frequency domain electromagnetic soundings near Medicine Lake, California: U.S. Geological Survey Open-file Report, pages 83–830.

Avdeev, D., Kuvshinov, A., Pankratov, O., and Newman, G., 1997, High-performance three-dimensional electromagnetic modeling using modified Neumann series. Wide band numerical solution and examples: J. Geomag. Geoelectr., **49**, 1519–1539.

Badea, E., Everett, M., Newman, G., and Biro, O., 2001, Finite-element analysis of controlled-source electromagnetic induction using coulomb-gauged potentials: Geophysics, **66**, 786–789.

Barton, M., and Cendes, Z., 1987, New vector finite elements for three-dimensional magnetic field computation: J. Applied Physics, **61**, 3919–3921.

Benavides, A., and Everett, M., 2003, Target detection in near-surface controlled-source electromagnetic data: Geophysics, **in press**.

Biro, O., and Preis, K., 1989, On the use of magnetic vector potential in the finite element analysis of three-dimensional eddy currents: IEEE Trans. Magn., **25**, 3145–3159.

Biro, O., and Richter, K., 1991, Cad in electromagnetism: Adv. Electronics Electron Phys., **82**, 1–96.

Boyse, W., Lynch, D., Paulsen, K., and Minerbo, G., 1993, Nodal-based finite element modeling of Maxwell's equations: IEEE Trans. Antennas Propagation, **40**, 642–651.

Bracewell, R., 2000, The Fourier Transform and its Applications: McGraw-Hill, New York, third edition.

Buselli, C., Barbar, C., Davies, G., and Salama, R., 1990, Detection of groundwater contamination near waste disposal sites with transient electromagnetic and electrical methods *in* Ward, S., Ed., Geotechnical and Environmental Geophysics: Soc. Expl. Geophys., 27–41.

Canann, S., Saigal, S., and Owen, S. E., 2000, Special issue: Unstructured mesh generation: International Journal for Numerical Methods in Engineering, **49**, 1–351.

Chen, Q., and Konrad, A., 1997, A review of finite element open boundary techniques for static and quasi-static electromagnetic field problems: IEEE Trans. Magn., **33**, no. 1, 663–676.

Duckworth, K., and Clement, B., 2001, Inductive interaction between closely spaced steeply dipping tabular conductors located in a resistive host: Geophysics, **66**, 1052–1058.

Edelsbrunner, H., 2000, Triangulations and meshes in computational geometry *in* Iserles, A., Ed., Acta Numerica: Cambridge Univ. Press, 133–213.

Eisenburg, M., and Malvern, L., 1973, On finite element integration in natural coordinates: Int. J. Numer. Methods Eng., **7**, 574–575.

Everett, M., and Schultz, A., 1996, Geomagnetic induction in a heterogeneous sphere: azimuthally symmetric test computations and the response of an undulating 660-km discontinuity: J. Geophys. Res., **101**, 2765–2783.

Everett, M., Badea, E., Shen, L., Merchant, G., and Weiss, C., 2001, 3-d finite element analysis of induction logging in a dipping formation: IEEE Trans. Geosci. Remote Sens., **39**, 2244–2252.

Everett, M., and Weiss, C., 2002, Geological noise in near-surface electromagnetic data: Geophys. Res. Lett., **29**.

Freund, R., Golub, G., and Nachtigal, N., 1992, Iterative solutions of linear systems *in* Iserles, A., Ed., Acta Numerica:: Cambridge Univ. Press, 57–100.

Fullagar, P., 1981, Inversion of horizontal loop electromagnetic soundings over a stratified earth: Ph.D. dissertation, University of British Columbia.

Fullagar, P. K., and Oldenburg, D. W., 1984, Inversion of horizontal loop electromagnetic frequency soundings: Geophysics, **49**, 150–164.

Geng, N., Baum, C., and Carin, L., 1999, On the low-frequency natural response of conducting and permeable targets: IEEE Trans. Geosci. Remote Sens., **37**, 347–359.

Grant, F., and West, G., 1965, Interpretation theory in applied geophysics, International Series in the Earth Sciences: McGraw-Hill Book Company.

Griffiths, D. J., 1999, Introduction to electrodynamics: Prentice Hall, Upper Saddle River, New Jersey.

Guptasarma, D., and Singh, B., 1997, New digital filters for hankel transform j_0 and j_1 transforms: Geophysical Prospecting, **45**, 745–762.

Hoekstra, P., and Blohm, M., 1990, Case histories of time-domain electromagnetic soundings in environmental geophysics *in* Ward, S., Ed., Geotechnical and Environmental Geophysics: Soc. Expl. Geophys., 1–15.

Hohmann, G., 1975, Three-dimensional induced polarization and electromagnetic modeling: Geophysics, **40**, 309–324.

Huang, H., and Won, I., 2003, Characterization of UXO-like targets using broadband electromagnetic induction sensors: IEEE Trans. Geosci. Remote Sens., **41**, 652–663.

Ivanenko, S., and Garanzha, V., Eds., 2002, Grid generation: Theory and applications, Communications on Applied Mathematics: Russian Academy of Sciences, Moscow.

Johnson, C., 1987, Numerical solution of partial differential equations by the finite element method: Cambridge University Press, Cambridge.

Kardestuncer, H., Ed., 1987, Finite element handbook: McGraw-Hill, New York.

Liu, A., and Joe, B., 1996, Quality local refinement of tetrahedral meshes based on 8-subtetrahedron subdivision: Math. of Comp., **65**, 1183–1200.

McNeill, J., Electromagnetic terrain conductivity measurement at low induction numbers:, Technical Report TN-6: Geonics Limited, 1980a.

———, Applications of transient electromagnetic techniques, Technical Report TN-7: Geonics Limited, 1980b.

Mitchell, A. R., and Wait, R., 1978, The finite element method in partial differential equations: Wiley, New York.

Mitsuhata, Y., 2000, 2-D electromagnetic modeling by finite-element method with a dipole source and topography: Geophysics, **65**, 465–475.

Mur, G., 1993, The finite-element modeling of three-dimensional electromagnetic fields using edge and nodal elements: IEEE Trans. Antennas Propagation, **41**, 948–953.

Nabighian, M., 1979, Quasi-static transient response of a conducting half-space: An approximate representation: Geophysics, **44**, 1700–1705.

Nabighian, M., Ed., 1988, Electromagnetic Methods in Applied Geophysics; Volume 1, Theory: Soc. Expl. Geophys.

Nabighian, M., Ed., 1991, Electromagnetic Methods in Applied Geophysics; Volume 2, Applications: Soc. Expl. Geophys.

Nabighian, M., and Macnae, J., 1991, Time domain electromagnetic prospecting methods *in* Nabighian, M., Ed., Electromagnetic Methods in Applied Geophysics; Volume 2, Applications: Soc. Expl. Geophys., 427–520.

Newman, G., Hohmann, G., and Anderson, W., 1986, Transient electromagnetic response of a three-dimensional body in a layered earth: Geophysics, **51**, 1608–1627.

Newman, G., and Alumbaugh, D., 1995, Frequency-domain modelling of airborne electromagnetic responses using staggered finite differences: Geophys. Prosp., **43**, 1021–1042.

Newman, G., 1999, 3–D magnetotelluric modeling and inversion: 2nd International Symposium on Three–Dimensional Electromagnetics, Salt Lake City UT, October 26–28, 1999.

Omeragic, D., and Silvester, P., 1996, Numerical differentiation in magnetic field postprocessing: Internat. J. Num. Mod.: Elect. Net., Dev., Fields, **9**, 99–113.

Palacky, G., 1987, Resistivity characteristics of geologic targets *in* Nabighian, M., Ed., Electromagnetic Methods in Applied Geophysics; Volume 1, Theory: Soc. Expl. Geophys., 53–130.

Pierce, C., Benavides, A., Everett, M., and Stalnaker, J., 2003, UXO detection improvements using EM63 synthetic multi-receiver array geometries (expanded abstract): SEG 73rd Annual Meeting, Dallas, TX, October, 2003.

Press, W., Teukolsky, S., Vetterling, W., and Flannery, B., 1992, Numerical recipes in FORTRAN: The art of scientific computing: Cambridge University Press.

Pridmore, D., Hohmann, G., Ward, S., and Sill, W., 1981, An investigation of finite-element modeling for electrical and electromagnetic data in three dimensions: Geophysics, **46**, 1009–1024.

Senos Matias, M., Marques da Silva, M., Ferreira, P., and Ramalho, E., 1994, A geophysical and hydrogeological study of aquifer contamination by a landfill: J. Appl. Geophys., **32**, 155–162.

Shubitdze, F., and O'Neill, K., 2002, Application of the method of auxilliary sources to the wide-band electromagnetic induction problem: IEEE Trans. Geosci. Remote Sens., **40**, 928–942.

Silvester, P., and Ferrari, R., 1996, Finite elements for electrical engineers: Cambridge University Press.

Sinha, A., 1980, A study of topographic and misorientation effects in multifrequency electromagnetic soundings: Geoexploration, **18**, 111–113.

Smith, J., 1996, Conservative modeling of 3-d electromagnetic fields: Geophysics, **61**, 1308–1324.

Sugeng, F., Raiche, A., and Xiong, Z., 1999, An edge–element approach to modeling the 3–D em response of complex structures with high contrasts: 2nd International Symposium on Three–Dimensional Electromagnetics, Salt Lake City UT, October 26–28, 1999.

Sun, D., Manges, J., Yuan, X., and Cendes, Z., 1995, Spurious modes in finite-element methods: IEEE Antennas and Propagation Magazine, **37**, 12–24.

Tabarra, M., Blacker, T., and Belytschko, T., 1994, Finite element derivative recovery by moving least squares interpolants: Comp. Meth. Appl. Mech. Eng., **117**, 211–223.

Travis, B., and Chave, A., 1989, A moving finite element method for magnetotelluric modeling: Phys. Earth Planet. Internat., **53**, 432–443.

Wait, J., 1954, Mutual coupling of two loops lying on the ground: Geophysics, **19**, 290–296.

Wait, J., 1955, Mutual electromagnetic coupling of loops over a homogeneous ground: Geophysics, **20**, 630–637.

Wait, J., 1956, Mutual electromagnetic coupling of loops over a homogeneous ground—an additional note: Geophysics, **21**, 479–484.

Wang, T., and Hohmann, G., 1993, A finite-difference, time domain solution for three-dimensional electromagnetic modeling: Geophysics, **58**, no. 6, 797–809.

Ward, S., and Hohmann, G., 1987, Electromagnetic theory for geophysical applications *in* Nabighian, M., Ed., Electromagnetic Methods in Applied Geophysics; Volume 1, Theory: Soc. Expl. Geophys., 131–311.

Weidelt, P., 1975, Electromagnetic induction in three-dimensional structures: Journal of Geophysics, **41**, 85–109.

West, G., and Macnae, J., 1991, Physics of the electromagnetic induction exploration method *in* Nabighian, M., Ed., Electromagnetic Methods in Applied Geophysics; Volume 2, Applications: Soc. Expl. Geophys., 5–46.

Zanoubi, M., Jin, J., Donepudi, K., and Chew, W., 1999, A spectral lanczos decomposition method for solving 3-d low-frequency electromagnetic diffusion by the finite-element method: IEEE Trans. Ant. Propag., **47**, 242–248.

Zhdanov, M., Dmitriev, V., Hursan, G., and Fang, S., 1999, Quasi–analytical approximations and series in 3–D electromagnetic modeling: 2nd International Symposium on Three–Dimensional Electromagnetics, Salt Lake City UT, October 26–28, 1999.

VITA

JACK STALNAKER

ADDRESS:
537 Washboard Road
Pelion, South Carolina 29123

EDUCATION:

B.S.	(1998)	Geology, College of Charleston, USA
B.S.	(1998)	Anthropology, College of Charleston, USA
Ph.D.	(2004)	Geophysics, Texas A&M University, USA

HONORS:
Chevron USA Scholarship (Texas A&M University)
Harrison Randolph Scholarship (College of Charleston)
NASA Space Grant (College of Charleston)

SELECTED PUBLICATIONS:

Stalnaker, J.L., Everett M.E., Benavides, A., and Pierce, Jr., C.J., 2004, Mutual induction and the effect of host conductivity on the EM induction response of multiple buried plates using 3-D finite element analysis: IEEE Trans. Geosci. Remote Sens., in press.

Pierce, Jr., C.J., Benavides, A., Everett, M.E., and **Stalnaker, J.L.**, 2003, UXO detection improvements using EM63 synthetic multi-receiver array geometries: SEG 73rd Annual Meeting, Dallas, TX, October, 2003.

Stalnaker, J.L. and Everett, M.E., 2002, The controlled-source electromagnetic response of two buried plates, including mutual induction and interaction with the host medium: EOS Trans. AGU, **83**, Fall Meet. Suppl. Abstract GP51A-0983.

Stalnaker, J.L and Everett, M.E., 2002, Finite element analysis of controlled-source electromagnetic induction for near-surface geophysical prospecting: SEG 72nd Annual Meeting, Salt Lake City, UT, October, 2002.

Stalnaker, J.L. and Everett, M.E., 2002, Finite element analysis of controlled-source electromagnetic induction for near-surface geophysical prospecting: The 16th Workshop on Electromagnetic Induction in the Earth, Santa Fe, NM, EM 5-40.

Stalnaker, J.L. and Newman, G.A., 2001, Sensitivity analysis of borehole time-domain controlled-source electromagnetic models: Sandia National Laboratories SAND report, SAND2001-2270A.

Stalnaker, J.L. and Nusbaum, R.L., 1998, Using remote sensing to locate potential hominid fossil sites, Hadar Region, Ethiopia: South Carolina Academy of Sciences Meeting, 71st Annual Meeting, Clemson, SC.